STUDY OF LONG RANGE POTENTIALS IN EXCITED STATES OF DIATOMIC

SODIUM USING MODULATED GAIN SPECTROSCOPY

by

GUNJIT CHAWLA

B.S., Virginia Commonwealth University
(1978)

SUBMITTED TO THE DEPARTMENT OF
CHEMISTRY IN PARTIAL
FULFILLMENT OF THE
REQUIREMENTS FOR THE
DEGREE OF
DOCTOR OF PHILOSOPHY

at the

MASSACHUSETTS INSTITUTE OF TECHNOLOGY

June (1985)

Signature of Author_____
Department of Chemistry
March 29, 1985

Certified by_____, _____
Robert W. Field
Thesis Supervisor

Accepted by_____ _____
Dietmar Seyferth
Chairman, Department Committee

This thesis has been examined by a committee of the Department of Chemistry as follows:

Professor _____
                                    Robert W. Field, Thesis Supervisor

Professor _____
                                    David E. Pritchard

Professor _____
                                    James L. Kinsey, Chairman

STUDY OF LONG RANGE POTENTIALS IN EXCITED STATES OF DIATOMIC

SODIUM USING MODULATED GAIN SPECTROSCOPY

by

GUNJIT CHAWLA

Submitted to the Department of Chemistry
on March 29, 1985 in partial fulfillment of the
requirements for the Degree of Doctor of Philosophy in
Chemistry

ABSTRACT

The long range intramolecular potentials of the Na_2 $A^1\Sigma_u^+$ and $B^1\Pi_u$ electronic states have been investigated by studying properties of the high vibrational levels that they support. In the case of the $B^1\Pi_u$ state, the long range potential possesses an intrinsic barrier to dissociation. By measuring the ro-vibrational energies of all (v'=27-33) quasibound vibrational levels and the rotation-dependent tunneling rates (as obtained by linewidth measurements) of the last quasibound vibrational level, we have been able to characterize this barrier. Our studies show that the barrier height U_m=369.5±3.9 cm^{-1}, relative to the center of gravity of the Na(3s)+Na(3p) atomic limit, and the barrier maximum is located at R_m=6.85±0.02Å. For the $A^1\Sigma_u^+$ state, many vibrational levels lying in the range of v'=43-105 have been investigated allowing us to characterize the potential up to 96% of its dissociation limit (corresponding to an outer internuclear separation of 10.7Å) using an RKR inversion procedure.

Accessing the high vibrational levels in the above electronic states posed a particularly challenging problem due to their poor Franck-Condon overlap with thermally populated levels of the $X^1\Sigma_g^+$ state. In order to overcome this difficulty, we have developed a new technique called Modulated Gain Spectroscopy.

Thesis Supervisor: Robert W. Field

Title: Professor of Chemistry

This thesis is respectfully dedicated to my grandparents,

Harnam Singh and Jaswant Kaur

TABLE OF CONTENTS   PAGE

8

TABLE OF CONTENTS   PAGE

CHAPTER 4 THE Na_2 $B^1\Pi_u$ STATE 111

4.1 Introduction 112

4.2 Presentation of Data 115

4.3 Analysis of Energy Levels. 117

A. Padé Representation. 117

B. RKR Potential. 127

4.4 Analysis of MGS Lineshapes 127

4.5 WKB Transmission Probability .138

4.6 From Tunneling Lifetimes to Potential Barrier. 149

4.7 Alternate Method for Determining Barrier Maximum 156

CHAPTER 5 THE Na_2 $A^1\Sigma_u^+$ STATE 161

5.1 Introduction 162

5.2 Presentation of Data 162

5.3 A $^1\Sigma_u^+$ State RKR Potential. 167

5.4 Determination of C_n Coefficients using Le Roy's Method 175

A. Principles 175

B. Application to the A State 184

5.5 Estimation of C_n Coefficients from RKR Turning Points. 190

CHAPTER 6 CONCLUSIONS. 197

REFERENCES. 200

LIST OF FIGURES   PAGE

LIST OF FIGURES   PAGE

LIST OF TABLES   PAGE

CHAPTER ONE

INTRODUCTION

Understanding the nature of forces between atoms at large internuclear separations (generally for R > 5Å) has been an underlying theme in many areas of physics and chemistry from the spectroscopy of diatomic molecules near dissociation[1-3] to atomic scattering processes[4,5], collision-induced, atomic line broadening[6,7], gas transport properties[8] and even condensed phase properties[8]. Conversely, the parameters characterizing the long range interatomic forces can be determined with varying degrees of accuracy, by studying any of the above mentioned processes. In this work we propose a method for studying the behavior of long range interactions which has the advantage of being direct and state-selective.

Our method is best illustrated with reference to Figure 1.1. The figure illustrates why the properties of excited vibrational levels strongly reflect the long range part of the interatomic potential. Because molecules in high vibrational levels spend a large fraction of their vibrational period in the vicinity of the outer (classical) turning point (due to the very small slope of the outer potential wall at high energies), the average value of any measured property of a molecule excited to these vibrational states will be dominated by its value near the outer part of the potential. Hence, measured properties of excited vibrational levels can be used to infer about the behaviour of interatomic potentials at large R.

The particular system considered in the present study consists of two sodium atoms, one in its ground state (3s) ^2S and the other in an excited state (3p) ^2P. Alkali atoms are particularly well-suited for such study because they are theoretically simple to handle due to the possibility of treating the effects of the core and valence electrons separately.

Figure 1.1 The interatomic potential of weakly bound KAr illustrates

the large probability amplitude of the vibrational wavefunction

near the outer turning point, for high v levels. (From Ref. 9) .
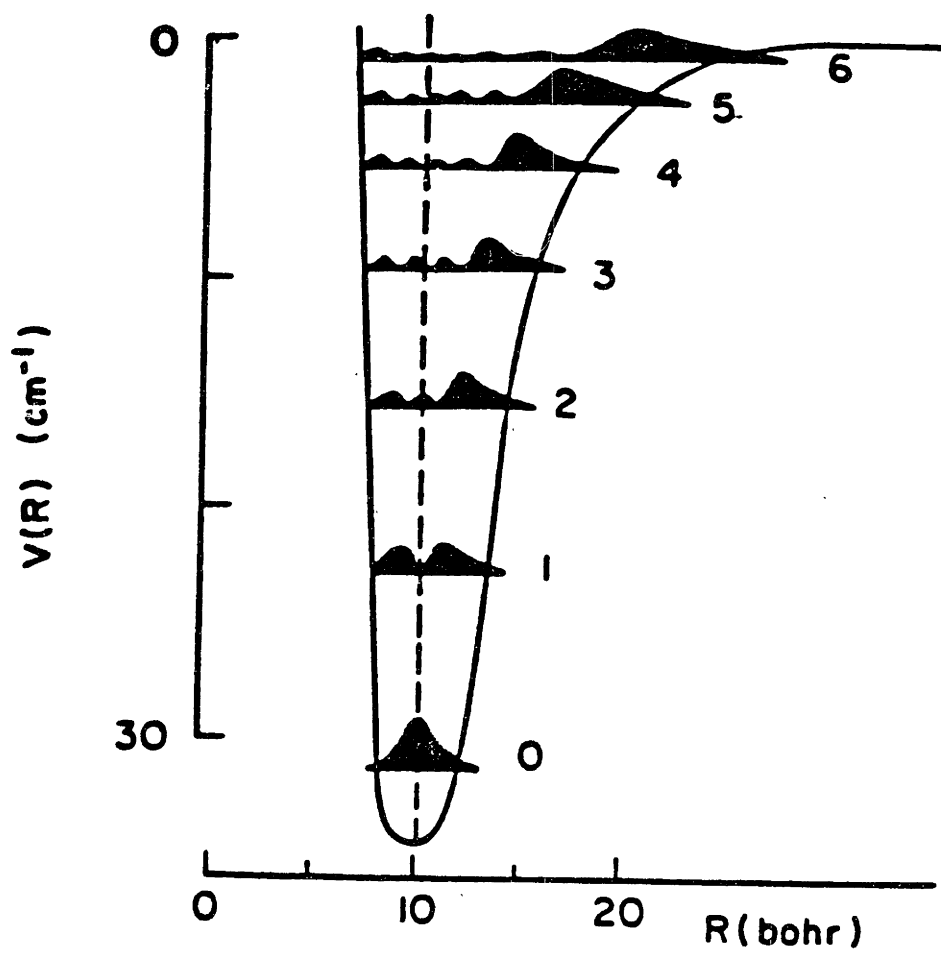
Besides being theoretically tractable, the spectroscopy of these alkali dimers is also very amenable to experimental study. The fact that the valence electrons in these systems are weakly bound (relative to hydrogen) leads to large oscillator strengths and strong electronic transitions in the visible part of the spectrum. The widespread availability of tunable dye lasers makes these electronic transitions easily accessible.

The Na 3s + Na 3p interactions have been of interest to us because they involve resonant interactions arising from the presence of an electric-dipole allowed transition between the 3s and 3p states. This resonance interaction leads to a long range potential which is dominated by a dipole-dipole C_3/R^3 contribution. A potential varying as $1/R^3$ corresponds to a relatively slow variation of the interatomic potential with R, and leads to a high density of vibrational states near the dissociation limit for some molecular states of Na$_2$ like the $A^1\Sigma_u^+$ state. For the $A^1\Sigma_u^+$ state, the C_3/R^3 term is attractive. The C_3/R^3 term can also be repulsive and in some cases produces the effect of a barrier to dissociation, as in the $B^1\Pi_u$ state of Na$_2$. Thus, studies of the Na$_2$ $A^1\Sigma_u^+$ and $B^1\Pi_u$ states can complement one another very well.

A second and more significant reason for studying the long range potentials of one Σ and one Π molecular state is that this work could lead to the determination of potentials for all other Na$_2$ molecular states correlating to the 3s + 3p atomic limit. Herein lies a major aspect of the appeal of long range theory. Since long range forces between atoms depend on the isolated atomic properties, there exist fundamental interrelationships between the C_n terms (where the C_n's are

coefficients of the R^{-3}, R^{-6}, R^{-8} terms in the R^{-n} expansion of long range potential energy) of different molecular states having the same atomic limit[10-12]. These interrelations serve to unify the properties of all molecular electronic states (at large R) arising from a given pair of separated atom states; they can be exploited to determine the behavior of many hitherto unobserved molecular potentials based upon detailed experimental knowledge of a select few. (These interrelationships are elaborated on in Chapter Three). As a by-product, one can also make estimates of fundamental atomic properties, for example, the static dipole polarizability from the Van der Waals C_6 coefficient.

Of the 24 ways in which two Na atoms one in the 3s state and the other in the 3p state can combine, twelve are gerade {$^1\Sigma_g^+$, $^1\Pi_g$, $^3\Sigma_g^+$, $^3\Pi_g$} while the other twelve are ungerade. Few of these molecular states have been studied in detail or observed experimentally either because of the different geometries of these excited states relative to the ground X $^1\Sigma_g^+$ state (leading to poor Franck-Condon factors) or because of the restrictive selection rules (rigorous g $\not\leftrightarrow$ g and approximately good singlet $\not\leftrightarrow$ triplet). We hoped to be able to characterize the long range potentials of these twenty-four molecular states by studying the excited vibrational levels of the A $^1\Sigma_u^+$ and B $^1\Pi_u^+$ states. Since these two states have been previously investigated near their potential minimum by several groups[13-17] (see Figure 1.2), extensions of their studies towards higher energies should be relatively straighforward, at least in principle.

In actual fact, one is confronted with a major experimental difficulty when attempting to study high lying vibrational levels. These levels

Figure 1.2 RKR potential curves for the Na$_2$ ground X $^1\Sigma_g^+$ electronic state,

from Ref. 14, and the excited A $^1\Sigma_u^+$ and B $^1\Pi_u$ electronic

states, from Refs. 14-16. The dashed regions of the A and

B state potentials had not been observed prior to this work.
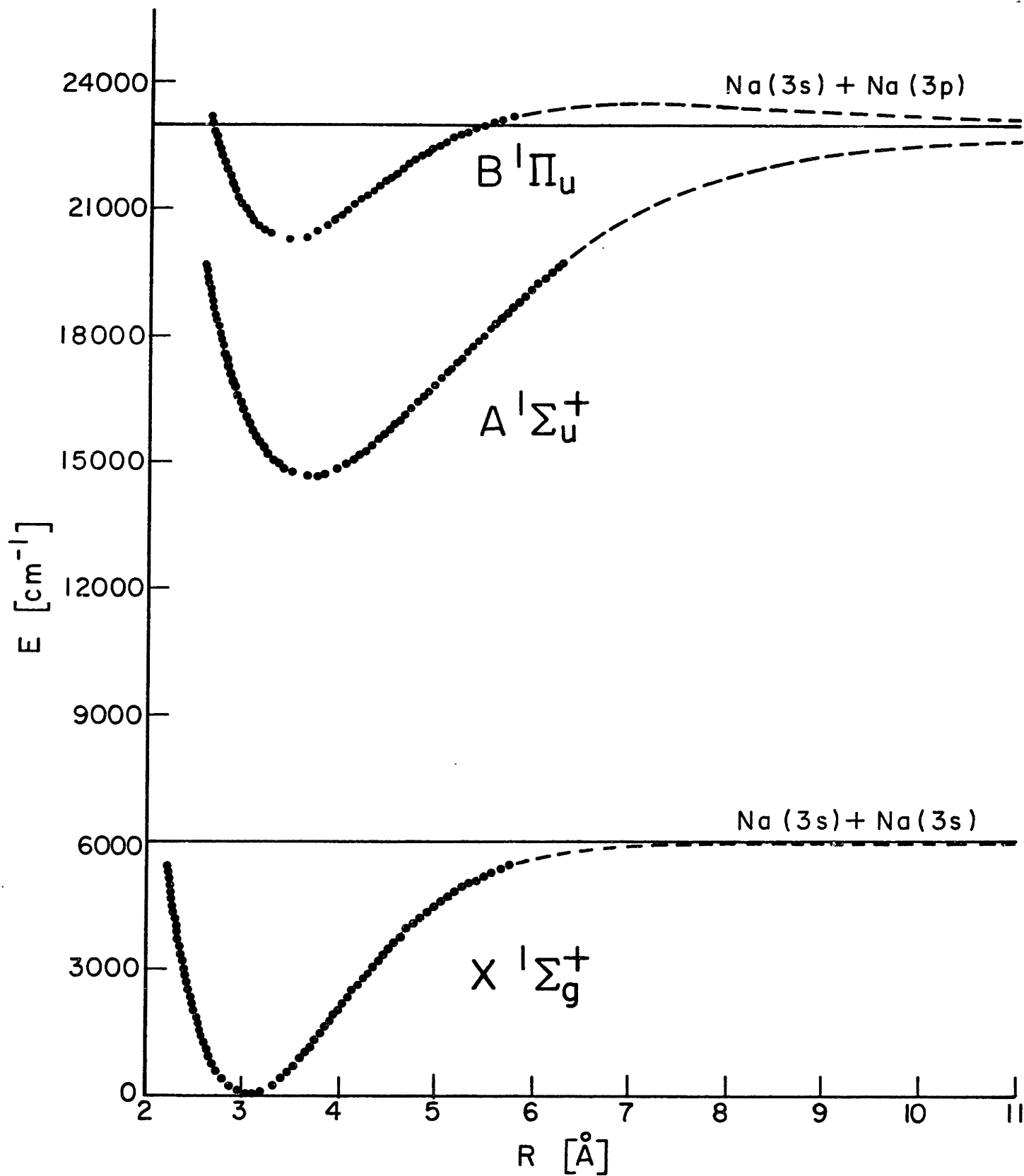
Figure 1.3 For typical ground and excited state potentials, thermally
populated levels of the ground state (dots) generally allow access
to only the dotted regions of the upper state whereas highly
excited levels of the ground state (checkers) allow access to the
checkered, excited regions of the upper state (in this case, via
the inner turning point).

TARGET
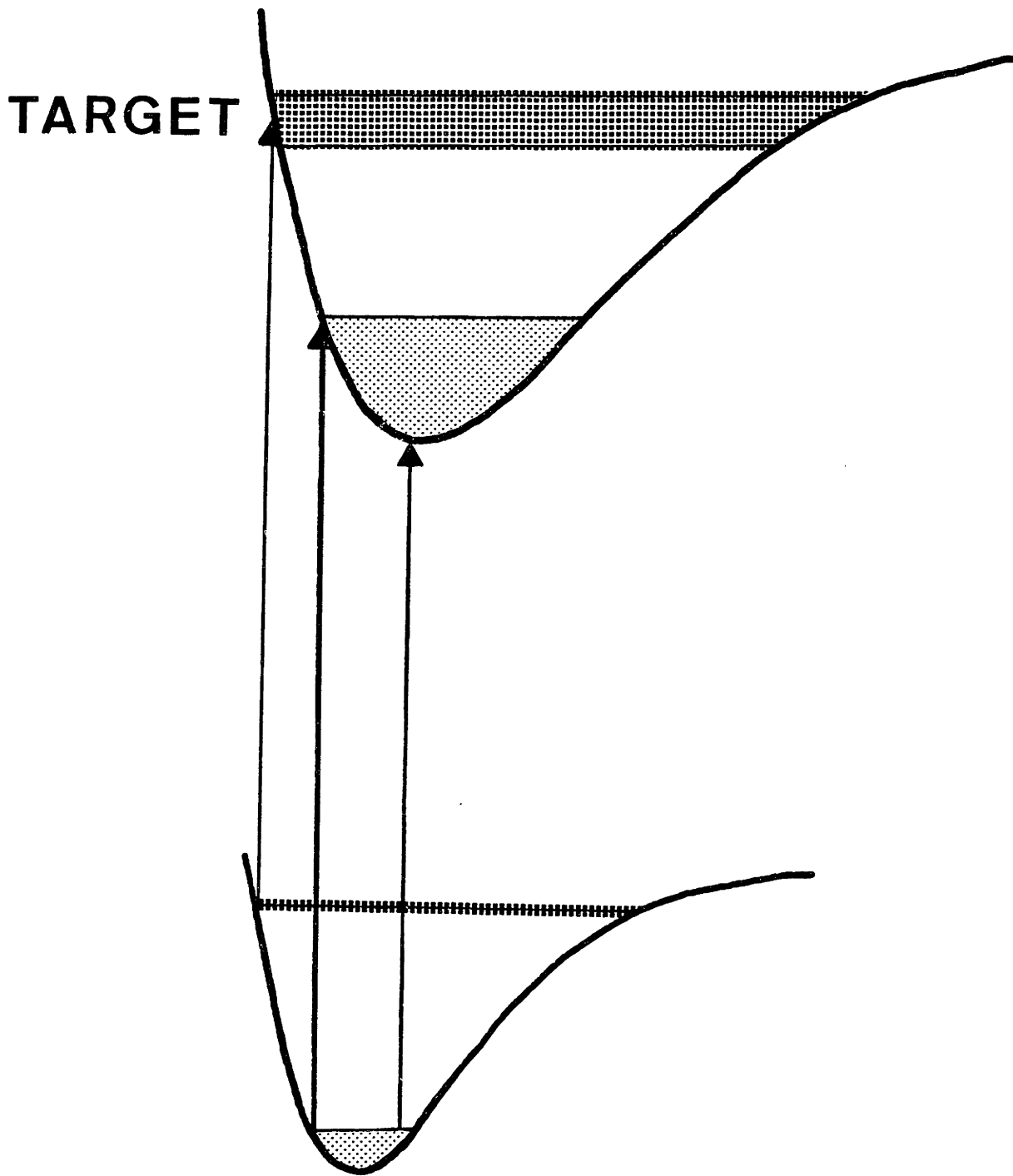
usually have extremely small Franck-Condon factors with thermally populated ground state levels and as a result are not accessible from the lowest vibrational states. However, excited vibrational levels of the ground electronic state generally can have quite large Franck-Condon factors with the vibrational levels of interest (in the excited electronic state), as illustrated in Figure 1.3. It therefore appeared necessary to devise a scheme by which we could first selectively transfer population in to the high v levels of the ground electronic state, and then excite this population to the target levels. (It would in addition be desirable for such a scheme to permit selective and sensitive detection of these excitations.)

In this study, we propose and demonstrate the use of a new multistep laser excitation technique that is expressly designed to meet the above mentioned requirements, for the study of high lying vibrational levels. It is called Modulated Gain Spectroscopy (MGS). A description of the principles of MGS as well as some practical measures taken to implement it are contained in Chapter Two. The usefulness of the technique is demonstrated by the observation of many high lying vibrational levels, in the range v=43-105, in the A $^1\Sigma_u$ state and all (rotationless) quasibound levels, v=27-33, in the B $^1\Pi_u$ state of Na_2. These results and the long range potentials determined for these two electronic states are discussed Chapters Four and Five.

CHAPTER TWO

EXPERIMENTAL

2.1 Introduction

This chapter presents the principles of the Modulated Gain
Spectroscopy technique and some operational details of experiments
utilizing MGS to study the A $^1\Sigma_u^+$ and B $^1\Pi_u$ electronic states of Na_2.
Sections two and three provide a description of the technique and an
overview of the experimental apparatus. Some design considerations of
the two key elements in the apparatus - the "heat pipe", used to generate
the Na_2 species, and the Na_2 optically pumped laser cavity - are
presented in further detail in sections four and five. Lastly, section
six describes the rich variety of signals that can be observed with the
MGS technique.

2.2 Principles of Modulated Gain Spectroscopy

Figure 1.3 portrays the typical problem encountered when studying
excited state long range potentials, or equivalently the high lying
vibrational levels: poor Franck-Condon factors for transitions out of
thermally populated levels of the ground state. The use of MGS
circumvents this problem and, in addition, provides a sensitive,
nonlinear means of detecting transitions to the target levels with
sub-Doppler resolution and greatly reduced spectral congestion.

The MGS technique is best illustrated by reference to Figure 2.1.
Three stepwise optical transitions allow access to high lying vibrational
levels of interest; the three lasers involved in the excitation scheme
are termed the PUMP, OPL, and PROBE lasers. The PUMP excites thermal
population in a level of the ground state preferentially into those
regions of the upper electronic state with which the initial level (type
1) has best vibrational overlap. The usual fate of the excited state

Fig. 2.1 MGS level diagram illustrating the PUMP → OPL → PROBE

sequence used to study levels of type 4.

MODULATED GAIN TECHNIQUE $\begin{cases} \text{PUMP \& OPL : Sample} \\ \qquad\qquad\qquad\text{Preparation} \\ \text{OPL \& PROBE : Signal} \\ \qquad\qquad\qquad\text{Detection} \end{cases}$

④

②

PROBE

OPL

$$\boxed{\text{GAIN} \sim N_2 - N_3}$$

PUMP

③

①
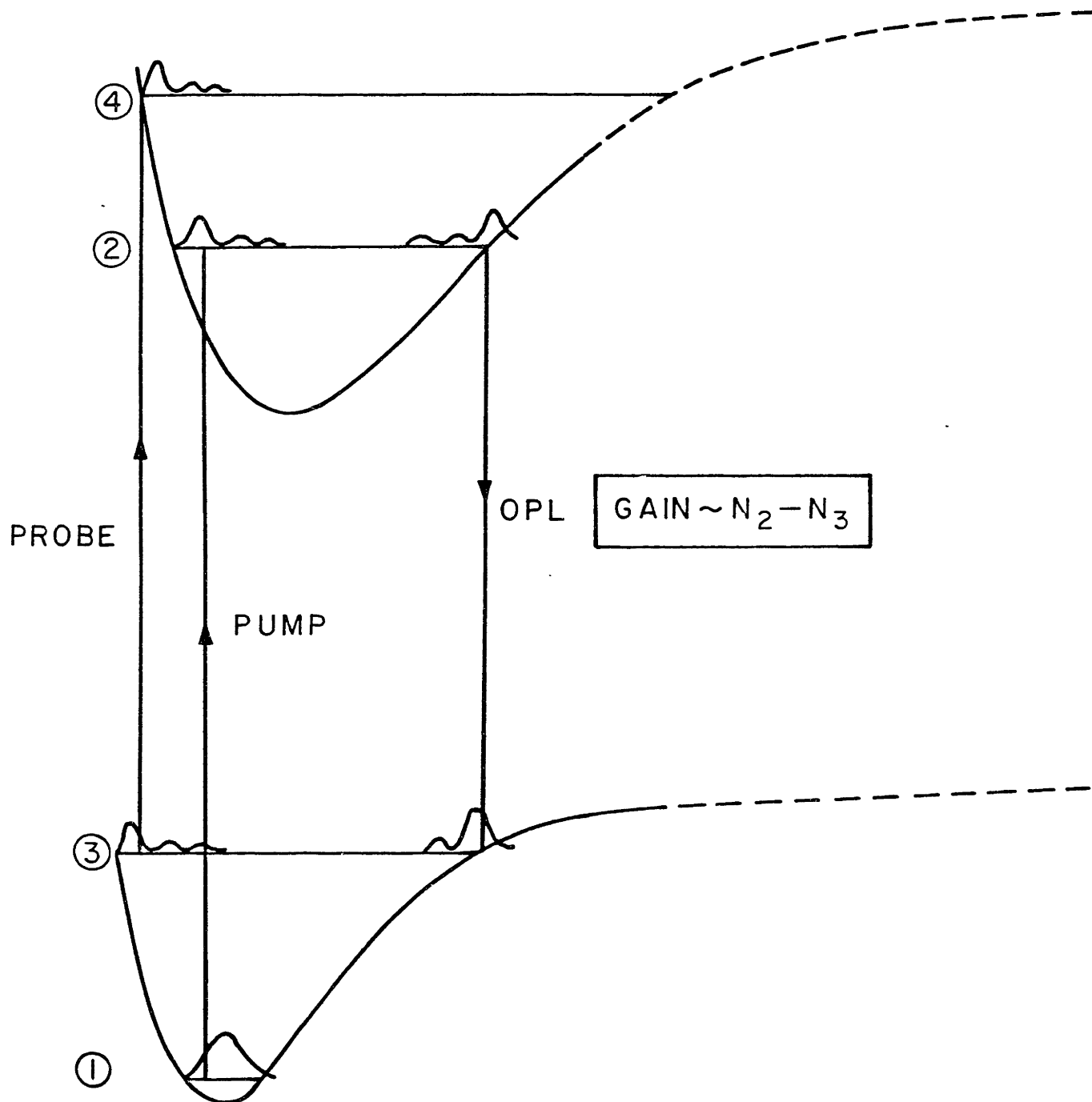
levels (type 2) thus populated by the PUMP is fluorescence into levels (type 3) of the ground state with which they have favorable Franck-Condon overlap. Therefore, a small fraction of the fluorescence from the type 2 levels consists of simple resonance fluorescence (via the inner turning point) but a large fraction consists of red-shifted fluorescence (via the outer turning point) due to the relative displacement of the upper state towards larger R. Since the red emission terminates on levels of the ground electronic state that are not thermally populated (type 3), the system possesses a population inversion with respect to these levels. Placing this inverted medium inside a laser cavity will cause it to lase on those transitions on which it would normally fluoresce (which are characterized by a population inversion). With the insertion of frequency selective elements inside the laser cavity, one can force this Optically Pumped Laser (OPL) to oscillate on a specific transition of interest. Thus, the effect of the PUMP-OPL cycle is to transfer a substantial fraction of thermal population from a single low-lying vibrational level to a selected high-lying vibrational level of the ground electronic state. Once this level (type 3) is populated, a third PROBE laser can excite the 4←3 transition with good Franck-Condon factors and thus access the levels of interest (type 4).

When the PROBE is in resonance with a 4←3 transition, it removes population from the lower OPL level, thus causing an increase in population inversion on the OPL transition, and an increase in the OPL intensity. Since each PROBE absorption is accompanied by a concommitant increase in the OPL intensity, resonances excited by the PROBE can be sensitively and selectively detected by monitoring differential increases in the OPL intensity.

The MGS technique is, in some respects, very similar to Intracavity Dye Laser Spectroscopy (IDLS).[19,20] In IDLS, the species under investigation and the dye laser are two physically distinct entities. The absorption spectrum is obtained by placing an absorption cell within a dye laser cavity and scanning the frequency of that dye laser. Each sample absorption results in an increased loss experienced by the dye laser system and therefore produces a decrease in the dye laser intensity. These differential intensity changes as a function of frequency provide a sensitive measure of the sample absorption spectrum. In MGS, the species of interest and the laser are one and the same. An external laser (the PROBE) excites the sample and in so doing, decreases the losses of the OPL system thus producing an increase in the OPL intensity. (The PROBE excitation rate reduces the losses since the small collisional depopulation rate of the lower OPL level normally limits the maximum population inversion attainable). Both MGS and IDLS rely upon small changes in intracavity losses causing large changes in the laser output. Where the two methods differ is that IDLS utilizes additional effects to enhance its overall sensitivity, such as multiple passes of the exciting radiation and cavity mode competition of the dye laser. The former effect does not play a role in MGS since the PROBE is usually weak and almost completely absorbed after two passes; the latter effect does not come into play since the OPL is intentionally operated on a single longitudinal and transverse mode in order to minimize intensity fluctuations (and thus maximize our ability to detect intensity changes caused by PROBE absorptions).

In addition to the nonlinear sensitivity afforded by MGS, one also

achieves sub-Doppler resolution as well as some spectral simplification.
The first feature arises because the narrow bandwidth PUMP (~2 MHz)
interacts with a narrow range of longitudinal velocity components in
level 1. This velocity selection is transferred to level 3 via the
PUMP-OPL cycle. However, partial velocity scrambling in level 3 by
collisions with atomic sodium at 1 Torr results in PROBE signals that are
typically ~350 MHz FWHM (still significantly less than the Doppler width
of 1.5 GHz).

The second advantage, spectral simplification, arises for two
reasons. The first is common to all double and multiple resonance
schemes, namely only the lower OPL level has substantial population. The
second reason lies in the discrimination afforded by the method of
detecting PROBE coincidences: only those PROBE excited transitions that
modulate the gain of the OPL appear as signals. All other PROBE
excitations go undetected.

We will see in Section Six that the PROBE can modulate the gain of
the OPL by interacting with population in type 1, type 2, or type 3
levels. While the additional resonances increase the total number of MGS
signals, they do not make it impossible to identify the various types of
MGS signals and in fact illustrate the versatility of the MGS technique.

2.3 Experimental Overview

Figure 2.2 shows a schematic of the experimental apparatus. Sodium
dimer is generated in a 2" diameter "heat pipe" which is operated at
460°C with 1 torr of helium. The partial pressure of Na_2 under these
conditions is 25 mtorr[21]. The 160 Watt input power to the "heat pipe"
produces a 30 cm long Na/Na_2 isothermal vapor zone. The principles and

Figure 2.2   Experimental set-up.

BRF denotes Birefringent Filter; TE denotes Thin Etalon; OC

denotes Output Coupler; A denotes Aperture. Not shown is

the frequency calibration method for the PUMP and PROBE dye

lasers, which involves the simultaneous recording of

a) PUMP (and PROBE) excited I_2 excitation spectrum for

absolute frequency determination,[22] and b) transmission

fringes of PUMP (and PROBE) through a 300 MHz FSR

Fabry-Perot, for frequency interpolation and scan linearity

checks.
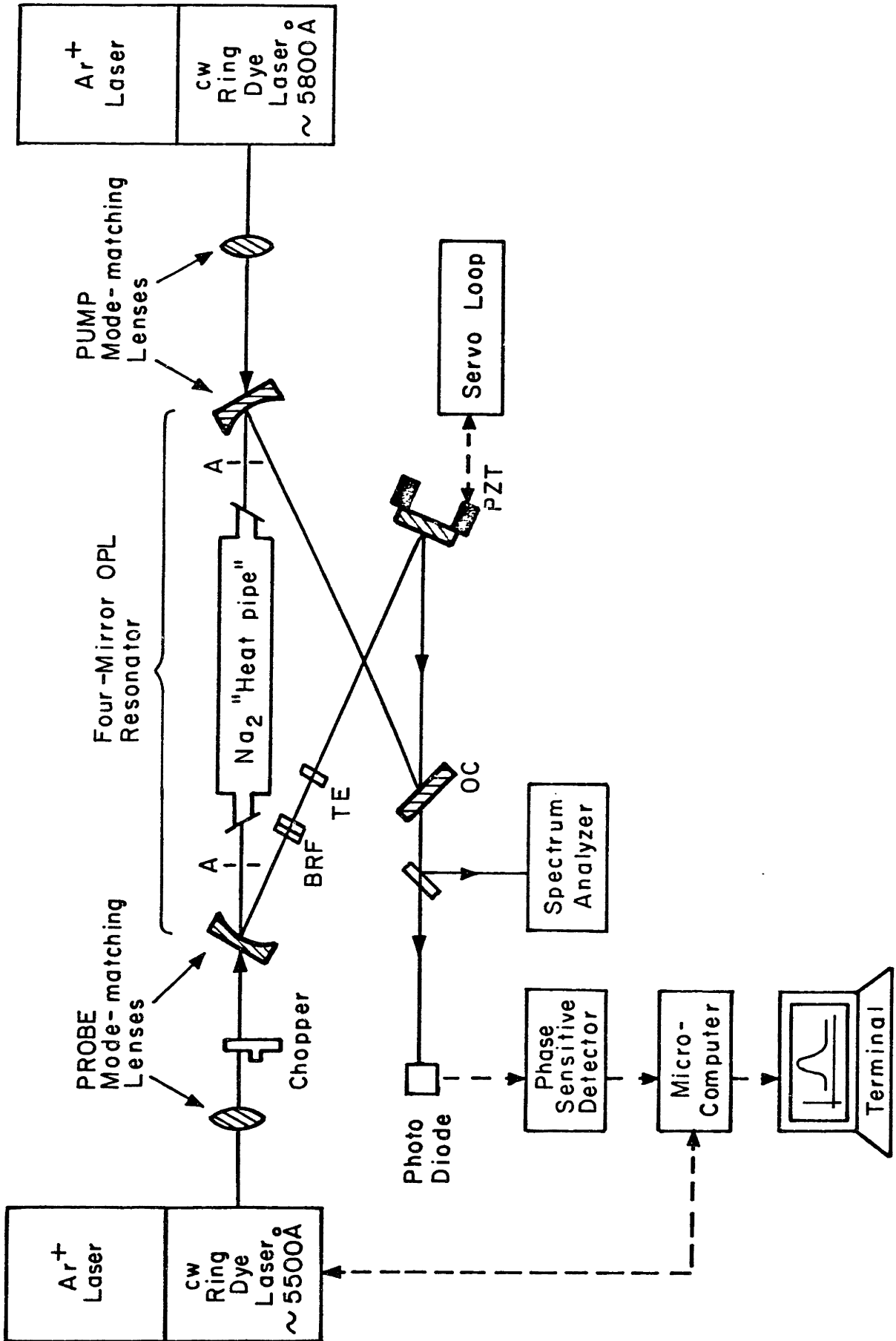
operating characteristics of the "heat pipe" will be described in section four.

The "heat pipe" is placed inside one leg of a figure-eight shaped resonator which makes up the OPL cavity. The ring resonator is defined by two R=300 cm dichroic reflectors (>99.9% reflectivity at 800nm and 60% transmissivity at 400 -650nm) located at opposite ends of the "heat pipe" and two flat high reflectors which complete the ring. A ring resonator is chosen to avoid optical feedback of the PUMP radiation into the pump laser which can cause both frequency and amplitude instability in the PUMP (and therefore the OPL); the particular geometry of the resonator is designed to accommodate three factors:

1) a 1 meter long heat pipe assembly,

2) the stability criteria of Gaussian resonator modes, and

3) minimized astigmatism of the cavity (i.e. astigmatism resulting from mirrors used in oblique reflection). Some characteristics of the resonator modes supported by the OPL cavity will be discussed in Section Five.

The PUMP laser (Coherent 699-21 c.w. ring dye) is typically operated with either Rhodamine 6G or DCM laser dye and possesses a frequency stabilized linewidth of ~2 MHz. The PUMP radiation propagates through one of the dichroic reflectors of the OPL cavity into the heat pipe. The TEM_{00} mode of the PUMP beam is matched to the fundamental Gaussian mode of the OPL cavity by a telescopic arrangement consisting of an R=200 cm reflector (represented by a lens in Figure 2.2) in series with one of the R=300 cm dichroic reflectors of the OPL resonator. (See Section 2.5 D for further detail). Typical PUMP power density is 15 W/cm^2 at the OPL beam waist, $\omega_0 \sim 0.05$ cm, located in the middle of the heat pipe.

When the PUMP excites a 2←1 transition, several 2→3 OPL transitions can be above lasing threshold. Using two frequency selective elements within the OPL cavity, a single OPL line is selected from all lasing transitions sharing the same upper OPL level. A 3-plate quartz birefringent filter selects a particular vibrational band (typical ground state vibrational separations are ~80 cm^{-1}) and a 0.5mm thin etalon (30% R at 800nm) selects a particular rotational line (typical PR line separations are 4-6 $cm^{-1}$for J~10). The traveling wave supported by the OPL ring cavity encourages all excited molecules to contribute to the gain of a single mode; therefore, oscillation on a single longitudinal cavity mode is achieved without any selecting elements. Two 2mm diameter irises located at opposite ends of the heat pipe enforce oscillation on the fundamental transverse mode. The intensity and spectral characteristics of the OPL are monitored by a photodiode and a 7.5 GHz FSR (Finnesse ~250) Tropel model 240 spectrum analyzer; both elements are located after the 2% T output coupler of the OPL cavity.

It should be noted here that the OPL copropagates with the PUMP owing to a direction-dependent, Raman contribution to the gain[23-25], which is present in addition to the isotropic, population-inversion (between type 2 and 3 levels) mechanism. For the "folded" PUMP-OPL scheme, the Raman gain linewidth is sub-Doppler when the OPL copropagates (with the PUMP) and completely Doppler broadened when the OPL counter-propagates. Since an equal number of excited molecules can contribute to gain in either direction (i.e. the integrated gain is the same for both directions), the forward Raman gain lineshape is narrow and large while the backward gain lineshape is broad and small. Hence the Na_2 OPL exhibits unidirectional oscillation, along the direction of the PUMP.

The PROBE (Coherent CR699-29 c.w. ring) is computer automated for wide spectral range frequency scans and is operated with Rhodamine 6G or Coumarin 540 laser dye. It is mode-matched to the OPL cavity in a fashion similar to the PUMP and for convenience, counter-propagates with respect to the PUMP through the second dichroic reflector of the OPL cavity. A 1 KHz mechanical chopper modulates the intensity of the PROBE; the differential change in OPL intensity accompanying a PROBE absorption is detected at this modulation frequency by a Keithley Model 840 phase sensitive detector.

Since increases of the OPL output intensity serve to detect the PROBE absorptions, the OPL intensity fluctuations when the PROBE is tuned off a 4←3 resonance sets the lower limit for the MGS detection sensitivity. The dominant source of <u>intensity</u> fluctuations is <u>frequency</u> fluctuations of the OPL arising, for example, from acoustic vibrations of mirrors and temperature or pressure variations causing refractive index changes within the cavity.

The very sensitive dependence of the frequency on refractive index, n, or mirror separation, ℓ, cannot be overemphasized. It is seen to change according to

$$\nu = mc/n\ell$$

$$\therefore \quad \Delta\nu/\nu = -[\Delta\ell/\ell + \Delta n/n]$$

(2.1)

If, for example, one wished to keep a laser operating at 3.75×10^{14} Hz stable to within 1 MHz, it would be necessary to require its mirror separation of 2.34 meters be kept constant to ± 6.2 nm. Compensating such small changes in the resonator length necessitates electronic

stabilization control.

To reduce large amplitude vibrations, the OPL cavity rests upon a vibration-isolated steel table and is housed in a simple box. It is then frequency stabilized to the peak of its own gain profile. This is accomplished in the following manner. The cavity frequency is modulated over a 15 MHz optical bandwidth at a frequency of 420 Hz. Since the laser intensity depends on the location of the cavity mode frequency relative to the optically pumped Na_2 the gain profile, the frequency modulation results in an intensity modulation. This modulation is detected by a phase sensitive detector (PSD), whose output is proportional to the first derivative of the gain profile when the PSD is tuned to 420 Hz. Thus, the PSD output provides the magnitude and sign of the error signal needed to tune the cavity frequency to the center of the gain profile. When the PSD is placed in a servo loop, the system equilibrates to zero PSD output voltage (i.e. the peak of the OPL gain profile). Figure 2.3 shows how the magnitude and sign of the error signal (PSD output voltage) depend on the slope of the gain profile, $dI/d\nu$, and to the phase of the intensity modulation relative to the reference.

The servo loop locking circuitry[26] consists of a Burleigh PZT stack attached to a flat high reflector of the OPL resonator, a PAR HR-8 phase sensitive detector tuned to 420 Hz, an integrator-amplifier error circuit and a Spectra-Physics Model 481 Dye Laser Etalon Controller for high voltage amplification. The typical time response of the servo loop is ~50 msec. The stabilized effective linewidth is <15 MHz; the associated intensity variation is <5%. However, in a 1 msec window (the relevant

36

Figure 2.3 Schematic of how the magnitude and phase of the OPL intensity

modulation depend on the location of the OPL cavity mode

beneath its gain profile.

OPL GAIN PROFILE

Applied Voltage

@f

time

(A) IF CAVITY FREQUENCY:

CENTER

@2f

I(OPL)

(B)

RED

@f; $\emptyset_{rel}=0$

(C)

BLUE

@f; $\emptyset_{rel}=\pi$
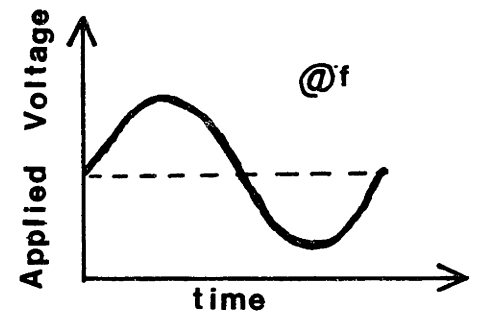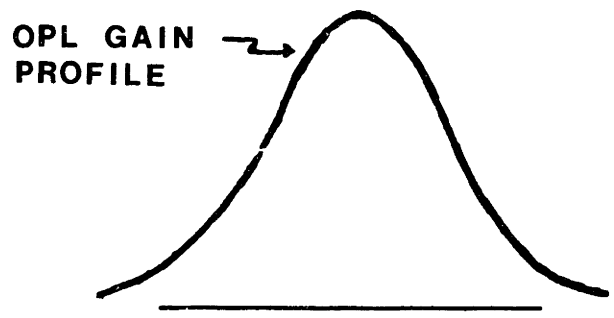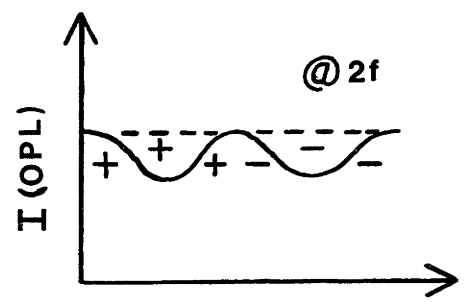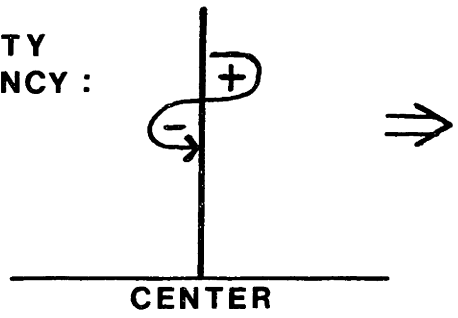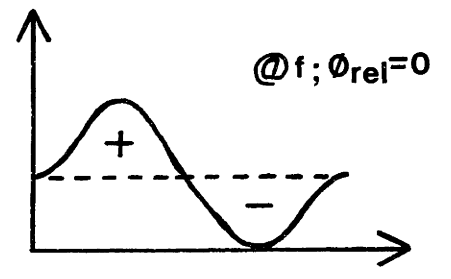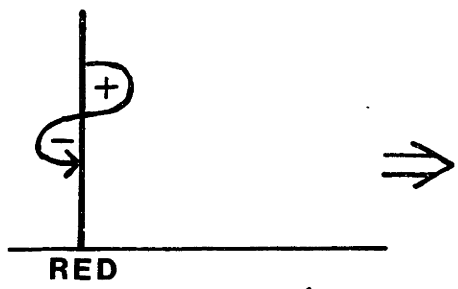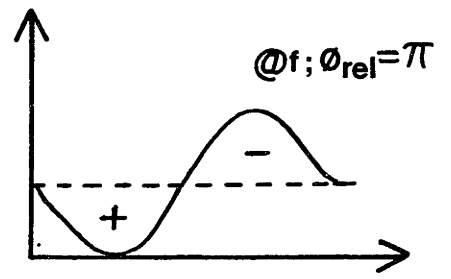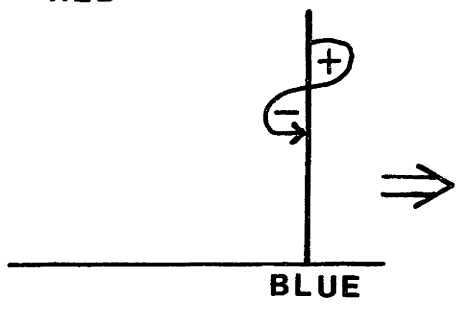
Figure 2.4 Block diagram of the servo loop

AMP
x 10^3

$\int$

SUM

420 Hz
MODULATION

ERROR
SIGNAL

PHASE
SENSITIVE
DETECTOR

PHOTO
DIODE

FLAT REFLECTOR
OF
Na$_2$ OPL

PZT
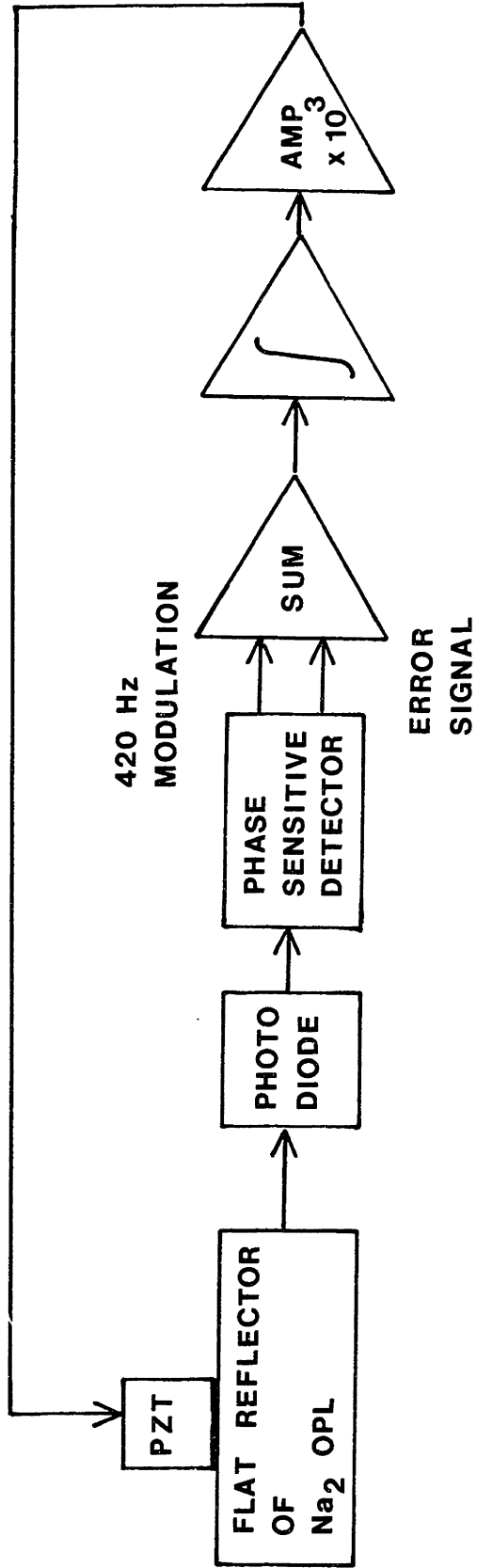
Figure 2.5 A~1 cm^{-1} PROBE scan, with τ~100 msec, shows (a) the main,
in-phase MGS signal and (b) extraneous, out-of-phase signals,
which arise from PUMP-OPL-PROBE schemes different from that of
Figure 2.1. (discussed in section six).

(a)

(b)

360 MHz
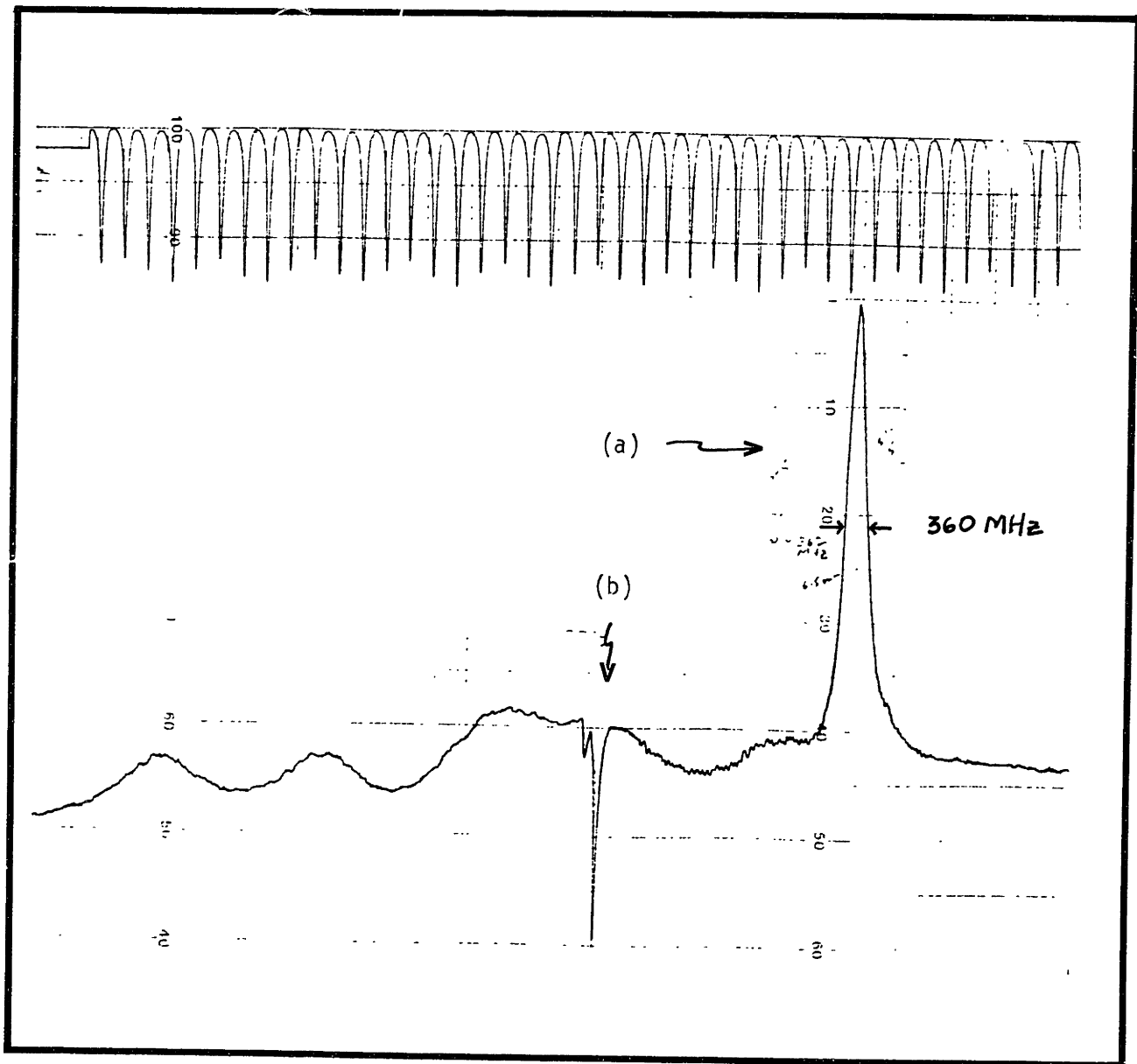
time scale since we detect at the 1 KHz PROBE modulation frequency), the OPL intensity variation is <0.05%.

Figure 2.5 shows an MGS signal which corresponds to a 2% intensity change. We have observed MGS signals spanning a three order-of-magnitude dynamic range (0.1%-100% change in OPL intensity) for probe transitions with Franck-Condon factors from ~10^{-4} to 10^{-1}.

2.4 Heat Pipe

In order to operate the Na_2 optically pumped laser with minimal intensity fluctuations, it is essential to be able to generate the metal vapor in a controlled manner for long periods of time with minimal turbulence. A heat pipe is a standard method of generating metal vapors with well-defined densities, temperatures, and optical path lengths[27-29]. The following sections outline the general principles of a gas-controlled heat pipe and the workings of the particular Na_2 heat pipe used in our experiments.

A. Principles of Operation

A heat pipe is a device characterized by a very high thermal conductance. The basis for the large thermal transmissivity of this device is that the latent heat of vaporization of a liquid is transported throughout by continual evaporation and condensation of that fluid. The heat pipe used in this work consists of a metal pipe whose central portion is enclosed in an oven and both end portions are enclosed in water-cooled jackets. A fine wire mesh lines the inner walls of the pipe and forms the wick structure that plays a crucial role in the operation of the heat pipe. Brewster windows are attached to both ends of the

pipe. The metal to be studied is the working fluid of the heat pipe.

The basic principles of operation are best described with reference to Figure 2.6a, which shows the distribution of working fluid within the wick structure. When the central portion of the pipe is heated, the metal melts and wets the wick. With further heating, the liquid evaporates to produce that vapor pressure that is in equilibrium with the temperature of the pipe. The saturated vapor diffuses towards the cooler ends of the tube, where the vapor pressure is lower, and condenses into a liquid. In the condenser region, the liquid tends to flood the wick thereby producing a large radius of curvature of the meniscus. In the evaporator region, the liquid recedes into the wick thereby greatly reducing the radius of curvature of the meniscus. It is the difference in the radii of curvature of the menisci in the two regions that enables the wick to act as a capillary and return the liquid to the heated portions of the tube. Thus the flow of two phases of the working fluid, following evaporation and condensation, completely circulates the fluid and leads to near-isothermal conditions within the pipe.

Normally, the temperature at which a heat pipe operates is dictated by the power input and the temperature of the condenser. By introducing an inert, noncondensing gas into the system, one can control the pressure, and hence temperature, independently of these external factors. Furthermore, one can operate the heat pipe in a self-regulating mode as is shown below. The underlying principle here is that the presence of the noncondensing gas severely inhibits the condensation of the metal vapor in the region that is occupied by the inert gas. Before start-up, the inert gas fills the pipe. During normal operation, the motion of the

Figure 2.6 (a) Distribution of liquid in a heat pipe, and

(b) use of an inert gas to control the temperature and

pressure of metal vapor in the heat pipe.

Vapor →

Mesh

← Liquid

EVAPORATOR   CONDENSER

Evaporator   Condenser

Gas
Reservoir

Non-condensing gas
cuts off this region
of the condenser
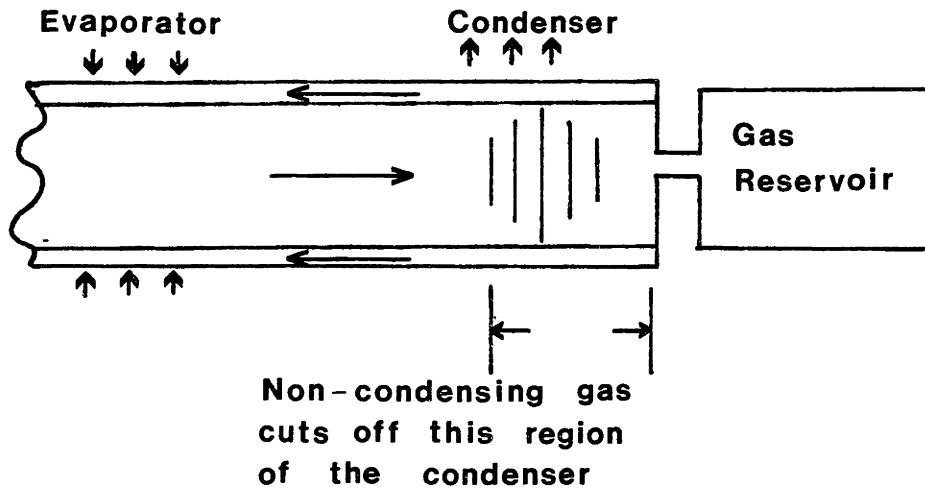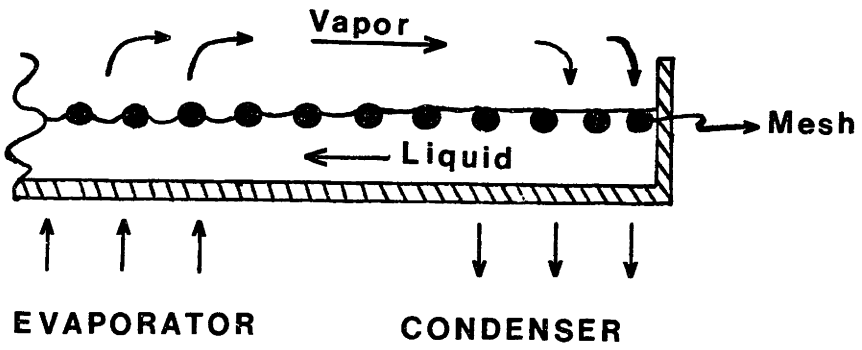
metal vapor "pumps" this inert gas towards the condenser region, thus completely separating the metal vapor and inert gas zones. A steady-state condition is reached when the vapor pressure of the metal becomes equal to the pressure of the inert gas, and the metal/inert gas interface is located near the condenser region (see Figure 2.6b).

It is the mobility of this interface that is primarily responsible for the temperature stability of the gas-controlled heat pipe. If, for example, there occurs an increase in input power, it would cause an increase in vapor pressure, which in turn would tend to compress the noncondensing gas and uncover a larger surface of the condenser. This larger cold surface would serve to dissipate the increased heat input. Similarly, a reduction in input power will cause a decrease in vapor pressure and allow the inert gas to expand towards the evaporator region. This movement will expose less of the condenser region to the metal vapor and thus produce a smaller heat sink to compensate for the lower heat input. The overall effect of the inert gas is to control passively the length of the condenser region in contact with the metal vapor, thus minimizing the temperature response of the heat pipe to variations in input power (i.e. input power changes map into changes in the length of the metal vapor zone rather than changes in its pressure).

To summarize, there are four principal advantages to the generation of metal vapors in heat pipes. First, the entire vapor zone is at a uniform pressure and temperature since the evaporation and condensation processes take place at almost identical temperatures. Second, gas-controlled heat pipes allow the use of an inert gas to sensitively

control the pressure (and hence temperature) of the metal vapor. Third, the inert gas prevents the metal from condensing on the end windows and further acts as transparent layer to optical radiation. Fourth, the continuous evaporation and condensation of the metal serves to distill out (into the condenser region) any impurities.

B. Construction and Operation

The heat pipe used in these experiments is constructed from a 2 inch o.d., type 304, stainless steel pipe with 1/16 inch wall and is ~19 inches long. The wick is constructed from three layers of 100 mesh type 303 stainless steel that is ~17 inches long. Before sodium is added, the heat pipe is baked overnight under vacuum at ~500°C in order to clean the mesh. Typically, 20 grams of reagent grade sodium is used in the pipe.

Power to the heat pipe is supplied by resistive heating of a 1/8 inch o.d. nichrome wire (encased in a stainless steel sheath) brazed to the pipe. Adjacent loops of the wire are separated by ~1 inch and the helix extends over ~12 inches. The temperature of the pipe is monitored by three chromel-alumel thermocouples spot welded along various portions of the pipe.

In order to test for heat pipe operation, one of the end windows was replaced by a ~10 inch long, 1/8 inch o.d. chromel-alumel thermocouple (protected by a stainless steel sheath) which was inserted through an o-ring fitting. In this configuration, the thermocouple could be moved in and out of the vapor zone so as to measure the axial temperature profile for various heater powers and inert gas pressures. Simultaneous readings were made with the external thermocouples.

.

Figure 2.7 Axial temperature profiles of the Na$_2$ heat pipe at three
different input powers.

.

49
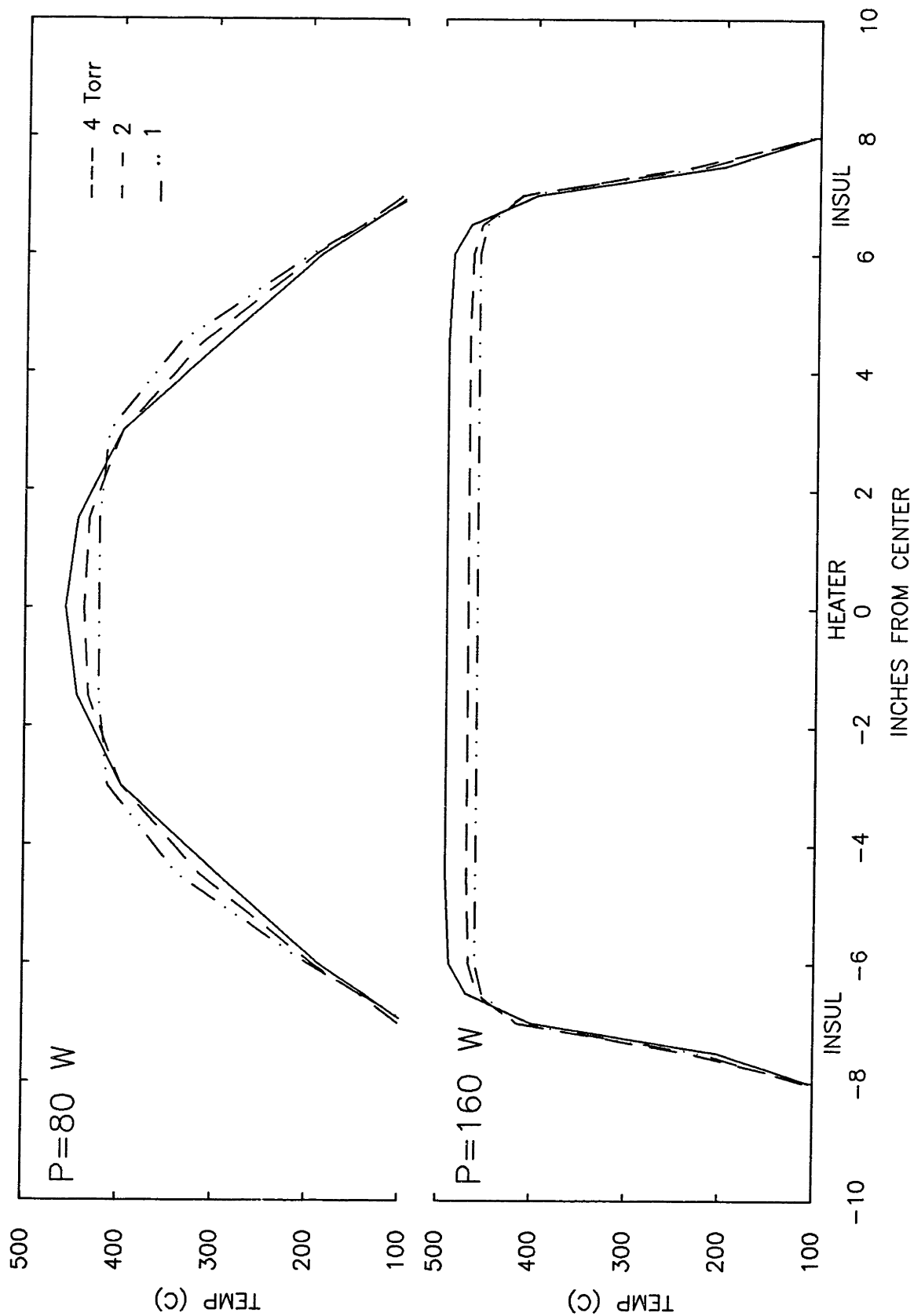
Figure 2.7 shows the measured temperature profiles for a series of input powers, starting from ~80 Watts for which the heat pipe is underpowered, to ~160 Watts for which the flat temperature profiles with sharp edges are evidence of proper heat pipe operation. The onset of "heat piping" is indicated by a lack of dependence of the pipe temperature on heater power; a true heat pipe mode is indicated by a uniform temperature profile with a reasonably well-defined metal/inert gas boundary.

After the heat pipe was tested, the thermocouple was replaced by the end window. The heat pipe was operated at low pressures (~1 Torr) so that the PROBE excitation rate could compete effectively with the collisional depopulation rate in order to maximize the probe-induced change in the OPL output intensity. (Extended operation at pressure lower than 1 Torr was not possible since significant condensation of the metal occured in the cold regions of the pipe.)

2.5 OPL Cavity

Having discussed some aspects of heat pipe operation, let us now consider some particulars of the Na_2 OPL cavity. The radii of curvature and the relative separation of the four reflectors making up the OPL resonator are chosen so as to produce stable resonator modes, with a beam waist of 0.05 cm located within the heat pipe, and a Rayleigh range of ~1 meter. This section is concerned with the calculation of the sizes and locations of the beam waists for the passive, four mirror OPL cavity. To prepare the groundwork for this calculation, we will recapitulate the ABCD transfer matrix formalism for Gaussian beam propagation and transformation by lenses[30].

A. Gaussian Beams

Use of ray (i.e. "geometric" as opposed to "physical") optics to describe the propagation of light is valid only in the limit that the wavelength, $\lambda \to 0$. Geometric optics is further lacking in that it only predicts which resonator configurations are stable, but it gives no information concerning the behavior of stable cavity modes. In order to determine the shapes of these modes, one must consider the effects of diffraction as the radiation field propagates in a resonator.

The paraxial formulation of diffraction is generally an adequate description of radiation typically encountered in lasers. In this limit, one deals with radiation fields propagating along the z direction whose intensity profile, $|U(x,y,z)|^2$, for a given z, varies slowly along the x and y directions. This leads to the paraxial wave equation

$$\nabla^2_{transverse}\psi = i2k \frac{\partial \psi}{\partial z} , \qquad (2.5)$$

which is the central equation for Gaussian beams. The solution to the above equation can be shown to be a modified plane wave, described by the following equation,

$$U(x,y,z) = \psi(x,y,z)\ e^{-ikz} \qquad (2.6)$$

Expressed more fully,

$$\psi = \psi_0\ H_m(\sqrt{2}x/\omega(z))H_n(\sqrt{2}y/\omega(z)) \qquad \times$$

$$\frac{\omega_0}{\omega(z)}\ \exp\{\frac{-(x^2+y^2)}{\omega^2(z)}\} \qquad \times \qquad \text{AMPLITUDE FACTOR}$$

$$\exp\{-ik\frac{(x^2+y^2)}{2R(z)}\} \qquad \times \qquad \text{RADIAL PHASE}$$

$$\exp\{-i[kz-(m+n+1)\tan^{-1}(\frac{\lambda z}{\pi\omega_0^2})]\} \qquad \text{LONGITUDINAL PHASE} \qquad (2.7a)$$

where

$$\omega^2(z) = \omega_0^2 \left[1+\left(\frac{\lambda z}{\pi\omega_0^2}\right)^2\right]$$

$$R(z) = z \left[1+\left(\frac{\pi\omega_0^2}{\lambda z}\right)^2\right] \qquad\qquad (2.7b)$$

The various parameters are illustrated in Figures 2.8 a) and b) and interpreted as follows:

$\omega(z)$ is the beam radius where the field amplitude drops to $1/e$ of its peak value at $r=0$;

$R(z)$ is the radius of curvature of the wavefront (surface of constant phase);

$H_n(\gamma)$ is the nth Hermite polynomial in the variable γ;

m,n are the number of transverse modes.

It is useful to interpret physically the three terms in Equation (2.7a). The first describes the Gaussian radial variation of the amplitude of the field and shows how this changes when the beam diffracts as it propagates along the z direction. Figure 2.8b shows this spreading of the beam from its minimum radius of ω_0 at $z=0$. The second factor, the radial phase factor, indicates the shape of the wave front. We note that the curvature at the center of the wavefront changes as a Gaussian beam propagates since

$$R(z) = z \left[1+\left(\frac{z_0}{z}\right)^2\right] \qquad \text{where } z_0 \equiv \pi\omega_0^2/\lambda \qquad\qquad (2.8)$$

For example, when $z \gg z_0$ the beam appears to originate from $z=0$. However, as $z \to 0$, the center of curvature of the phase front recedes until, at $z=0$, the center of curvature is at infinity and the wavefront is planar. (A

Figure 2.8 Illustration of (a) the Gaussian intensity profile of a laser beam propagating along the z axis, and (b) its diffraction from the beam waist, ω_0. (c) is with reference to Equation (2.10).

B

1/e Field Contour

z=0

ω_0

$|\omega(z)|$

Beam Waist, ω_0

Radius of Phase front, R(z)

A

E

E_0

E_0/e

$|x| = \omega$

x

y

C

$(z_2 - z_1)$

R_1

R_2

z
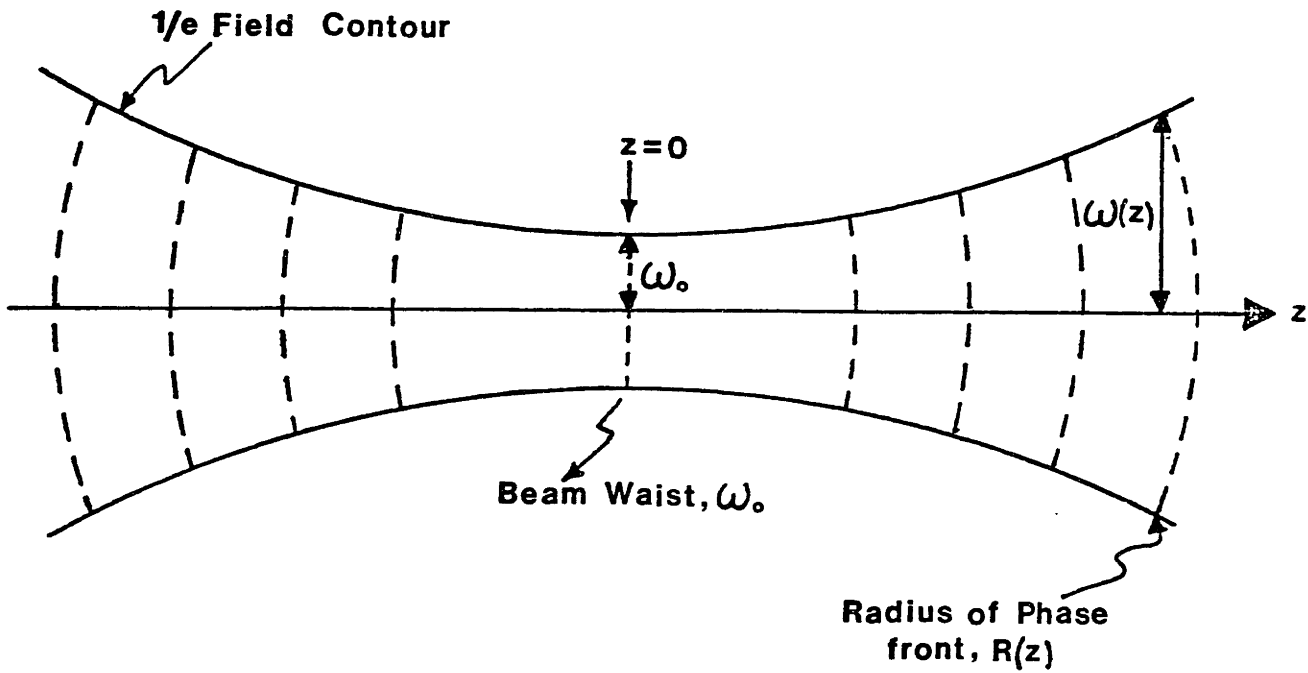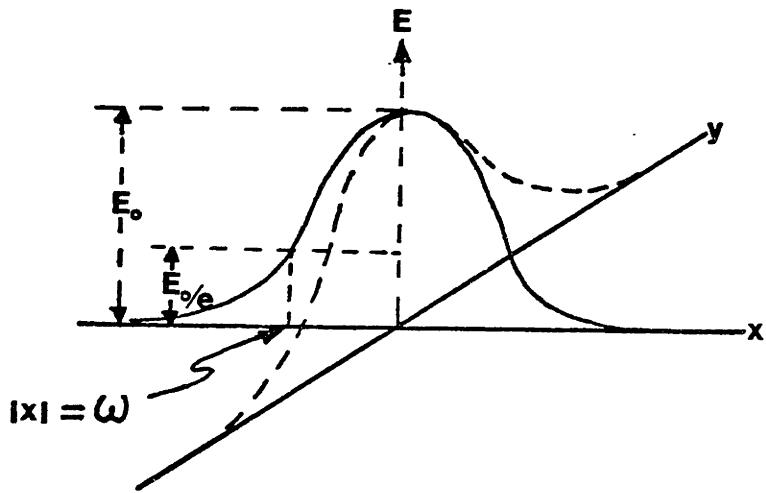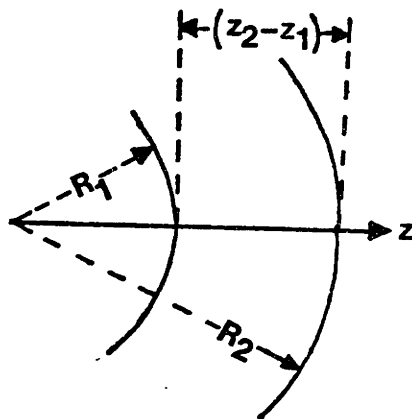
planar wavefront is an alternate definition of the z=0 plane where the beam has a minimum radius.) The third factor in Equation 2.7a is simply the change in phase of the wave along the direction of propagation.

With this description of Gaussian beams, we can now describe their transformations as they propagate through lenses. In order to represent succinctly the characteristics of a Gaussian beam, the parameters ω and R are combined in a complex beam parameter, $q(z)$, which is defined as

$$\frac{1}{q(z)} \equiv \frac{1}{R(z)} - i\frac{\lambda}{\pi\omega^2(z)} \tag{2.9}$$

The propagation of a beam through free space between points z_1 and z_2 can be expressed, in terms of q, as

$$q(z_2) = q(z_1) + z_2 - z_1. \tag{2.10}$$

Equation 2.10 is formally the same as the relationship between wavefronts of spherical waves at z_1 and z_2: $R(z_2) = R(z_1) + (z_2 - z_1)$, as is obvious from Figure 2.8c. Similarly, the radius of curvature of a Gaussian beam transforms in the same way as for spherical waves when propagating through a thin lens of focal length, f,

$$\frac{1}{R_2} = \frac{1}{R_1} - \frac{1}{f} \tag{2.11}$$

where R_1 and R_2 are the radii of curvature directly before and after the lens. Since the beam diameters are unaltered by the lens, that is, $\omega_1=\omega_2$, we get the transformation of q through a lens

$$\frac{1}{q_2} = \frac{1}{q_1} - \frac{1}{f}. \tag{2.12}$$

Application of Equations 2.10 and 2.12 allows one to trace Gaussian beams through any combination of elements which can be broken down into equivalent sequence of thin lenses and free space.

B. ABCD Matrices

A systematic procedure for tracing Gaussian beams, which employs Equations 2.10 and 2.12, involves the ABCD ray transfer matrices[30]. These same matrices appear in ray optics and express the linear relationships (arising from the paraxial approximation) between the position x_1 and slope x_1' of a ray in the input plane of a lens and the corresponding parameters x_2 and x_2' in the output plane of the lens:

$$\begin{bmatrix} x_2 \\ x_2' \end{bmatrix} = \begin{bmatrix} A & B \\ C & D \end{bmatrix} \begin{bmatrix} x_1 \\ x_1' \end{bmatrix} . \tag{2.13}$$

These ABCD matrices can also be used to represent the transformation of a Gaussian beam characterized by the parameter q,

$$q_2 = \frac{Aq_1 + B}{Cq_1 + D} , \tag{2.14}$$

where the elements of the ABCD matrix reflect the properties of the optical medium through which the beam propagates. For example, $C = -1/f$, where f is the focal length of the optic.

Let us illustrate this formalism for beams in laser cavities. The resonant modes of a cavity are those Gaussian beams for which the amplitude and phase of the field repeats itself after one complete pass. Self-consistency in the longitudinal phase defines the allowed frequencies of the stable modes, while self-consistency in the amplitude and radial phase defines the shape of the mode. We will see that, given a frequency,

a mode is completely characterized by the size and location of its beam

waist. For confined Gaussian beams, we require that $q_2 = q_1$ (the second

cycle equals the first cycle through the cavity); therefore, Equation

(2.14) becomes

$$q = (Aq+B)/Cq+D$$

or $1/q = \{D-A + [(A-D)^2 + 4BC]^{1/2}\}/2B$.

where the ABCD elements now represent the properties of the resonator

structure as a unit. Using the fact[30] that AD-BC=1, the two roots of the

above equation are found to be

$$\frac{1}{q} = \frac{D-A}{2B} \pm \frac{i}{2B} \; [4-(A+D)^2]^{1/2} \qquad \qquad (2.15)$$

and, from the definition of q,

$$R(z) = 2B/D-A \qquad \qquad (2.16)$$

$$\omega^4(z) = (\frac{2\lambda}{\pi})^2 \; \frac{B^2}{4-(A+D)^2}$$

Let us apply (2.10)-(2.16) to the example shown in Figure 2.9. The

ABCD matrix for this structure is the ordered product of matrices

representing the propagation of a beam a distance d, followed by

reflection off a mirror of radius R_2, etc. The ABCD matrix elements

allow one to determine R and ω, at the starting point, by using equations

(2.16):

$$R(z) = R_2$$

$$\omega^4(z) = (\frac{\lambda}{\pi})^2 \; \frac{dR_2^2(R_1-d)}{(R_2-d)(R_1+R_2-d)} \; . \qquad \qquad (2.17)$$

Notice that the phase front of the resonator mode exactly matches the

curvature of the mirror, R_2.

We now determine the location, z_0, and size, ω_0, of the beam waist. Let us take the waist to be at the origin. Since the phase front is planar at the waist, q is purely imaginary; therefore, Equation (2.10) gives

$$q(z_0) = q(z_1) - z_1$$

thus $z_1 = \text{Re}\{q(z_1)\}$. $\hspace{3cm}$ (2.18)

Since $q(z_1)$ is given by $R(z_1)$ and $\omega(z_1)$ as determined in Equation (2.17), z_1 is found to be

$$z_1 = \frac{d(d-R_2)}{2d-R_1-R_2} . \hspace{3cm} (2.19)$$

We can now substitute z_1 and $q(z_1)$ back into Equation (2.18) and thus determine $q(z_0)$ and, in turn, ω_0:

$$\omega_0^2 = \left(\frac{\lambda}{\pi}\right) \left[\frac{d(R_1-d)(R_2-d)(R_1+R_2-d)}{(R_1+R_2-2d)^2}\right]^{1/2} . \hspace{1.5cm} (2.20)$$

Another method for determining ω_0 and z_0 from the ABCD elements is with the following relations:

$$\omega_0^2 = \frac{\lambda}{\pi} \cdot -\frac{[4-(A+D)^2]^{1/2}}{2C}$$

$$\hspace{9cm} (2.21)$$

$$z_0 = (A-D)/2C$$

Starting from a knowledge of the beam waist, one can determine the properties of the beam anywhere in the cavity with Equations 2.7b.

C. OPL Resonator Mode

We proceed in exactly the same fashion as in the example of Figure 2.9 to determine the properties of modes supported by the Na_2 OPL cavity of Figure 2.10. This cavity possess two beam waists; their characteristics are as follows:

$\omega_0(1)$ (midpoint of heat pipe) = 0.0579 cm

$\omega_0(2)$ (midpoint of two flat high reflectors) = 0.0527 cm

ω (at M_1 and M_2) = 0.0629 cm

R (at M_1) = 243.4 cm

R (at M_2) = 393.2 cm

The two waists can be thought to arise from the two unfolded cavity configurations shown in Figure 2.10; the first configuration has an effective focal length of 136 cm (therefore C = -7.34 x 10^{-3}) and the second has 113 cm focal length (therefore C = -8.86 x 10^{-3}). The 134 cm longer arm between M_1 and M_2 is intentionally made as short as possible in order to minimize the size of the beam waist within the heat pipe and thus maximize the PUMP power density. The astigmatism produced by the 15° oblique angle of reflection causes only ~0.5% distortion the size of the beam waists.

There are two noteworthy points which distinguish the OPL resonator mode from the example of Figure 2.9. First, there are no beam waists (or planar phase fronts) located at either of the two flat mirrors of the OPL cavity. This is not surprising since the ring resonator supports traveling waves and, like the free propagation of traveling waves through lenses, the wavefront curvature need not coincide with the mirror curvature (unlike the case of standing waves - see Equation (2.17)). Second, the resonance frequency condition is different for traveling waves than for standing waves. The longitudinal phase of the field must repeat itself after one complete pass for all cavities, i.e.,

Figure 2.9 The ABCD matrix elements for a standing-wave resonator.

starting point

$$f_1 = R_1/2 \qquad f_2 = R_2/2$$
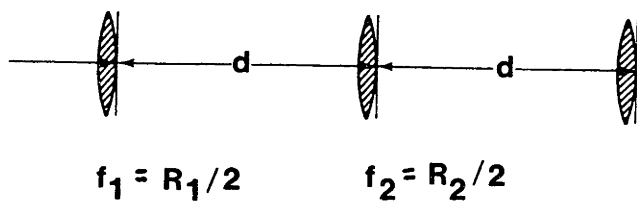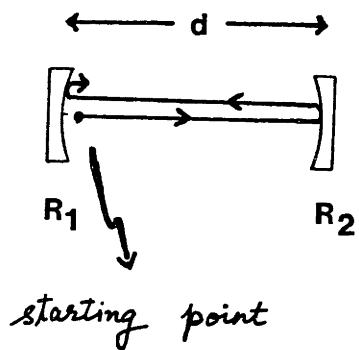
$$\begin{bmatrix} A & B \\ C & D \end{bmatrix} = \begin{bmatrix} 1 & 0 \\ -2/R_1 & 1 \end{bmatrix} \begin{bmatrix} 1 & d \\ 0 & 1 \end{bmatrix} \begin{bmatrix} 1 & 0 \\ -2/R_2 & 1 \end{bmatrix} \begin{bmatrix} 1 & d \\ 0 & 1 \end{bmatrix}$$

$$A = 1 - \frac{2d}{R_2}$$

$$B = 2d - \frac{2d^2}{R_2}$$

$$C = \frac{4d}{R_1 R_2} - \frac{2}{R_1} - \frac{2}{R_2}$$

$$D = 1 - \frac{4d}{R_1} - \frac{2d}{R_2} + \frac{4d^2}{R_1 R_2}$$

62

Figure 2.10 The ABCD matrix elements for the Na$_2$ OPL cavity.

$\omega_o[1]$

M1   **M2**

100

R=300   R=300

59.5   59.5

M3   **M4**

R=∞ $\omega_o[2]$ R=∞

D = 234
θ = 15°

15

UNFOLDED

no.1   no.2

134   100   134
f=150   f=150   f=150   f=150

100   134   100
f=150   f=150   f=150   f=150
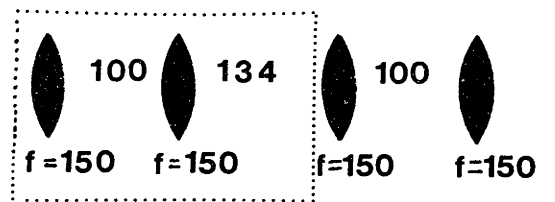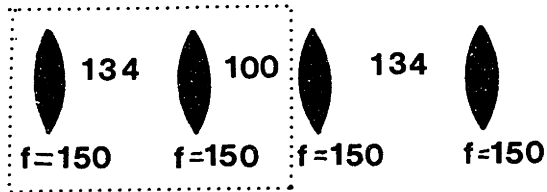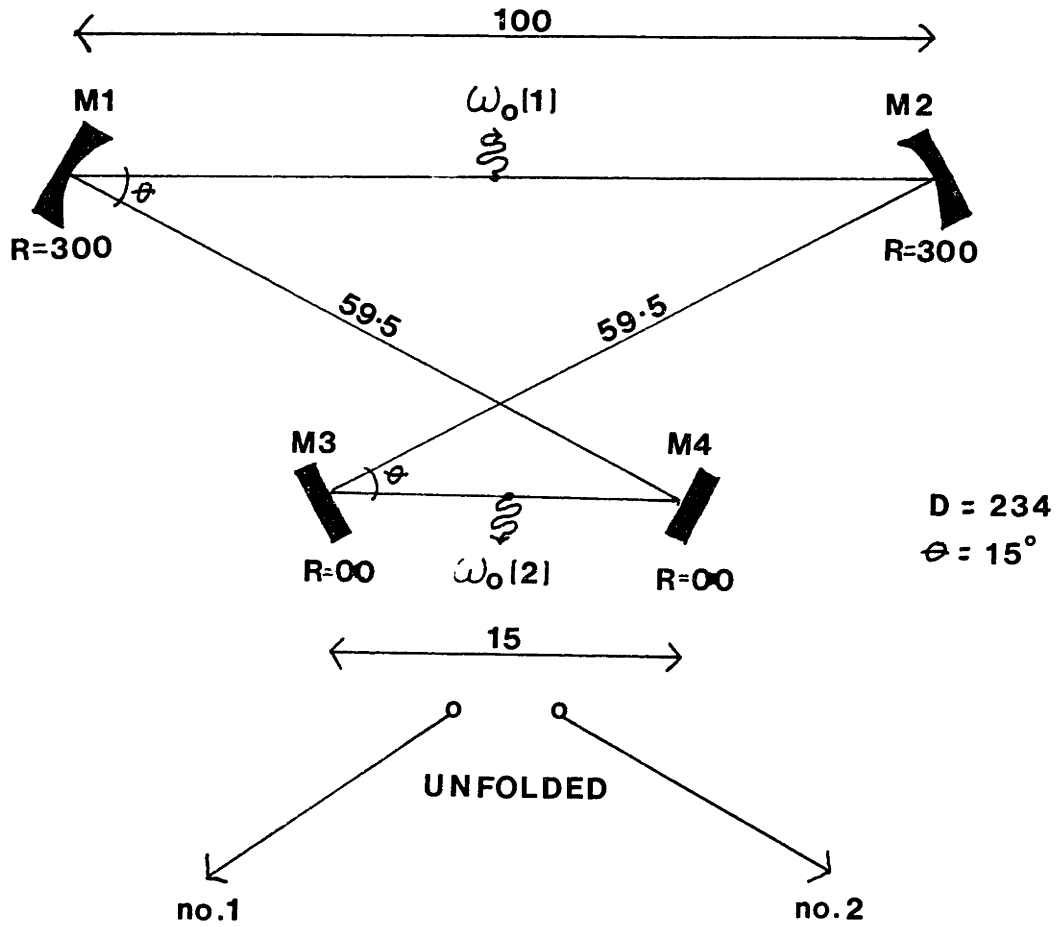
$$\begin{bmatrix} A & B \\ C & D \end{bmatrix} = \begin{bmatrix} -0.629 & 145 \\ -7.34\times10^{-3} & 0.107 \end{bmatrix} \qquad \begin{bmatrix} -0.856 & 145 \\ -8.86\times10^{-3} & 0.333 \end{bmatrix}$$

⇒ $\omega_o = 0.579$ mm
at position 1

⇒ $\omega_o = 0.527$ mm
at position 2

Figure 2.11 Trace 1 shows the I_2 fluorescence excited by the PUMP laser; trace 2 shows two Na_2 OPL transitions and the cavity mode structure within each Doppler-broadened transition.
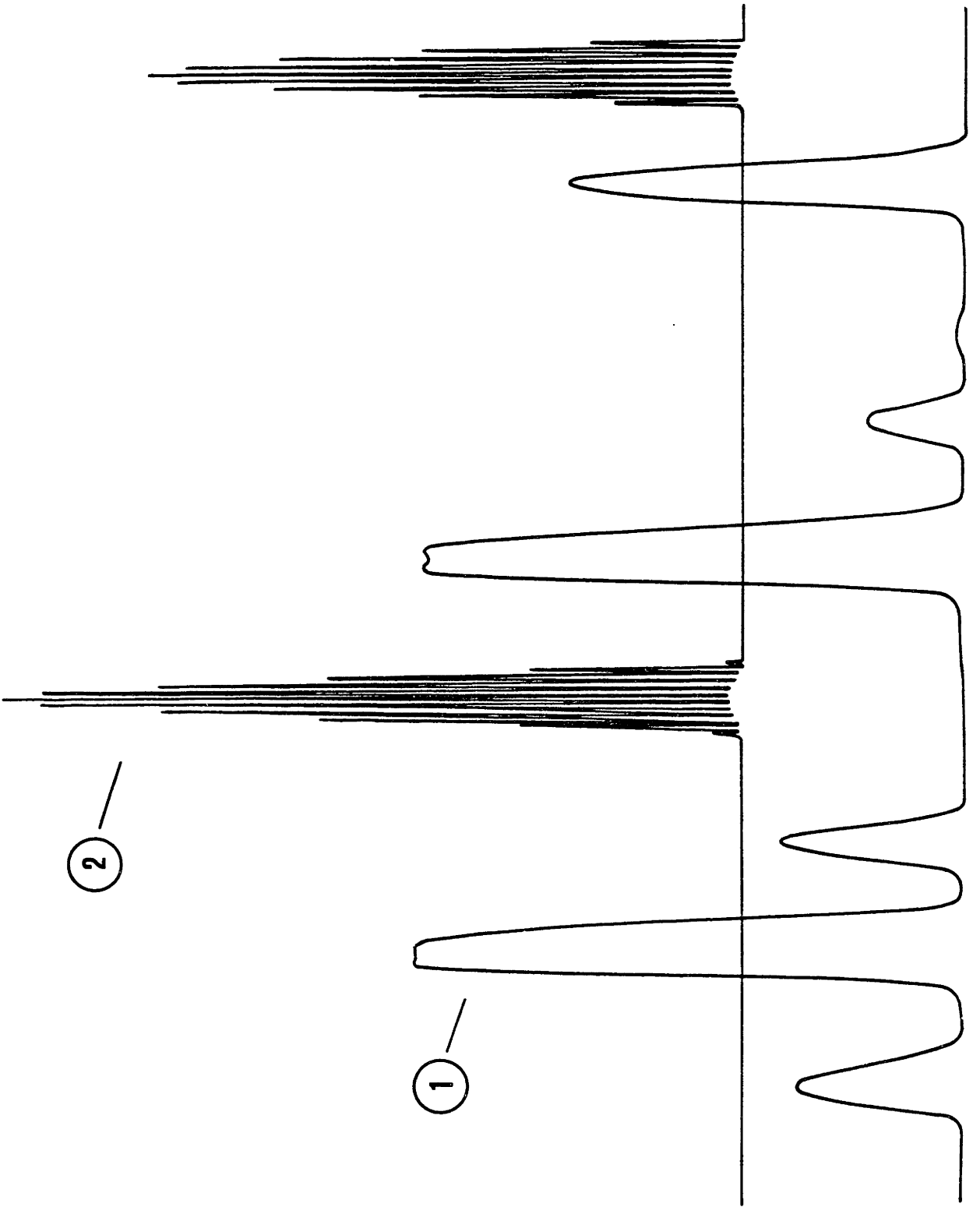
$\Delta\phi = 2\pi k$ where k is an integer (not to be confused with the wave propagation constant)

$$= \frac{2\pi z}{\lambda} - (m+n+1)\tan^{-1}(\frac{\lambda z}{\pi \omega_0^2}) \qquad (2.22)$$

from Equation 2.7a. In a standing wave resonator, an additional boundary condition is imposed: there must be nodes at the mirror surfaces. This leads to the more stringent requirement that the longitudinal phase difference be πk between any two mirrors. Thus,

$\nu = kc/2d$

for the fundamental transverse mode. In traveling wave resonators, where the fields are not retro-reflected back on themselves, the round trip $2\pi k$ phase shift of Equation (2.22) leads to the frequency condition

$\nu = kc/D$

where D is the total length of the cavity.

The 234 cm round trip length of the OPL cavity produces a longitudinal mode separation of 128 MHz. An example of the OPL cavity mode structure, observed as a function of PUMP frequency, is shown in Figure 2.11.

D. Mode-Matching of Resonators

The preceeding section gives the mode structure of the Na_2 OPL resonator. Optimum coupling of the PUMP (and PROBE) radiation into the OPL cavity is accomplished by matching the Gaussian mode of the ring dye lasers (that provide the PUMP and PROBE radiation) with the resonator mode of the OPL. The resonator mode of the CR699 cavity is characterized by the sizes and locations of its beam waists; the three beam waists are calculated[31] and shown in Figure 2.12.

The transformation of the dye laser beam (whose output propagates from waist #3 located 13.6 cm from its output coupler) so that it overlaps with waist #1 of the OPL cavity is accomplished by a thin lens placed between the two optical structures, as illustrated in Figure 2.13. The focal length and placement of this lens must satisfy the equations

$$d_1 = f \pm \frac{\omega_1}{\omega_2} [f^2 - f_0^2]^{1/2}$$

$$d_2 = f \pm \frac{\omega_2}{\omega_1} [f^2 - f_0^2]^{1/2},$$

(2.23)

where $f_0 = \pi\omega_1\omega_2/\lambda$

and d_1 and d_2 are the distances of the lens from the OPL beam waist, ω_1, and the dye laser beam waist, ω_2.

Equations (2.23) can be derived in the following manner. Consider the two general resonators of Figure 2.13a with beam waists ω_1 and ω_2. We require that the Gaussian beam with parameter $q_1 = i\lambda/\pi\omega_1^2$ at the waist of resonator 1 transform into a beam with parameter $q_2 = i\lambda/\pi\omega_2^2$ at the waist of resonator 2 after traversing the lens of focal length f. This means that d_1, d_2 and f for the lens must satisfy the condition:

$$q_2 = \frac{Aq_1 + B}{Cq_1 + D} = \frac{(1 - \frac{d_2}{f})q_1 + (d_1+d_2 - \frac{d_1d_2}{f})}{-(\frac{1}{f})q_1 + (1 - \frac{d_1}{f})} \ .$$

Substituting q_1 and q_2 into the above equation and equating the real and imaginary parts gives

$$\frac{d_1-f}{d_2-f} = \frac{\omega_1^2}{\omega_2^2} \quad \text{and} \quad (d_1-f)(d_2-f) = f^2 - f_0^2.$$

Solving for the two unknowns d_1 and d_2 gives the matching formulas of Equations (2.23).

Equations (2.23) tell us that any lens with a focal length $f > f_0$ can be used to perform the transformation. For an OPL beam waist $w_1 = 0.057$ cm, a dye laser beam waist $w_2 = 0.03$ cm, and the dye laser $\lambda \sim 6000\text{Å}$, the focal length of the lens must be greater than 98.5 cm. A beam-steering high reflector with R = 200 cm (f = 100 cm) is used as the mode-matching lens. Its placement is given by either of the two solutions below [(a) satisfies the "+" solution and (b) satisfies the "-" solution of Equations (2.23)]:

$$\begin{array}{llll} \text{(a)} & d_1 = 130 \text{ cm} & \text{and} & d_2 = 110 \text{ cm} \\ \text{or} & & & \\ \text{(b)} & d_1 = 83 \text{ cm} & \text{and} & d_2 = 90 \text{ cm,} \end{array} \qquad (2.24)$$

where d_1 and d_2 are, respectively, the distances of the OPL and dye laser beam waists from the lens.

If the PUMP radiation were coupled into the OPL through a flat reflector of the OPL cavity, then the distances given above would refer to the separation of the OPL and dye laser beam waists from the surface of the focusing lens. However, the PUMP is coupled through one of the R = 300 cm reflectors of the OPL cavity. This changes the meaning of the above distances so that they now refer to the principal planes of the "thick lens" formed by the f = 100 cm lens and the f = 150 cm (R = 300 cm) reflector. When these two elements are separated by 100 cm (thus possessing an effective f = 100 cm), the two principal planes are located as shown in Figure 2.13b. We found the distances given by Equation (2.24a) to be the more practial ones to use. Figure 2.13b shows that the actual distance d_1 between the OPL beam waist and the principal

Figure 2.12 The size and location of the three beam waists in the CR699 dye laser.

OUTPUT MIRROR, FLAT

$3^{\underline{rd}}$ waist

$3^{\underline{rd}}$ waist

57

66

22

15 cm R

$2^{\underline{nd}}$ waist

10 cm R

8

10 cm R

5

$1^{\underline{st}}$ waist
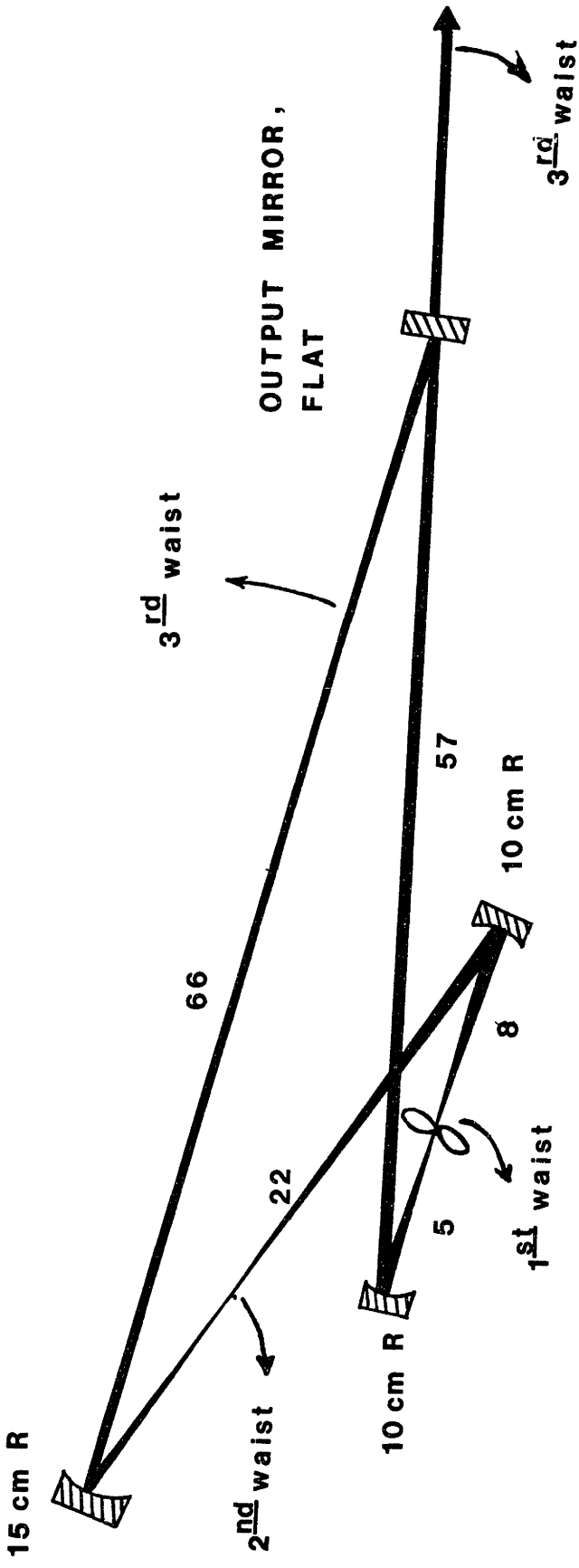
WAIST	SIZE $\left[\begin{matrix}\text{in plane}\\ \bot\end{matrix}\right]$	POSITION
ω_1	1.90×10^{-3} 1.88	JET, 5cm down from tweeter
ω_2	3.31×10^{-3} 3.45	RHOMB, 8cm from upper fold
ω_3	3.5×10^{-2} 3.3	13.6 cm from (or outside) output mirror

Figure 2.13   Mode-matching of the CR-699 dye laser and the Na_2 OPL.

$2\omega_2$

d_1

f

d_1

$2\omega_1$

A

CR 699 DYE LASER
$\lambda \sim 6000\text{Å}$

$\omega_2 \sim 0.03$

$\text{M} \sim 1/4.8$

75

$f_2 = 100$

100

66.7

ℓ_1

ℓ_2
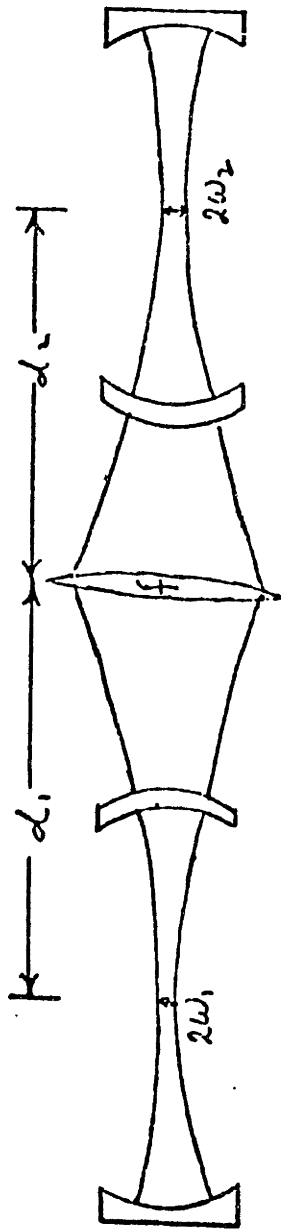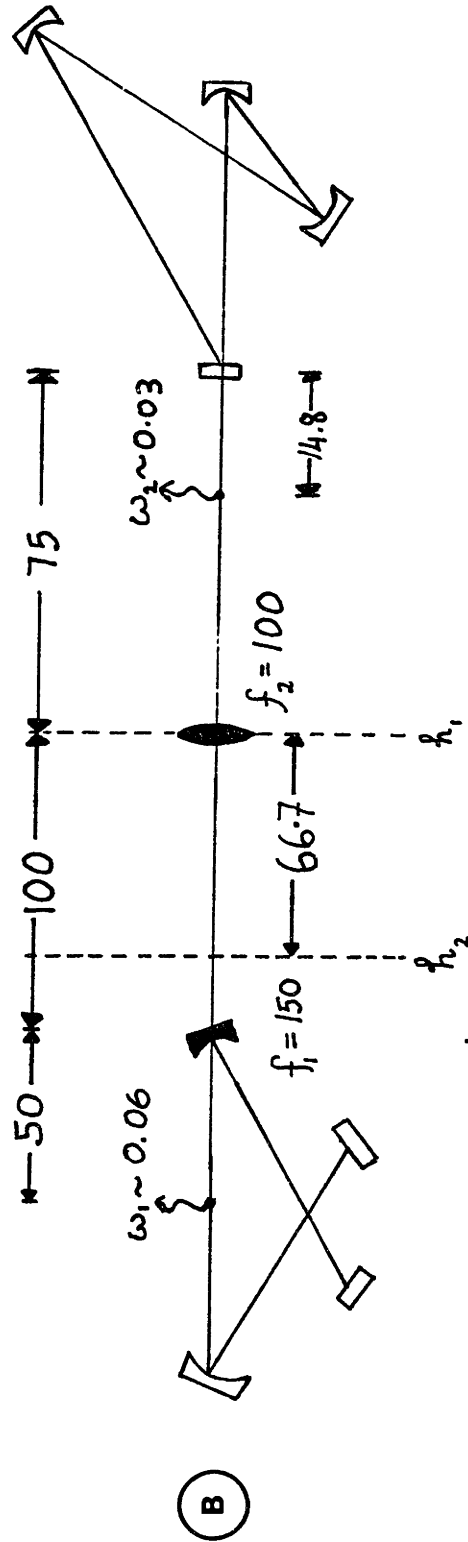
MODE MATCHING LENSES

$f_1 = 150$

50

$\omega_1 \sim 0.06$

Na$_2$ OPL

B

plane h_1 is 20 cm larger than the prescribed 130 cm. While this causes
some coupling loss, it still allows adequate mode-matching of the PUMP
and OPL resonators.

2.6 Variety of MGS Signals

Throughout this thesis, we are concerned with a small class of MGS
signals that correspond to the PUMP-OPL-PROBE excitation scheme of Figure
2.1, in which the PROBE laser excites population from the lower Na_2 OPL
level to the vibrational levels of either the $A^1\Sigma_u^+$ or $B^1\Pi_u$ states and
thus alters the gain of the OPL system. In general, the PROBE laser can
change the OPL gain by interacting with population in anyone of the three
levels participating in the PUMP-OPL scheme. Some examples of the
resulting MGS signals observed are shown in Figures 2.14.

We used two key features of these MGS signals to provide guidelines
to their identity - the phase, relative to the PROBE amplitude
modulation, and the fullwidth. Consider, for example, the excitation
schemes of type A or B where the PROBE removes population from
respectively the upper OPL level or the lower PUMP level. The OPL
intensity decreases that occur concommitantly with these PROBE
excitations are phase shifted by π with respect to the reference. Thus
these types of MGS signals are easily distinguished from those in-phase
signals corresponding to the excitation scheme of Figure 2.1. The type A
and B signals can be distinguished from each other by their different
linewidths. The nearly Doppler-broadened fullwidth (~1.5 GHz) of the
type B signal is due to the thermal axial velocity distribution in the
lower PUMP level whereas the 300-400 MHz fullwidth of the type A signal
is due to the narrow velocity spread in the upper OPL level that is

prepared by the narrow bandwidth PUMP. We note that collisional satellites arising from PROBE interaction with rotational levels collisionally coupled to the lower PUMP or upper OPL level are also observed. (The maximum $\Delta J \approx 8$ at 1 torr).

Opposite to the type A scheme, the PROBE can also excite population into the upper OPL level from thermally populated levels of the ground state. The resulting in-phase MGS signals are observed to be Doppler-broadened.

We finally note one additional mechanism whereby the PROBE can modulate the gain of the OPL. When the OPL frequency coincides with a molecular transition frequency and is partially absorbed by thermal population, then self-absorption is clearly a loss mechanism for the OPL system. Reducing this loss will result in an increase of the OPL intensity. Shown in Figure 2.14, as a type C signal, is an example of the in-phase MGS signal observed when the PROBE laser excites that thermal population that is absorbing the OPL radiation.

Figure 2.14 Examples of various types of MGS signals.
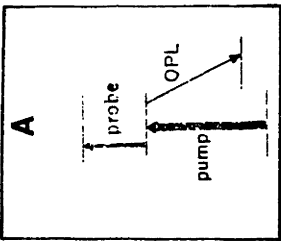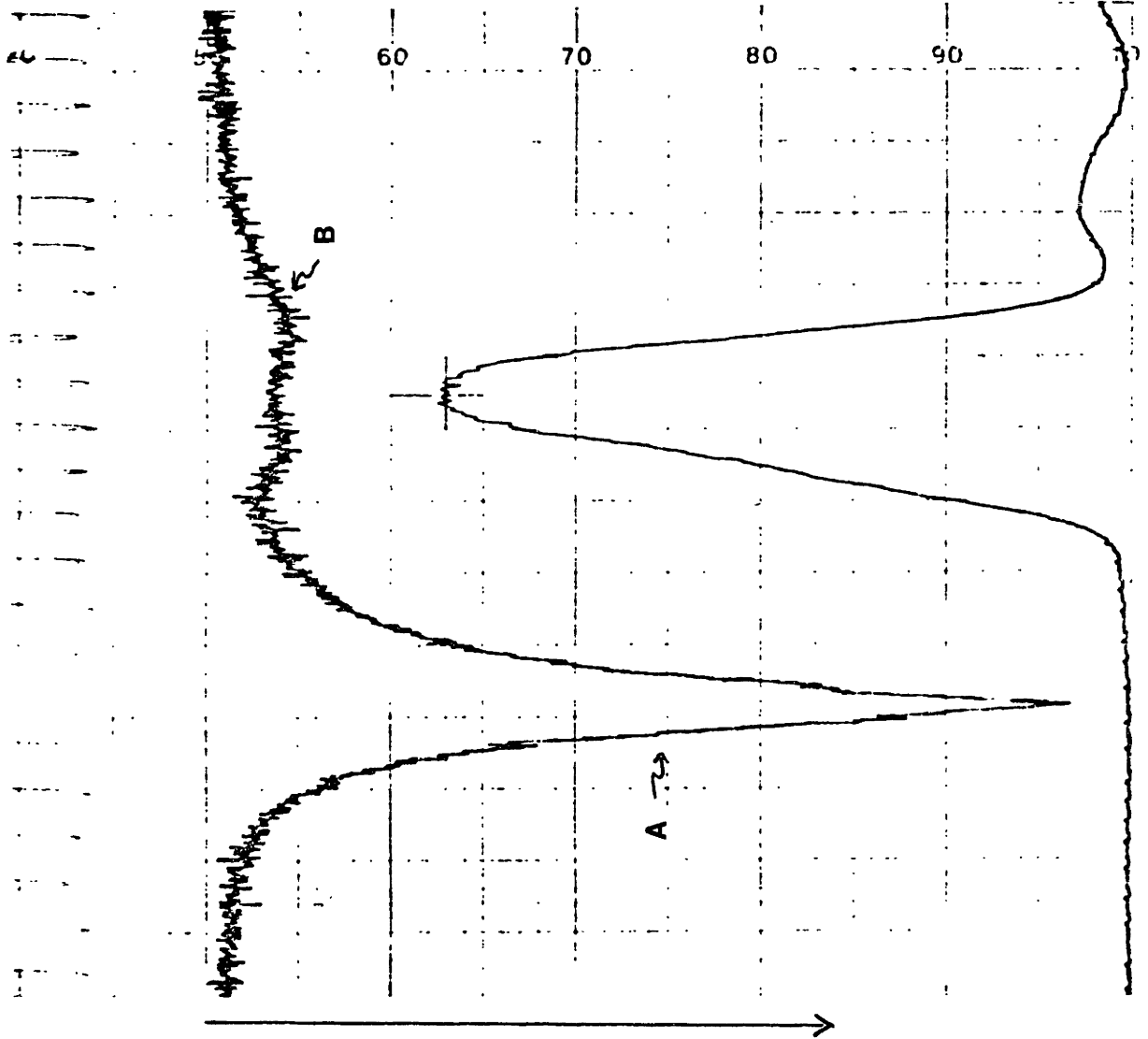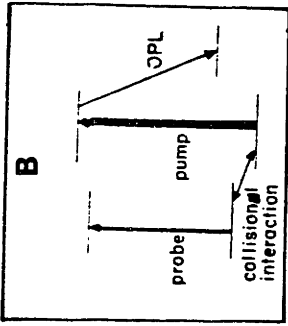
Decrease
in
OPL
Intensity
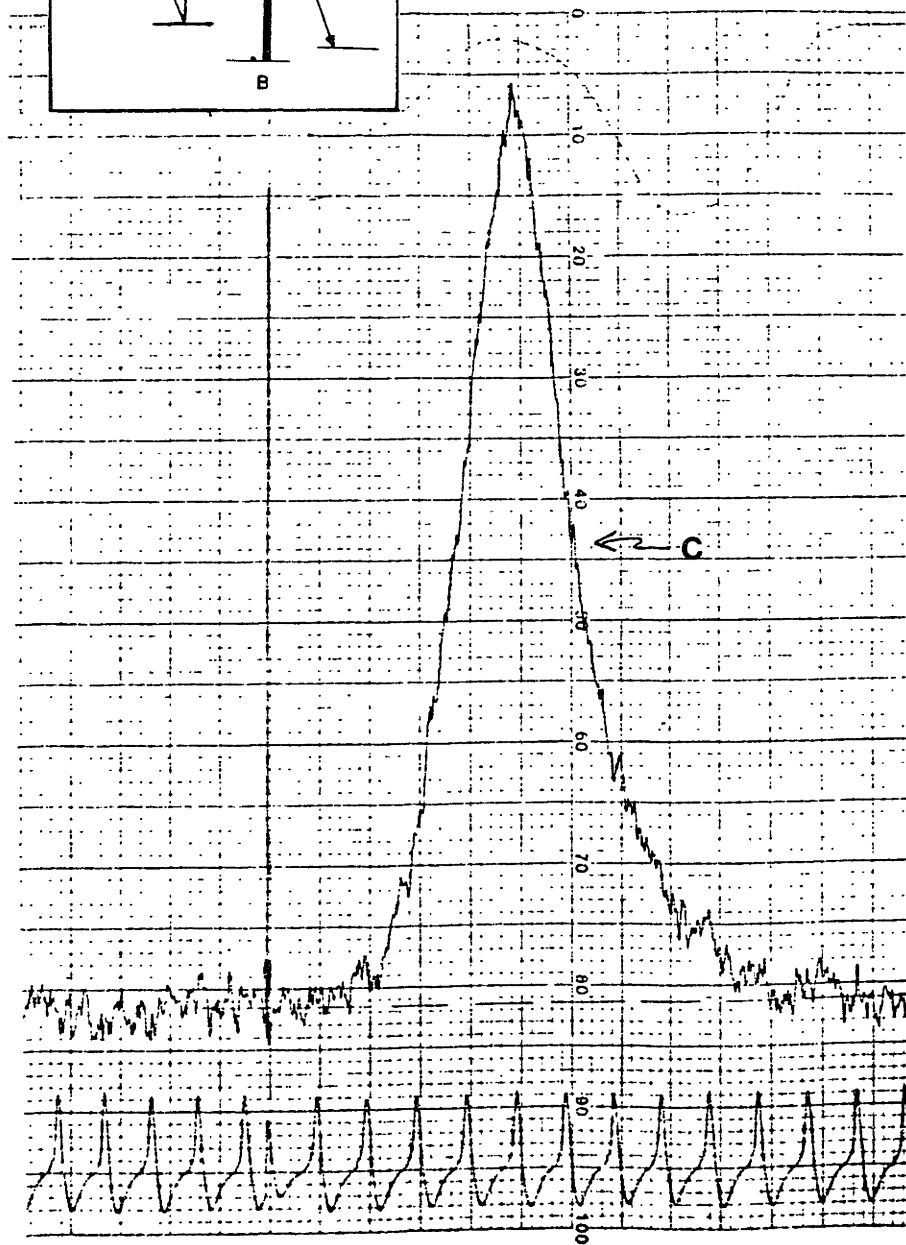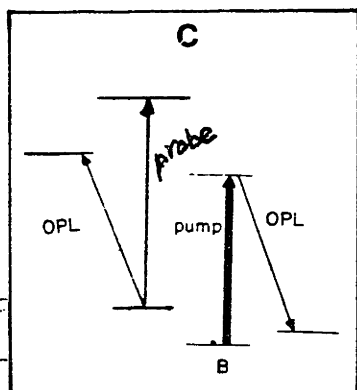
CHAPTER THREE

OVERVIEW OF VAN DER WAALS COEFFICIENTS

3.1 Introduction

This chapter provides a basic perspective on the interrelationships existing between C_n coeffecients (of the R^{-n} terms in long range potential expansions) for molecular states dissociating to the same atomic limit. Some attention is given to the origin and consequences of the degeneracy present in the Na (^{2}S) + Na (^{2}P) atomic limit, which gives rise to the Na_2 A $^1\Sigma_u^+$ and B $^1\Pi_u$ molecular states considered in this thesis. We begin with a general treatment of electrostatic interactions between two non-overlapping arbitrary charge distributions, since the essential behavior of long range potentials is determined by such interactions between separated atoms.

3.2 Multipole Expansions

For the sake of generality, let us begin by considering the electrostatic interaction energy between two distinct and arbitrary charge distributions, A and B. The treatment that follows is largely standard and can be found in references 32, 33; it is included here because it is central to the understanding of the R^{-1} power series expansion of long-range potential energies. The interaction energy, W, between A and B can be viewed as the interaction of the charge density of B, $\rho_B(x)$, with the effective potential of A at the site of system B, ϕ_A,

$$W = \int \rho_B(x)\phi_A(x) \; d^3x \qquad\qquad (3.1)$$

where the integration is performed over the coordinates of charge distribution B. Before examining the interaction between two charge distributions, let us first examine the potential generated by one arbitrary charge distribution, at some point $\vec{r}$ outside the distribution.

For a point charge e located at $\vec{r}'$, the electrostatic potential at $\vec{r}$ is given by

$$\phi(\vec{r}) = e/|\vec{r}-\vec{r}'| . \tag{3.2}$$

Similarly for a distribution with charge density $\rho(\vec{r}')$, the electrostatic potential at $\vec{r}$ is given by

$$\phi(\vec{r}) = \int \frac{\rho(\vec{r}')}{|\vec{r}-\vec{r}'|} d^3r' . \tag{3.3}$$

Using the law of cosines (see Figure 3.1a), we can rearrange $1/|\vec{r}-\vec{r}'|$ in the following manner,

$$\frac{1}{|\vec{r}-\vec{r}'|} = \frac{1}{[(\vec{r}-\vec{r}')^2]^{1/2}} = \frac{1}{[r^2-2rr'\cos\Theta+r'^2]^{1/2}}$$

$$= \frac{1}{r[1- 2\frac{r'}{r}\cos\Theta + (\frac{r'}{r})^2]^{1/2}} \tag{3.4}$$

Examination of (3.4) shows that it has the form of the generating function, $(1-2xt+t^2)^{-1/2}$, for the Legendre polynomials, $P_t(x)$. Therefore, if the potential is measured at a point, $\vec{r}$, well outside the the distribution, $\vec{r}'$, then equation (3.4) can be expanded to yield

$$\frac{1}{|\vec{r}-\vec{r}'|} = \frac{1}{r} \sum_\ell (\frac{r'}{r})^\ell P_\ell(\cos\Theta), \qquad r' < r \tag{3.5}$$

Further, by making use of the spherical harmonic addition theorem, (see Figure 3.1b), we get

Figure 3.1 Coordinate Systems a) and b) for Equations (3.3) and (3.6)

respectively.

(A)
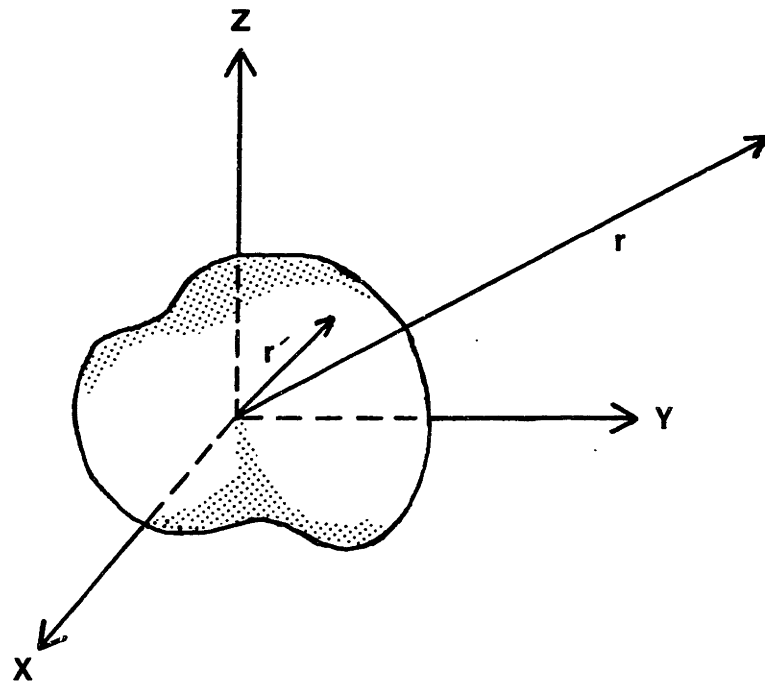
(B) $\quad P_\ell(\cos\Theta) = \dfrac{4\pi}{2\ell+1} \displaystyle\sum_m Y_\ell^{m*}(\theta',\phi') Y_\ell^m(\theta,\phi)$
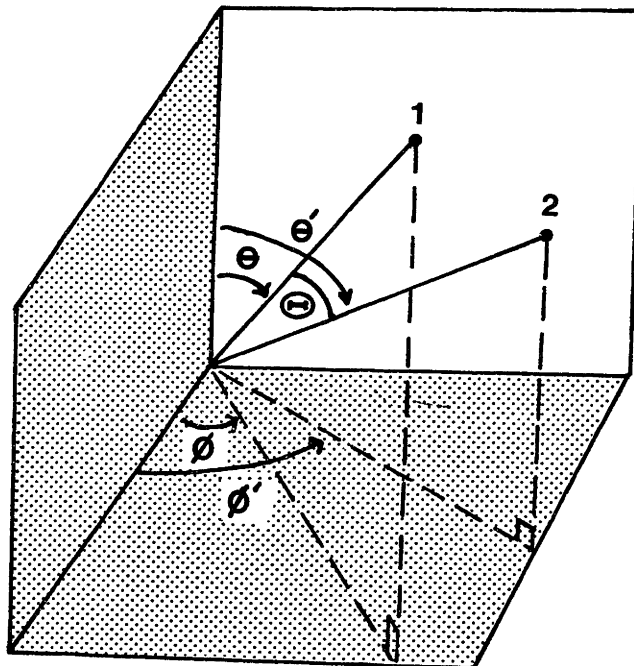
Table 3.1 Spherical components of the first three multipole moments
(from Ref. 32).

q is the total charge,

$$q_0^o = \frac{1}{\sqrt{4\pi}} \int d^3x' \, \rho(\vec{r}') = \frac{1}{\sqrt{4\pi}} q ,$$

$\vec{p} = \int d^3x' \, \vec{r}' \, \rho(\vec{r}')$ is the dipole moment,

$$q_1^1 = -\sqrt{\frac{3}{8\pi}} \int d^3x' \, r'\sin\theta' \, e^{-i\varphi'} \rho(\vec{r}')$$

$$= -\sqrt{\frac{3}{8\pi}} \int d^3x' \, (x'-iy') \, \rho(\vec{r}')$$

$$= -\sqrt{\frac{3}{8\pi}} (p_x - ip_y) ,$$

$$q_1^o = \sqrt{\frac{3}{4\pi}} \int d^3x' \, r' \cos\theta' \, \rho(\vec{r}')$$

$$= \sqrt{\frac{3}{4\pi}} p_z ,$$

$Q_{ij} = \int d^3x' \, (3x_i'x_j' - r'^2\delta_{ij}) \, \rho(\vec{r}')$ is the quadrupole moment tensor

$$q_2^2 = \frac{1}{4}\sqrt{\frac{15}{2\pi}} \int d^3x' \, r'^2\sin^2\theta' \, e^{-2i\varphi'} \rho(\vec{r}')$$

$$= \frac{1}{4}\sqrt{\frac{15}{2\pi}} \int d^3x' \, (x'-iy')^2 \rho(\vec{r}')$$

$$= \frac{1}{12}\sqrt{\frac{15}{2\pi}} (Q_{11} - 2iQ_{12} - Q_{22}) ,$$

$$q_2^1 = -\sqrt{\frac{15}{8\pi}} \int d^3x' \, r'^2\sin\theta' \cos\theta' \, e^{-i\varphi'} \rho(\vec{r}')$$

$$= -\sqrt{\frac{15}{8\pi}} \int d^3x' \, (x'-iy')z' \, \rho(\vec{r}')$$

$$= -\frac{1}{3}\sqrt{\frac{15}{8\pi}} (Q_{13} - iQ_{23}) ,$$

$$q_2^o = \frac{1}{2}\sqrt{\frac{5}{4\pi}} \int d^3x' \, r'^2(3\cos^2\theta' - 1) \, \rho(\vec{r}')$$

$$= \frac{1}{2}\sqrt{\frac{5}{4\pi}} \int d^3x' \, (3z'^2 - r'^2) \, \rho(\vec{r}')$$

$$= \frac{1}{2}\sqrt{\frac{5}{4\pi}} Q_{33} ,$$

This page left intentionally blank.

$$P_{\ell}(\cos\Theta) = \frac{4\pi}{2\ell+1} \sum_m Y_{\ell}^{m*}(\theta',\phi') Y_{\ell}^m(\theta,\phi) \ , \tag{3.6}$$

thus
$$\frac{1}{|\vec{r}-\vec{r}'|} = 4\pi \sum_{\ell,m} \frac{1}{2\ell+1} r'^{\ell} Y_{\ell}^{m*}(\theta',\phi') \frac{1}{r^{\ell+1}} Y_{\ell}^m(\theta,\phi) \ . \tag{3.7}$$

The effective potential at $\vec{r}$ now becomes

$$\phi(\vec{r}) = 4\pi \sum_{\ell=0}^{\infty} \sum_{m=-\ell}^{\ell} \frac{1}{2\ell+1} q_{\ell}^m \frac{Y_{\ell}^m(\theta,\phi)}{r^{\ell+1}} \tag{3.8}$$

where

$$q_{\ell}^m = \int Y_{\ell}^{m*}(\theta',\phi') \vec{r}'^{\ell} \rho(r') \, d^3x' \ . \tag{3.9}$$

The representation of the potential, $\phi(\vec{r})$, in Equation (3.8) in terms of a multipole expansion allows one to identify clearly the separate contributions of each multipole, q_{ℓ}^m, to the total potential. It is readily seen that the potential created by each multipole has a very different angular distribution and dependence on r, in the sense that the potential generated by terms with larger ℓ has a more complicated angular distribution and decays more rapidly with increasing r. The various multipole moments correspond physically to the total charge, q_0^0, the the dipole moment, q_1^m, the quadrupole moment, q_2^m, and so on. These low These low order moments are evaluated in Table 3.1. A useful mnemonic for the generation of a multipole moment of order 2^{ℓ} is to start with two multipoles of the next lowest order, $2^{\ell-1}$, that have opposite signs, and displace one from the other by some distance. For example, a dipole can be created by taking two point charges of opposite sign and separating them by some distance; a quadrupole can be created by taking two dipoles of opposite sign and displacing them in either one of two orthogonal

directions to yield a linear or square quadrupole; etc..

When substituting the low order moments of Table 3.1 into Equation (3.8), the potential can be reexpressed in the more familiar form,

$$\phi(\vec{r}) = \frac{q}{r} + \frac{\vec{p}\cdot\vec{r}}{r^3} + \frac{1}{2} \sum_{i,j} Q_{ij}\frac{x_i x_j}{r^5} + \cdots .$$

(3.10)

Knowing the properties of the potential set up by an arbitrary charge distribution, we can address our original problem of determining the interaction energy between two charge distributions, as given by Equation (3.1). If we assume that the effective potential of distribution A, ϕ_A, does not vary rapidly over the volume of distribution B, then we can expand ϕ_A in a Taylor series

$$\phi_A(x) = \phi_A(0) + \sum_i \frac{\partial \phi_A(0)}{\partial x_i} x_i + \frac{1}{2!} \sum_i \sum_j \frac{\partial^2 \phi_A(0)}{\partial x_i \partial x_j} x_i x_j + \cdots$$

(3.11)

The expansion is about the origin of distribution B; therefore, the x_i's and x_j's refer to the coordinates of B. Since the electric field is given by $\vec{E}_A = -\vec{\nabla}\phi_A$,

$$\phi_A(x) = \phi_A(0) - \vec{x}\cdot\vec{E}_A(0) - \frac{1}{2} \sum_i \sum_j \frac{\partial E_{Aj}(0)}{\partial x_i} x_i x_j + \cdots .$$

(3.12)

The electric field, $\vec{E}_A$, external to distribution A must obey

$$\vec{\nabla}\cdot\vec{E}_A = 0$$

(3.13)

since $\vec{E}_A$ is produced by sources outside the region of interest, B. Therefore, we can subtract $\{1/6\ r^2(\vec{\nabla}\cdot\vec{E}_A)\}$ from the third term in Equation (3.12) thereby obtaining

$$\phi_A(x) = \phi_A(0) - \vec{x}\cdot\vec{E}_A(0) - \frac{1}{6}\sum_i\sum_j (3x_ix_j - r^2\delta_{ij})\frac{\partial E_{Aj}(0)}{\partial x_i} + \cdots . \quad (3.14)$$

Substituting the definitions of the multipole moments of distribution B into the above equation, we find the interaction energy, W, between distributions A and B to be

$$W = q_B\phi_A - \vec{p}_B\cdot\vec{E}_A - \frac{1}{6}\sum_i\sum_j (Q_{ij})_B \frac{\partial E_{Aj}}{\partial x_i} + \cdots . \quad (3.15)$$

Notice the characteristic manner in which the multipoles of B interact with the electric field of A: the charge with the potential, the dipole with the electric field, the quadrupole with the gradient of the electric field, etc.; the $2^{\ell th}$ multipole interacts with the $(\ell-1)^{th}$ spatial derivative of an external electric field.

As an example of the applicability of equation (3.15), consider the interaction of the two dipoles, $\vec{p}_1$ and $\vec{p}_2$. The interaction energy, W_{dd}, must be of the form

$$W_{dd} = - \vec{p}_1\cdot\vec{E}_{p_2} . \quad (3.16)$$

Since $\vec{E}_{p_2} = - \vec{\nabla}\phi_{p_2}$ and $\Phi_{p_2} = (\vec{p}_2\cdot\vec{r})/r^3$, from equation (3.10), we have

$$\vec{E}_{p_2} = - \vec{\nabla}(\frac{\vec{p}_2\cdot\vec{r}}{r^3})$$

$$= -\frac{1}{r^3}\vec{\nabla}(\vec{p}_2\cdot\vec{r}) - (\vec{p}_2\cdot\vec{r})\vec{\nabla}(\frac{1}{r^3})$$

$$= -\frac{1}{r^3}(\vec{p}_2) - (\vec{p}_2\cdot\vec{r})(-\frac{3\vec{r}}{r^5})$$

$$\therefore \quad W_{dd} = \frac{\vec{p}_1 \cdot \vec{p}_2}{r^3} - \frac{3(\vec{p}_1 \cdot \vec{r})(\vec{p}_2 \cdot \vec{r})}{r^5}$$

$$= \frac{\vec{p}_1 \cdot \vec{p}_2 - 3(\vec{p}_1 \cdot \hat{r})(\vec{p}_2 \cdot \hat{r})}{r^3} \qquad (3.17)$$

We see that dipole $\vec{p}_1$ interacting with the electric field of dipole $\vec{p}_2$ has an R^{-3} energy dependence. It can be shown in a similar fashion that dipole $\vec{p}_1$ interacting with the electric field of quadrupole $\overleftrightarrow{Q}_2$ has an R^{-4} energy dependence; a charge q_1 interacting with the potential of a dipole $\vec{p}_2$ has an R^{-2} energy dependence; a quadrupole $\overleftrightarrow{Q}_1$ interacting with the gradient of the electric field set up by quadrupole $\overleftrightarrow{Q}_2$ has an R^{-5} energy dependence, etc. Thus the electrostatic interaction energy $W(A-B)$ of two arbitrary charge distributions A and B can be represented by a power series in R^{-1}, and the coefficients of the various orders of R^{-1} reflect the magnitudes and relative orientations of the multipoles of distributions A and B.

3.3 Long Range Potentials

The preceding discussion of electrostatic interactions is important to any discussion of long range potentials: it is essentially the multipolar interactions between separated atoms A and B that are responsible for the long range behaviour of internuclear potentials of the diatomic molecule, AB. In the long range limit, where there is negligible ovelap of atomic wavefunctions and the magnitude of the electrostatic interaction energy is significantly less than the energy difference between states of the separated atom, the following perturbation theoretic approach is appropriate.

The basis functions consist of products of separated atom wavefunctions and the multipolar interactions are treated as perturbations on the zero-order system (which consists of two noninteracting atoms at infinite separation). The resulting first and second order corrections to the energy generally provide a complete description of the long range portions of the potentials of various molecular states of the AB molecule.[34-37]

A. First-Order Corrections

Let us begin by considering the first-order contribution to the long range potential energy of the heteronuclear diatomic molecule AB, formed from the combination of atom A in state 0 and atom B in state 1. The zero-order energy and wavefunction are, respectively, $E^{(0)} = \varepsilon_{A_0} + \varepsilon_{B_1}$ and $|\psi^0\rangle = |A_0\rangle|B_1\rangle$. For two neutral atoms, the leading electrostatic interaction is of the dipole-dipole form, W_{dd}; therefore, the first-order correction to the energy, with W_{dd} acting as the perturbation, is

$$E^{(1)} = \langle A_0 B_1 | W_{dd} | A_0 B_1 \rangle \ .$$

Choosing the internuclear axis of the AB molecule as the z direction, we can express W_{dd} of Equation 3.17 as

$$W_{dd} = \frac{\mu_{x_A}\mu_{x_B} + \mu_{y_A}\mu_{y_B} - 2\mu_{z_A}\mu_{z_B}}{R^3} \ . \tag{3.18}$$

Thus $E^{(1)} = \dfrac{e^2}{R^3}\{\langle A_0|x_A|A_0\rangle\langle B_1|x_B|B_1\rangle + \langle A_0|y_A|A_0\rangle\langle B_1|y_B|B_1\rangle$

$$- 2\langle A_0|z_A|A_0\rangle\langle B_1|z_B|B_1\rangle\} \ . \tag{3.19}$$

We see that $E^{(1)}=0$ for this case since x,y,z have odd parity whereas the (nondegenerate) atomic states $|A_0\rangle$ and $|B_1\rangle$ have well defined parities.

As a result, the leading first-order correction (lowest order R^{-n} term) to the interatomic potential energies usually arises when the perturbation is a quadrupole-quadrupole interaction (i.e. when both atomic states of A and B are characterized by $J \geqslant 1$, or non-S states).

In view of the above statement (that there are no first-order energy contributions to atomic interactions when one of the atoms is in an S-state), let us examine the paradox posed by the Na(3s) and Na (3p) interactions which do possess first-order contributions. This particular combination of atoms exhibits this unique behavior for two reasons:

a) There exists an energy degeneracy in this homonuclear system composed of atoms in different electronic states. Therefore, the total energy of the Na_2 system remains unchanged when the state of excitation is interchanged between the sodium atoms. In other words, if we label one sodium atom A and the other B, then $E(A_s + B_p) = E(A_p + B_s)$.

b) The two atomic states are connected by an electric-dipole transition.
Consequently, the first-order energy corrections are of the dipole-dipole form, C_3/R^3. This will be shown below using degenerate perturbation theory.

The following heuristic argument helps us to visualize the first-order dipole-dipole interaction. When the two sodium atoms are near one another, they can exchange their state of excitation with the simultaneous absorption and emission of photons at the frequency of the $^2P \rightarrow {}^2S$ transition. (They are, in essence, exactly matched oscillators capable of resonantly driving each other). When the atoms interchange their excitation, the charge distribution at each atom oscillates between

the 3s and 3p states. The resulting transition dipole moments set up at each atom can interact with one another in the same fashion as two classical dipoles, with an R^{-3} energy dependence.

We can formally obtain a C_3/R^3 first-order correction using degenerate perturbation theory. For purposes of clarity, let us label one sodium atom A and the other B. The states of atoms A and B can be specified in zero-order (that is, in the absence of A-B interaction, where A and B have spherically symmetric potentials) by their orbital angular momentum L, and the projection of L on the AB internuclear axis, Λ. The six degenerate zero-order wave functions, denoted by $|A_L,A_\lambda\rangle|B_L,B_\lambda\rangle$, are

$$
\begin{array}{ll}
|A_s,0\rangle|B_p,1\rangle & |A_p,1\rangle|B_s,0\rangle \\
|A_s,0\rangle|B_p,0\rangle & |A_p,0\rangle|B_s,0\rangle \\
|A_s,0\rangle|B_p,-1\rangle & |A_p,-1\rangle|B_s,0\rangle \ .
\end{array}
\tag{3.20}
$$

The first-order energies and eigenfunctions can be obtained by diagonalizing the 6x6 Hamiltonian matrix that is formed in the basis of the above wave functions. Rather than proceeding with a brute force solution of the secular equation, $\det(H-\lambda\delta_{ij}) = 0$, we instead prefer to reduce this 6x6 matrix using the symmetry properties of the molecular system. The cylindrical symmetry of a diatomic molecule implies that $[L_z,H]=0$. Therefore, the matrix elements of the perturbation that are off-diagonal in Λ (where $\Lambda = \lambda_A + \lambda_B$) are zero. This immediately allows us to reduce the 6x6 matrix to a block-diagonal form, consisting of three 2x2 blocks, where each block has the same Λ:

$$H^{(1)} = \begin{array}{c|cccccc} & |01\rangle & |10\rangle & |00\rangle & |00\rangle & |0\text{-}1\rangle & |\text{-}10\rangle \\ \hline \langle 01| & 0 & * & & & & \\ \langle 10| & * & 0 & & & & \\ \langle 00| & & & 0 & * & & \\ \langle 00| & & & * & 0 & & \\ \langle 0\text{-}1| & & & & & 0 & * \\ \langle\text{-}10| & & & & & * & 0 \end{array}$$

(3.21)

Here, $|0\text{-}1\rangle$ is used to represent symbolically $|A_s,0\rangle|B_p,\text{-}1\rangle$, and likewise for the other wave functions. The asterisks denote nonzero matrix elements. The above matrix can be further reduced by using the g/u inversion symmetry of homonuclear diatomic molecules. Since $[i,H] = 0$, there exist eigenfunctions of H which are also simultaneous eigenfunctions of the g/u symmetry operator i. Use of this symmetry label completely diagonalizes the the perturbation matrix of Equation (3.21). The resulting first-order eigenfunctions, labelled as $\psi_{M_L},\pm$ (where the two subscripts refer to $\pm\Lambda$ and the symmetry of the linear combination) are listed below:

$$\psi^{(1)}_{1,+} = 1/\sqrt{2}\,(|01\rangle+|10\rangle) \qquad \psi^{(1)}_{1,-} = 1/\sqrt{2}\,(|01\rangle-|10\rangle)$$

$$\psi^{(1)}_{0,+} = 1/\sqrt{2}\,(|00\rangle+|00\rangle) \qquad \psi^{(1)}_{0,-} = 1/\sqrt{2}\,(|00\rangle-|00\rangle) \qquad (3.22)$$

$$\psi^{(1)}_{-1,+} = 1/\sqrt{2}\,(|0\text{-}1\rangle+|\text{-}10\rangle) \qquad \psi^{(1)}_{-1,-} = 1/\sqrt{2}\,(|0\text{-}1\rangle-|\text{-}10\rangle)\ .$$

Symmetric and antisymmetric linear combinations correspond to u and g symmetry, respectively. The first-order energies associated with the

above symmetry-adapted wave functions, for a dipole-dipole perturbation
(Equation (3.18)), are

$$E^{(1)} = \langle \psi^{(1)} | H_{dd} | \psi^{(1)} \rangle$$

$$\therefore \quad E_{1,+}^{(1)} = +C_3/R^3 \qquad E_{1,-}^{(1)} = -C_3/R^3$$

$$E_{0,+}^{(1)} = -2C_3/R^3 \qquad E_{0,-}^{(1)} = +2C_3/R^3 \qquad (3.23)$$

$$E_{-1,+}^{(1)} = +C_3/R^3 \qquad E_{-1,-}^{(1)} = -C_3 R^3$$

where $C_3 \equiv e^2 |\langle s|x|p_x \rangle|^2.$ \hfill (3.24)

We can label the molecular states corresponding to each of the above
eigenfunctions. The electronic states of homonuclear diatomic molecules
are denoted by

$$^{2S+1}\Lambda_{g,u}^{\pm}$$

where Λ is the projection of the electronic orbital angular momentum
along the internuclear axis,

$$\Lambda = |M_L|$$

Since the range of possible values of Λ is $|\lambda_A + \lambda_B|, \cdots, |\lambda_A - \lambda_B|$, two atoms
in S and P states can combine to give , $\Lambda = \Sigma$ or Π (M_L = 0 or ±1). $\Lambda > 0$
states are doubly degenerate. The left superscript, 2S+1, refers to the
multiplicity of the total spin, S. For two spin one-half atoms, S=0 or
1, singlets or triplets. The right superscript, + or -, is determined by
the sign of the molecular electronic wave function upon reflection in a

plane passing through both nuclei. Thus, a combination of like atoms in ^2S and ^2P states produces the singlet states, $\{^1\Sigma_g^+, \ ^1\Sigma_u^+, \ ^1\Pi_g, \ ^1\Pi_u\}$ and the triplet states $\{^3\Sigma_g^+, \ ^3\Sigma_u^+, \ ^3\Pi_g, \ ^3\Pi_u\}$.

Let us first consider the singlet states. There are a total of six such states; recall from Equation (3.22) that there are six first-order eigenfunctions. A molecular state assignment for each eigenfunction is very straightforward and is shown in Table 3.2. It is seen that these symmetry-adapted wave functions, having the appropriate symmetry labels for a diatomic molecule, diagonalize the perturbation Hamiltonian (Equation (3.21)) to yield:

$$
H^{(1)} = \begin{bmatrix}
\Pi_g^+ & & & & & \\
 & \Pi_u^+ & & & & \\
 & & \Sigma_g^+ & & & \\
 & & & \Sigma_u^+ & & \\
 & & & & \Pi_g^- & \\
 & & & & & \Pi_u^-
\end{bmatrix} . \tag{3.25}
$$

In the above matrix, Π^+ and Π^- refer to symmetric and antisymmetric combinations of the $M_L = +1$ and $M_L = -1$ states.

We noted earlier that the $(^2S+^2P)$ limit also produces triplet states. Since we are considering long-range atomic interactions, overlap and electron exchange effects are assumed to be negligible. As a result the singlet and triplet states within each of the four pairs $-(^1\Sigma_g^+, \ ^3\Sigma_u^+)$, $(^1\Pi_g, \ ^3\Pi_u)$, $(^1\Pi_u, \ ^3\Pi_g)$, $(^1\Sigma_u^+, \ ^3\Sigma_g^+)$ - have identical forms for the long-range potentials. These are illustrated in Figure 3.2.

Let us momentarily digress in order to show that this specific

Table 3.2   First-order energies and wave functions for the Na (3s) +

Na (3p) atomic limit. $|01\rangle + |10\rangle$ denotes $|A_sB_{p_{m=1}} + |A_{p_{m=1}}B_s\rangle$.

The last column is a schematic representation of the

orientation of <u>transition</u> <u>dipole</u> <u>moments</u> when the atoms

combine to form each molecular state.

State	Symmetry-Adapted Wave Function	Energy	Transition Dipoles	
$1\Sigma_g^+$	$1/\sqrt{2}\,(\|00\rangle - \|00\rangle)$	$+2C_3/R^3$	→	←
$1\Pi_u$	$1/\sqrt{2}\,(\|01\rangle + \|10\rangle)$ $1/\sqrt{2}\,(\|0\text{-}1\rangle + \|\text{-}10\rangle)$	$+C_3/R^3$	↑	↑
$1\Pi_g$	$1/\sqrt{2}\,(\|01\rangle - \|10\rangle)$ $1/\sqrt{2}\,(\|0\text{-}1\rangle - \|\text{-}10\rangle)$	$-C_3/R^3$	↑	↓
$1\Sigma_u^+$	$1/\sqrt{2}\,(\|00\rangle + \|00\rangle)$	$-2C_3/R^3$	→	→

Figure 3.2 The R^{-3} behavior of the molecular potentials of Na_2 near the
Na 3s (^2S) + Na 3p (^2P) asymptote. The short dashed lines
refer to the ($^2S_{1/2}$ + $^2P_{3/2}$) and ($^2S_{1/2}$ + $^2P_{1/2}$) limits; the
long dashed line refers to the degeneracy-weighted average of
these two limits. (From Ref. 12).
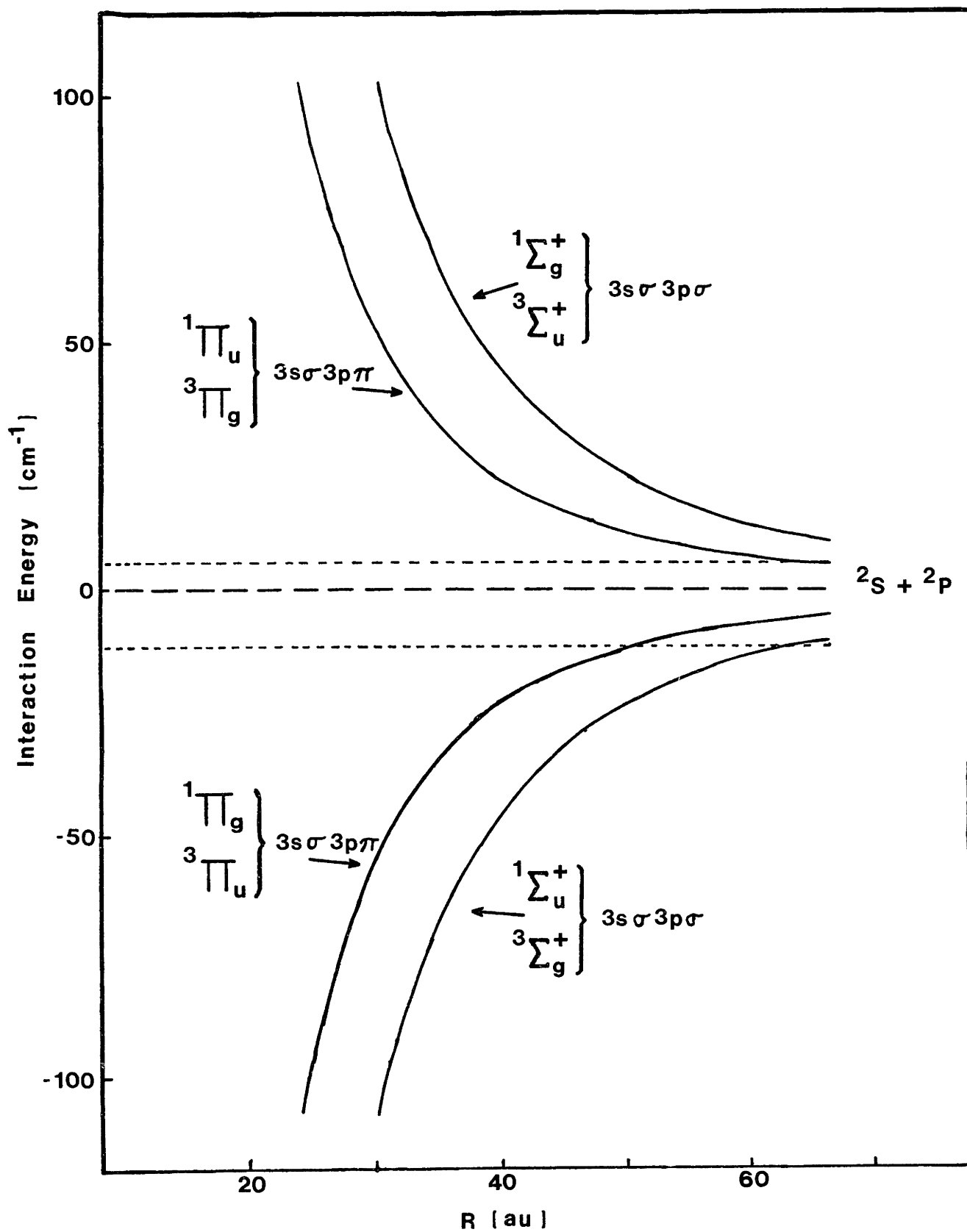
pairing of singlets and triplets at long range is reasonable. It can be explained quite simply as follows. The zero-order wavefunctions of Equation (3.20) are not properly symmetrized to account for the indistinguishability of identical electrons. (The results that followed are nevertheless still valid). To illustrate the identical behavior of certain singlet and triplet states, at large R, let us now symmetrize $\psi° = A_s(1)B_p(2)$ with respect to electron exchange. Applying $(1 \pm P_{12})/\sqrt{2}$ to $\psi°$, where P_{12} is the permutation operator of electrons 1 and 2, we get:

$$(2)^{-1/2} (A_s(1)B_p(2) \pm A_s(2)B_p(1)),$$

where the symmetric combination corresponds to a singlet state and the antisymmetric to triplet states. Now applying $(1 \pm i)/\sqrt{2}$ to the above wavefunction, where i is the inversion operator, we get the final result:

$$(2)^{-1} [A_s(1)B_p(2) \pm A_s(2)B_p(1)] \mp [B_s(1)A_p(2) \pm B_s(2)A_p(1)],$$
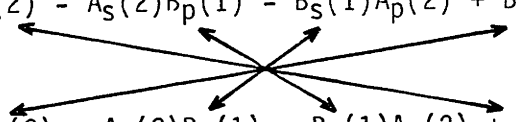
where the antisymmetric combination (outside the square brackets) corresponds to a gerade state and the symmetric combination to an ungerade state. Therefore, the four combinations for a given Λ value are

$$
\begin{aligned}
[\; + \;] - [\; + \;] &\equiv {}^1\Lambda_g \\
[\; + \;] + [\; + \;] &\equiv {}^1\Lambda_u \\
[\; - \;] - [\; - \;] &\equiv {}^3\Lambda_g \qquad (3.26) \\
[\; - \;] + [\; - \;] &\equiv {}^3\Lambda_u \; .
\end{aligned}
$$

We wish to show that in the long range limit, the following is true:

$$\langle {}^1\Lambda_g | H_{dd} | {}^1\Lambda_g \rangle = \langle {}^3\Lambda_u | H_{dd} | {}^3\Lambda_u \rangle \ .$$

Consider the ${}^3\Sigma_g^+$ state. Since $\Lambda = 0$, the non-zero part of the dipole-dipole perturbation matrix element (Equation (3.18)) for this state involves the $-2\mu_{A_z}\mu_{B_z}/R^3$ term. Since μ_A and μ_B do not act on the spin coordinates, only the four matrix elements indicated below are nonzero:

$$\frac{-2}{R^3}\langle A_s(1)B_p(2) - A_s(2)B_p(1) - B_s(1)A_p(2) + B_s(2)A_p(1)| \ \mu_A\mu_B$$

$$|A_s(1)B_p(2) - A_s(2)B_p(1) - B_s(1)A_p(2) + B_s(2)A_p(1)\rangle \ .$$

Thus, the first-order energy correction for the ${}^3\Sigma_g^+$ state is

$$E^{(1)} = \frac{-2}{R^3} \ |\langle A_s | \mu_A | A_p \rangle|^2 \ ,$$

since A and B are, in fact, like atoms. By inspection of Equation (3.26), we can see that the ${}^1\Sigma_u^+$ state also has this correction energy (i.e. $E^{(1)}$ is the same for both ${}^3\Sigma_g^+$ and ${}^1\Sigma_u^+$).

In summary, we see that the $Na({}^2S) + Na({}^2P)$ atomic limit has the unique feature of giving rise to one first-order correction, the C_3/R^3 term. From Equation (3.24), the C_3 coefficient was seen to be proportional to the square of the transition dipole moment for the Na $^2P \leftarrow {}^2S$ D-line transition. With the definition of the oscillator strength, f_{n0}, for the transition $|\phi_n\rangle \leftarrow |\phi_0\rangle$,

$$f_{n0} = \frac{2m\omega_{n0}|\langle \phi_n | \mu | \phi_0 \rangle|^2}{\hbar} \qquad , \qquad (3.27)$$

we see that the C_3 coefficient is proportional to the oscillator strength of the D-lines. Thus, a determination of the C_3/R^3 contribution to the long range molecular potential (for any of the above-mentioned molecular states) allows one to rigorously determine an atomic property of fundamental importance, the 3p←3s oscillator strength.

B. Second Order Corrections

For a more accurate description of long range potentials, one must also account for energy corrections arising from second-order terms in the multipolar perturbation. Consider first the dipole-dipole perturbation on the general AB system composed of two unlike atoms A and B in, respectively, the s and p states. The second order correction is:

$$E^{(2)} = \sum_{\substack{i \\ i \neq s}} \sum_{\substack{j \\ j \neq p}} \frac{\langle A_s B_p | H_{dd} | A_i B_j \rangle \langle A_i B_j | H_{dd} | A_s B_p \rangle}{(E_{A_s} - E_{A_i}) + (E_{B_p} - E_{B_j})} \tag{3.28}$$

$$= \frac{1}{R^6} \sum_{i,j}' \frac{|\langle A_s B_p | \mu_{A_x} \mu_{B_x} + \mu_{A_y} \mu_{B_y} - 2\mu_{B_z} \mu_{B_z} | A_i B_j \rangle|^2}{(E_{A_s} - E_{A_i}) + (E_{B_p} - E_{B_j})}$$

where the indices of the primed-summation i,j refer to all zero-order electronic states of A and B except $|A_s\rangle|B_p\rangle$. Since the sum runs over all atomic states of even and odd parity, the second-order energy correction is nonzero. Similarly, perturbations corresponding to dipole-quadrupole, quadrupole-quadrupole, dipole-octupole (and so on) interactions between atoms A and B also make second-order energy corrections and form a series with even powers of R, i.e.,

$$E^{(2)} = C_6/R^6 + C_8/R^8 + C_{10}/R^{10} + \cdots \quad . \tag{3.29}$$

The terms of Equation (3.29) are often referred to as dispersion contributions. The dispersion form of the second-order corrections becomes evident with the following approximation to Equation (3.28). If the various energy differences in the sum of Equation (3.28) are replaced by a mean energy difference (Unsöld's approximation[39]),

$$\sum_{i}{}'\sum_{j}{}' \frac{1}{(E_{A_s}-E_{A_i})+(E_{B_p}-E_{B_j})} \approx \frac{1}{(\overline{E_{A_s}-E_{A_i}})+(\overline{E_{B_p}-E_{B_j}})} \equiv \frac{1}{\overline{E}} \,, \qquad (3.30)$$

and if we use the closure relation in Equation (3.28) we get:

$$E^{(2)} = \frac{1}{\overline{E}} \{ \sum_{ij} \langle A_s B_p|W|ij\rangle\langle ij|W|A_s B_p\rangle - |\langle A_s B_p|W|A_s B_p\rangle|^2 \}$$

$$= \frac{1}{\overline{E}}[\langle W^2\rangle - \langle W\rangle^2] \quad . \qquad (3.31)$$

Notice that the above equation has the form of the variance, or mean square deviations, of the energy; hence the name attributed to second-order energy corrections, "dispersion energies".

In order to gain insight into the C_6 (and other second-order) coefficients, let us note that Equation (3.28) is very similar to the product of the static dipole polarizabilities of atoms A and B:

$$\alpha_{A_s}\alpha_{B_p} = 4 \sum_{ij}{}' \frac{|\langle A_s|\mu_A|A_i\rangle\langle B_p|\mu_B|B_j\rangle|^2}{(E_{A_s}-E_{A_i})\,(E_{B_p}-E_{B_j})}$$

If Equation (3.30) is substituted into Equation (3.28), then one can directly relate C_6 to the polarizabilities (London's formula[38]):

$$C_6 \simeq \alpha_A\alpha_B\overline{\omega}/4 \qquad (3.32)$$

where $\bar{\omega} = \overline{\Delta E_A} \overline{\Delta E_B}/(\overline{\Delta E_A} + \overline{\Delta E_B})$. That the molecular C_6 coefficient is proportional to the dipole polarizabilities of the atoms is a reasonable outcome. The physical basis of the second-order corrections lies in the mutual distortion of the atomic wave functions, when each atom is in the vicinity of the other; a measure of the ease of distortion is given by the polarizability. By similar arguments, the C_8 coefficient is proportional to the dipole and quadrupole polarizabilities of both atoms.

We would expect the C_6 term to be different for the Σ and Π molecular states of AB, with a larger C_6 for the Σ st.·· than the Π state. This difference has its origin in the anisotropic polarizability of the p state and is considered below. It can be seen from Figure 3.3 that C_6^Σ samples polarizability of the B_{p_z} orbital and $C_6^{\Pi+}$ (or $C_6^{\Pi-}$) samples the polarizability of the B_{p_x} (or B_{p_y}) orbital. Of course, both C_6 coefficients sample the A_S polarizability but because of the spherical symmetry of the s state, $\alpha(A_S)$ does not affect the C_6 anisotropy. We can show the degree of C_6 anisotropy by expressing $\alpha(B_{p_x})$ and $\alpha(B_{p_z})$ in terms of the two unique components of the p state polarizability, $\alpha_\parallel$ and $\alpha_\perp$. ($\alpha_\parallel$ and $\alpha_\perp$ are defined as the polarizabilities produced by an electric field applied parallel and perpendicular to the orientation of the p orbital). Rewriting W_{dd} of Equation (3.17) as

$$H_{dd} = \vec{\mu}_A \cdot \vec{\mu}_B : (1 - 3\hat{R}\hat{R})/R^3,$$

We get for the second-order energy:

$$E^{(2)} = \frac{1}{R^6} \sum_{ij}{}' \frac{|\langle A_S|\mu_A|A_i\rangle|^2 |\langle B_p|\mu_B|B_j\rangle|^2 : (1-3\hat{R}\hat{R})^2}{(E_{A_S}-E_{A_i})+(E_{B_p}-E_{B_j})}$$

Using Unsöld's approximation as before and the definition of the

polarizability, we get for the C_6 coefficient:

$$C_6 \simeq \alpha_A \alpha_B : (1-3\hat{R}\hat{R})^2$$

$$\simeq \alpha_A \begin{bmatrix} \alpha_{xx} & & \\ & \alpha_{yy} & \\ & & \alpha_{zz} \end{bmatrix}_B \begin{bmatrix} 1 & & \\ & 1 & \\ & & 4 \end{bmatrix}$$

where $\hat{R}$ lies along the z axis of the molecule. For a Π-state, $\alpha_{yy}\equiv\alpha_\parallel$ and $\alpha_{xx}=\alpha_{zz}\equiv\alpha_\perp$; for a Σ state, $\alpha_{zz}\equiv\alpha_\parallel$ and $\alpha_{xx}=\alpha_{yy}\equiv\alpha_\perp$. Therefore, from the above equation, we get:

$$C_6^\Sigma \sim \alpha_A(4\alpha_\parallel+2\alpha_\perp)_B \qquad (3.33)$$

$$C_6^{\Pi-} = C_6^{\Pi+} \sim \alpha_A(\alpha_\parallel+5\alpha_\perp)_B$$

Since $\alpha_\parallel > 2\alpha_\perp$, we see that $C_6^\Sigma > C_6^\Pi$.

Equation (3.33) can be obtained by an intuitive line of reasoning as well. Figure (3.3) shows that the electric field that polarizes the p orbital of atom B originates from the "instantaneous dipoles" of atom A. Momentary fluctuations in the charge distribution of atom A cause instantaneous dipoles (in atom A) in the x, y and z directions. Notice that a dipole (of atom A) along the z direction is able to cause fourfold greater polarization (of atom B) than a dipole in the x or y direction $[\alpha_{zz}\sim|<-2\mu_{A_z}\mu_{B_z}>|^2$ whereas $\alpha_{xx}\sim|<\mu_{A_x}\mu_{B_x}>|^2]$. Since the x, y and z dipoles of atom A (in the spherically symmetric s state) occur with equal probability, one simply adds the contributions made by each of these to determine the total polarization of atom B. Thus, we obtain Equations (3.33).

Two significant conclusions can be drawn from Equation (3.33). Firstly, experimentally determined C_6 coefficients for one Σ and one Π

Figure 3.3 Different polarizabilities of the B_p orbital in Σ and Π
molecular states of the molecule AB.

Σ

$4\alpha_{\parallel}$

$\alpha_{\perp}$

A

$\alpha_{\perp}$

B

z

$\Rightarrow$

$\alpha_{Bp_z} = 4\alpha_{\parallel} + 2\alpha_{\perp}$

Π

$4\alpha_{\perp}$

$\alpha_{\parallel}$

$\alpha_{\perp}$

x

z

$\Rightarrow$

$\alpha_{Bp_x} = \alpha_{\parallel} + 5\alpha_{\perp}$
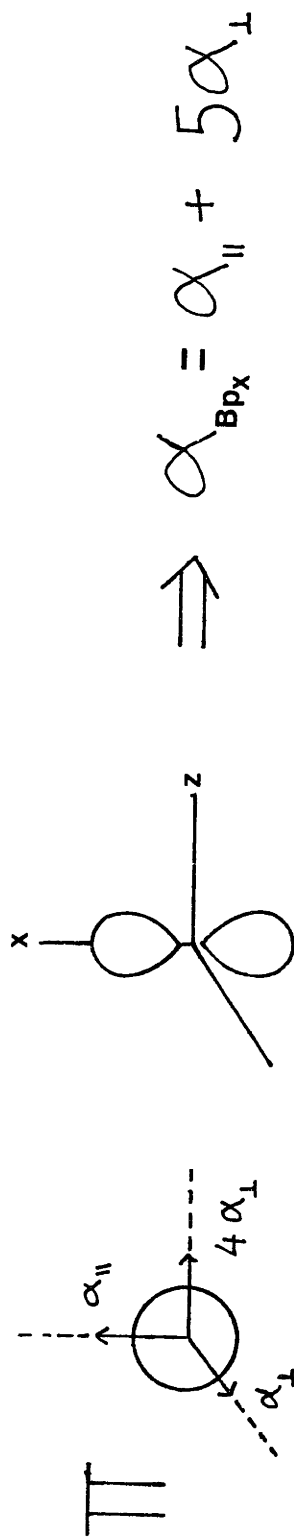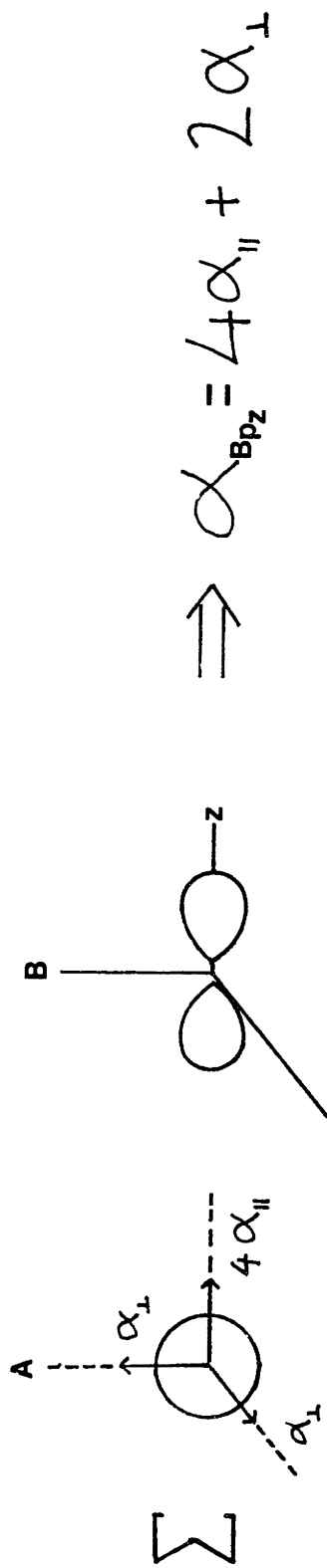
molecular state (correlating to the same 3s+3p atomic limit) can be combined to determine $\alpha_\parallel$ and $\alpha_\perp$ for the 3p state, thus completely characterizing the p state polarizability. (This is of course assuming knowledge of an α for the s state.) Secondly, knowledge of the Na 3p state polarizability allows one to determine C_6 coefficients for those molecular states of Na_2 that dissociate into two Na(3p) atoms. For example,

$$C_6(\Sigma) \simeq 2\alpha_\perp^2 + 4\alpha_\parallel^2$$

$$(\Pi) \simeq \alpha_\perp^2 + 5\alpha_\parallel\alpha_\perp$$

$$(\Delta) \simeq 5\alpha_\perp^2 + \alpha_\parallel^2$$

In addition, the 3p state polarizability provides information relevant to the C_6 terms of other Na_2 molecular states, dissociating to Na(3p) + Na (other) limits as well as heteronuclear diatomic molecular states containing Na(3p).

It should be emphasized that the above-mentioned relationships between the molecular C_6 coefficient and the atomic dipole polarizabilities are based upon Unsöld's approximation. Errors associated with this approximation should be insignificant when determining C_6 anisotropies. In addition, since there appear to be reliable methods for determining $\overline{\omega}$ in Equation (3.32) based on oscillator strength sum rules;[40] one should also be able to make reasonable estimates of C_6 coefficients from polarizabilities, and vice-versa.

We conclude this section by determining the anisotropy of the C_6 coefficient for the Σ and Π molecular states of Na_2, in a different manner from that shown above. This exercise is useful because it allows the C_6 term for both states to be expressed in terms of a common matrix element (Equation (3.37)). From Equation (3.31) we see that the

orientation dependence of C_6 is determined primarily by $\langle H_{dd}^2 \rangle$. The resonance term, $\langle H_{dd} \rangle^2$, is relatively negligible. The anisotropy of $\langle H_{dd}^2 \rangle$ depends upon the angular factors of only the following matrix elements:

$$\langle H_{dd}^2 \rangle = \frac{e^4}{R^6} \{ \langle x_A^2 \rangle \langle x_B \rangle^2 + \langle y_A^2 \rangle \langle y_B^2 \rangle + 4 \langle z_A^2 \rangle \langle z_B^2 \rangle$$

$$+ 2 \langle x_A y_A \rangle \langle x_B y_B \rangle - 4 \langle x_A z_A \rangle \langle x_B z_B \rangle - 4 \langle y_A z_A \rangle \langle y_B z_B \rangle \} \qquad (3.34)$$

where $\langle x_A^2 \rangle$ and $\langle x_B^2 \rangle$ denote the expectation value of x^2 for atom A in the s state and atom B in the p state. Using the Wigner-Eckart theorem we find for atom B:

$$\left. \begin{aligned} \langle x^2 \rangle = \langle y^2 \rangle &= 2/5 \langle r^2 \rangle \\ \langle z^2 \rangle &= 1/5 \langle r^2 \rangle \end{aligned} \right\} \lambda = \pm 1 \qquad (3.35)$$

and

$$\left. \begin{aligned} \langle x^2 \rangle = \langle y^2 \rangle &= 1/5 \langle r^2 \rangle \\ \langle z^2 \rangle &= 3/5 \langle r^2 \rangle \end{aligned} \right\} \lambda = 0$$

where $\langle r^2 \rangle$ is a radial integral of r^2 for the Na 3p state. For atom A in the spherically symmetric s state,

$$\langle x^2 \rangle = \langle y^2 \rangle = \langle z^2 \rangle = 1/3 \langle r^2 \rangle$$

and
$$\langle xy \rangle = \langle yz \rangle = \langle xz \rangle = 0 \qquad (3.36)$$

Combining Equations (3.34)-(3.36), we get a measure of the anisotropy of $\langle H_d^2 \rangle$,

$$\langle H_{dd}^2 \rangle = \frac{e^4}{15 R^6} \langle r^2 \rangle_A \langle r^2 \rangle_B \times \left\{ \begin{aligned} 8 &\quad \text{for } M_L = \pm 1 \ (\Pi) \\ 14 &\quad \text{for } M_L = 0 \ (\Sigma) \end{aligned} \right. \qquad (3.37)$$

We see that the C_6 coefficient for Σ states is a factor of 1.75 larger than that for Π states. This approximate ratio is in very good agreement (to within 5%) with that ratio determined from Bukta and Meath's[41] accurate values of C_6 for the H(1s) + H(2p) atomic limit. These and other C_n coefficients for the molecular states of H_2 dissociating to this limit are reproduced in Table 3.3. Table 3.4 shows various theoretical estimates of the C_n coefficients for molecular states of Na_2 dissociating to the Na(3s) + Na(3p) limit. It is seen that the C_6 anisotropy of 1.55 among these molecular states agrees poorly with the factor of 1.75 predicted by Equation (3.37).

C. Third-Order Corrections

It should be noted that the resonance degeneracy of the Na(3s) + Na(3p) atomic limit leads to a third-order energy correction involving an R^{-1} term of relatively low order; the H_{dd} perturbation leads to a C_9/R^9 term. Therefore, the long-range interaction potential takes the form

$$E(R) = E^{(0)} + \frac{C_3^{(1)}}{R^3} + \frac{C_6^{(2)}}{R^6} + \frac{C_8^{(2)}}{R^8} + \frac{C_9^{(3)}}{R^9} + \frac{C_{10}^{(2)}}{R^{10}}$$

where the superscript on each C_n coefficient indicates the order of the perturbation giving rise to that term. The R^{-9}, R^{-10}, and higher terms generally make negligible contributions to the total energy of the system at large R. Therefore, the potentials for the $A^1\Sigma_u^+$ and $B^1\Pi_u$ states considered in this thesis are represented by terms up to and including R^{-8}, in the above R^{-1} expansion.

Table 3.3 Calculated values of the C_n coefficients (in atomic units) in the R^{-1} expansion for the interaction energy between ground and first excited state hydrogen atoms. From Bukta and Meath.[41]

State	C_3	C_6	C_8	C_9	C_{10}
$^1\Sigma_g^+$ ($1s$–$2p$) $^3\Sigma_u^+$	$+1.1098579146$	-174.16590097	-31724.678808	-594.176339	-3807934.0723
$^1\Sigma_u^+$ ($1s$–$2p$) $^3\Sigma_g^+$	-1.1098579146	-174.16590097	-26378.305423	$+594.176339$	-3413054.7620
$^1\Pi_g$ ($1s$–$2p$) $^3\Pi_u$	-0.5549289573	-94.457429859	-10576.817484	$+136.428052$	-47942.765643
$^1\Pi_u$ ($1s$–$2p$) $^3\Pi_g$	0.5549289573	-94.457429859	-1623.4758167	-136.428052	-82988.475938

Table 3.4 Calculated values of the C_n coefficients (in atomic units) for molecular states of Na_2 correlating with Na(3s) + Na(3p) atomic limit: First row from Vigne-Maeder,[42] second row from Bussery[12] and third row from Konowalow and Rosenkrantz.[43]

State	C_3	C_6	C_8	C_9	C_{10}
$^1\Sigma_g^+$ $^3\Sigma_u^+$	+12.51 +12.95	-4164 -4144	-2.078(6) -1.128	+2.830(5)	-3.043(8)
$^1\Sigma_u^+$ $^3\Sigma_g^+$	-12.51 -12.95 -13.3	-4164 -4144 -5800	-6.775(5) -1.036	-2.830(5)	-8.771(7)
$^1\Pi_g$ $^3\Pi_u$	-6.255 -6.48 -6.85	-2686 -2669 -2900	-8.229(4) -3.582	-5.978(4)	-2.402(6)
$^1\Pi_u$ $^3\Pi_g$	+6.255 +6.48 +6.86	-2686 -2669 -2100	-2.100(5) +4.438(4)	+5.978(4)	-2.045(7)

CHAPTER FOUR

THE Na_2 $B^1\Pi_u$ STATE

4.1 <u>Introduction</u>

The long range potential of the Na_2 B $^1\Pi_u$ state has stimulated much interest because of its characteristic barrier to dissociation. This barrier is thought to arise from the combined effect of two competing forces. At large internuclear separations when Na(3s) and Na(3p) atoms combine to form the B $^1\Pi_u$ state, they must be oriented so that the 3p←3s transition dipole moments set up in each atom are parallel to one another and perpendicular to the axis of approach. The interaction of these transition dipole moments gives rise to a repulsive C_3/R^3 interaction energy which dominates the character of the potential at long range. As the inter-atomic distance is reduced and the charge distributions of the atoms overlap, attractive electron-exchange interactions begin to contribute to the potential energy. The resultant of these two inter-actions produces a barrier (at about 7Å). Because the barrier rises several hundred wave numbers above the dissociation limit, it is able to support several quasi-bound vibrational levels. The lowest three quasi-bound levels, v=27-29, have been previously observed by Kusch and Hessel[14].

A characteristic property of these quasibound levels is their ability to tunnel through the barrier. We hoped to study the variation of tunneling lifetimes with energy for all of the quasibound levels and invert this information to yield the location of the barrier maximum and the shape of the barrier's outer wall. The energy levels themselves would, in addition, extend our knowledge of the potential well, with the inner wall of the potential barrier (outer wall of the potential well) being of greatest interest.

Figure 4.1 shows the best estimate of the B state barrier prior to this work.[44] It depicts the predicted height of ~410 cm^{-1} relative to

Figure 4.1 An estimate of the B state potential barrier, obtained by merging the known RKR potential[14] (for v=0-29) for R<10.7 bohr, with an <u>ab initio</u> long-range potential[43], R>15 bohr. Also shown in short dashes is the potential barrier predicted by Konowalow and Rosenkrantz[43]. This figure is provided by Stwalley[44].

114

Na$_2$ B$^1\Pi_u$
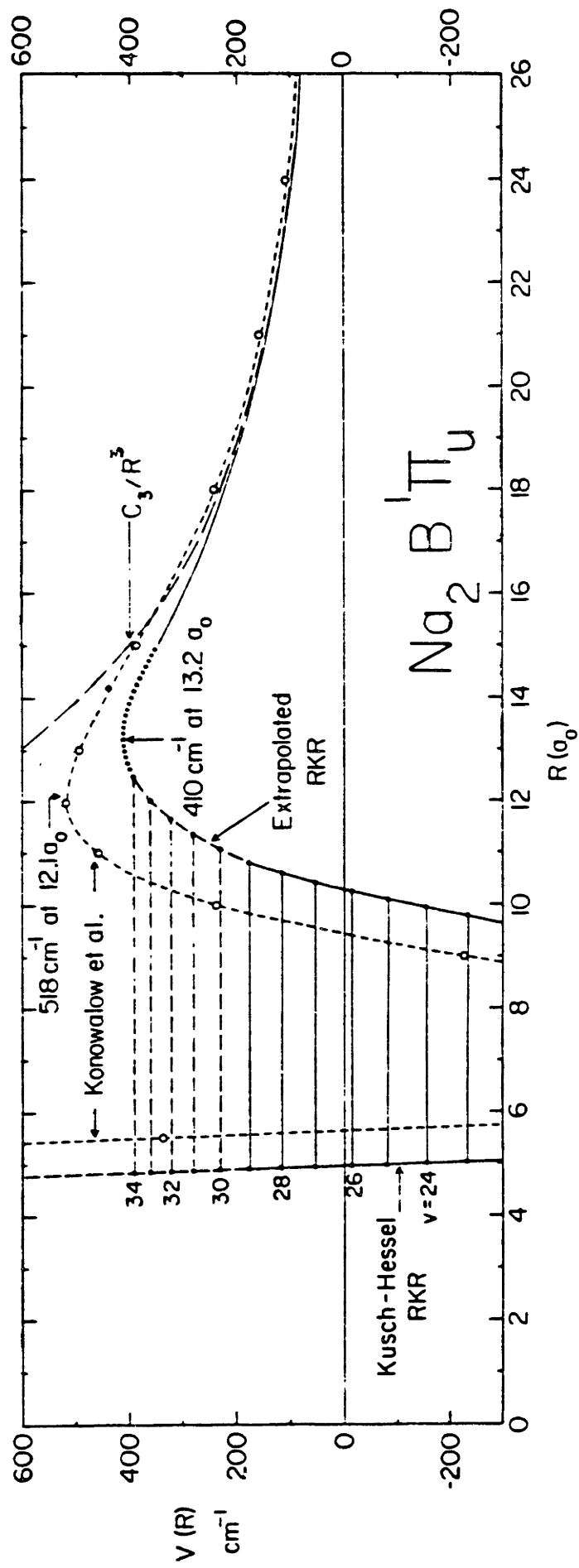
the Na (3s) + Na (3p) dissociation limit, and is expected to support eight quasibound levels, v=27-34.

4.2 Presentation of Data

$\underline{\text{All}}$ quasibound (v'=27-33) and the last few bound (v'=24-26) vibrational levels of the B state were observed using the technique of Modulated Gain Spectroscopy. The following three excitation schemes were used to access these levels (see Figure 2.1):

$$A^1\Sigma_u^+(v'=26,J') \overset{\text{PUMP}}{\leftarrow} X^1\Sigma_g^+(v''=4,J'')$$

(i)   OPL ↓

$$X^1\Sigma_g^+(v''=39,J'') \underset{\text{PROBE}}{\rightarrow} B^1\Pi_u(v'=24-27,J')$$

$$A^1\Sigma_u^+(v'=30,J') \overset{\text{PUMP}}{\leftarrow} X^1\Sigma_g^+(v''=5,J'')$$

(ii)   OPL ↓   (4.1)

$$X^1\Sigma_g^+(v''=44,J'') \underset{\text{PROBE}}{\rightarrow} B^1\Pi_u(v'=27-33,J')$$

$$A^1\Sigma_u^+(v'=34,J') \overset{\text{PUMP}}{\leftarrow} X^1\Sigma_g^+(v''=7,J'')$$

(iii)   OPL ↓

$$X^1\Sigma_g^+(v''=50,J'') \underset{\text{PROBE}}{\rightarrow} B^1\Pi_u(v'=33,J')$$
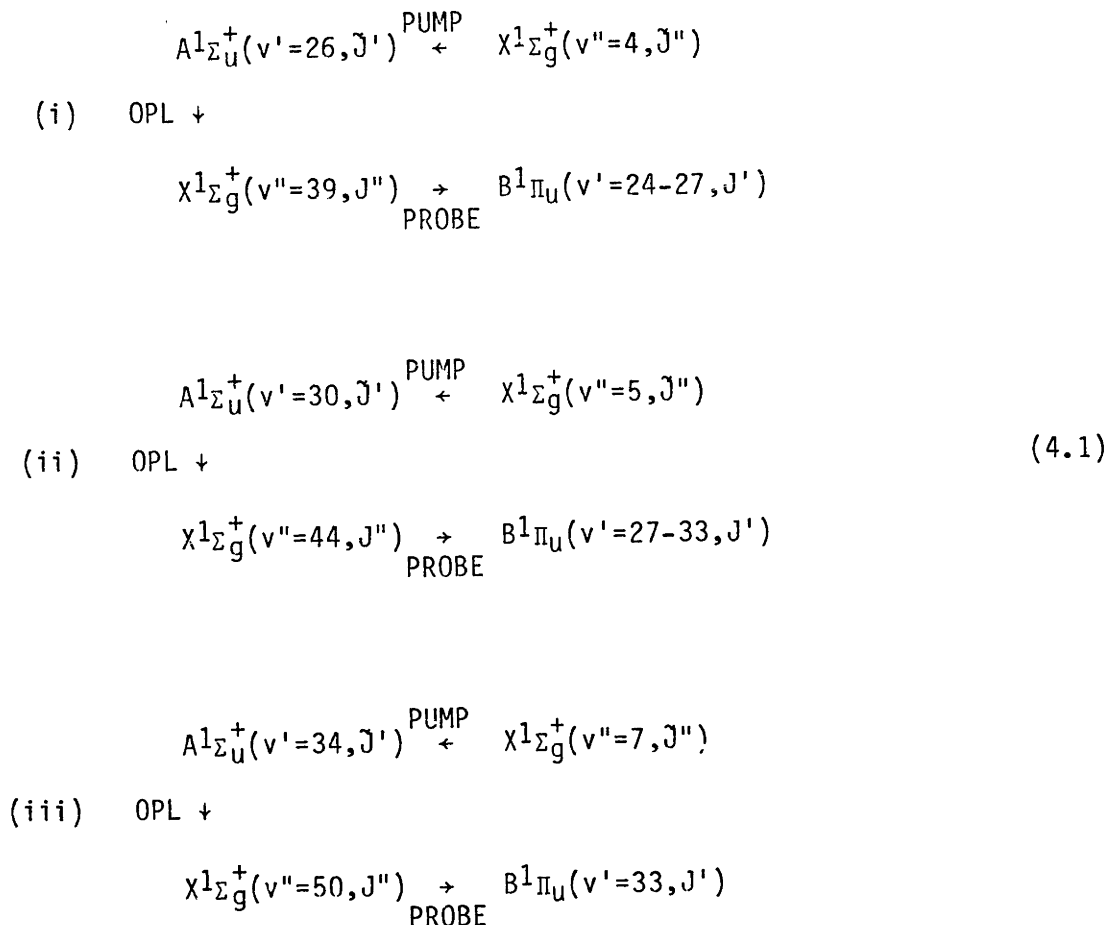
In the above equations, J'' denotes the thermally-populated rotational level of the X $^1\Sigma_g^+$ state which is the lower level of the PUMP laser excited transition; J', J'' and J' are determined by the rotational selection rules for the PUMP ($\Sigma\leftarrow\Sigma$), OPL ($\Sigma\rightarrow\Sigma$), and PROBE ($\Pi\leftarrow\Sigma$)

transitions ($\Delta J=\pm 1$ for $\Delta\Lambda=0$, and $\Delta J=0,\pm 1$ when $\Delta\Lambda\neq 0$). The different excitation schemes were chosen so as to optimize the Franck-Condon factors for the B←X PROBE transitions.

While a vibrational study of the B state is quite straightforward (by utilizing a series of schemes like (i)-(iii)), it should be pointed out that a rotational study, using a triple resonance excitation scheme, is not altogether trivial and requires further consideration. For a given J" that is prepared as the lower level of the OPL transition, only three rotational levels of the B state are accessible by the PROBE ($\Delta J=0,\pm 1$). Excitation into other levels of the $B^1\Pi_u$ state requires preparation of a different lower rotational level of the OPL. This, in turn, requires excitation into yet another rotational level of the A state by the PUMP. As a result, different preparative schemes are necessary (different PUMP-OPL transitions) in order to access each new set of three rotational levels ($\Delta J=0,\pm 1$) of the B state.

All measured PROBE frequencies to the B state levels are accurate to 0.006 cm^{-1}. This error is set by the calibration method used to determine the frequency of the PROBE laser; a simultaneously recorded excitation spectrum of I_2 is compared with lines in the I_2 atlas of Gerstenkorn and Luc,[22] which are reported with ± 0.003 cm^{-1} accuracy. The error associated with the absolute energies of the observed levels (relative to the minimum of the ground state) is not, however, uniformly 0.006 cm^{-1}. The accuracy is somewhat poorer (~0.012 cm^{-1}) for v'=33, J'=15-17 levels because these levels accessed with the third excitation scheme (iii), had to be calibrated against the J'=14 term value which was obtained via schemes (ii) and (iii). This was necessary because the v"=50

ground state energy is not determined sufficiently accurately when extrapolated from the molecular constants of Kusch and Hessel. The measured vibration-rotation term values are listed in Table 4.1.

The tunneling lifetimes of the quasibound levels were determined from the MGS linewidths. Pressure and power broadening of the PROBE transitions (~150 MHz) and some residual inhomogeneous broadening (~200 MHz) together combine to place a ~350 MHz lower bound on detectable tunneling rates. This is illustrated by Figure 4.2. MGS linewidths greater than 350 MHz were observed only for the rotational levels of the last quasibound vibrational level, v=33. The lineshape fitting procedure used and the resulting tunneling lifetimes for the J=3-17 levels of v=33 are discussed in Section four.

4.3 Analysis of Energy Levels

A. Padé Representation

In order to fit the observed term values to within their experimental uncertainties, a rational fraction representation was employed, with the near dissociation variable (v_D-v) as the expansion parameter[46]. v_D refers to the vibrational index (generally noninteger) at the dissociation limit; however, in the case of a barrier to dissociation, v_D refers to the vibrational index at the barrier maximum. The overall energy level expression is

$$E(v,J) = G(v) + B(v)[J(J+1)-1] + D(v)[J(J+1)-1]^2, \qquad (4.2)$$

since for a $^1\Pi$ state, $\Omega^2=1$. The G(v) part is expressed by a ratio of polynomials while the B(v) and D(v) parts are expressed by the exponential of a simple polynomial:

$$G(v) = E^\dagger - (v_D-v)^m [L/N] \qquad (4.3)$$

TABLE 4.1 Observed and calculated energy levels from the fitted parameters of Table 4.2. All energies are in cm^{-1}. $\sigma = 0.005\ cm^{-1}$

v	J	E_{obs}	$E_{obs}-E_{calc}$	v	J	E_{obs}	$E_{obs}-E_{calc}$
24	10	22844.899	-0.002	31	4	23271.912	-0.002
24	11	22846.948	0.000	31	5	23272.630	-0.002
24	12	22849.179	-0.002	31	6	23273.494	-0.001
				31	7	23274.497	-0.003
25	10	22918.086	0.004	31	8	23275.651	0.002
25	11	22920.082	0.004	31	9	23276.950	0.008
25	12	22922.258	0.003	31	10	23278.380	0.004
				31	11	23279.956	0.001
26	10	22987.983	0.000	31	12	23281.666	-0.009
26	11	22989.927	0.001				
26	12	22992.041	-0.002	32	4	23315.191	-0.005
				32	5	23315.858	-0.004
27	10	23054.372	-0.008	32	6	23316.655	-0.003
27	11	23056.258	-0.006	32	7	23317.583	-0.005
27	12	23058.316	-0.002	32	8	23318.653	0.002
				32	9	23319.852	0.009
28	10	23117.008	0.004	32	10	23321.177	0.009
28	11	23118.827	0.002	32	11	23322.633	0.008
28	12	23120.816	0.004	32	12	23324.215	0.003
				32	13	23325.925	-0.004
29	4	23168.354	-0.004	32	14	23327.766	-0.008
29	5	23169.151	-0.002				
29	6	23170.104	-0.005	33	3	23350.188	0.004
29	7	23171.222	-0.003	33	4	23350.653	0.002
29	8	23172.501	0.003	33	5	23351.244	0.008
29	9	23173.941	0.009	33	7	23352.742	-0.006
29	10	23175.532	0.008	33	8	23353.668	-0.009
29	11	23177.282	0.007	33	9	23354.711	-0.005
29	12	23179.188	0.002	33	10	23355.867	-0.001
29	13	23181.251	-0.004	33	11	23357.130	0.002
29	14	23183.476	-0.005	33	12	23358.501	0.003
				33	13	23359.976	0.002
30	10	23229.514	0.002	33	14	23361.555	0.001
30	11	23231.184	0.000	33	15	23363.235	-0.004
30	12	23233.003	-0.006	33	16	23365.026	0.003
				33	17	23366.905	-0.002

Figure 4.2 Simulation of the expected line broadening, above the 350 MHz

lower limit, due to tunneling through the barrier.

ABSORPTION

ENERGY OF
B STATE
LEVELS

PROBE
LASER
FREQUENCY

350 MHz
$\tau_{eff} \sim 0.45$ nsec

$\Delta \nu$ (MHz)

400

300

200

100

E

← LOWER BOUND ←

← velocity spread

← pressure broadening
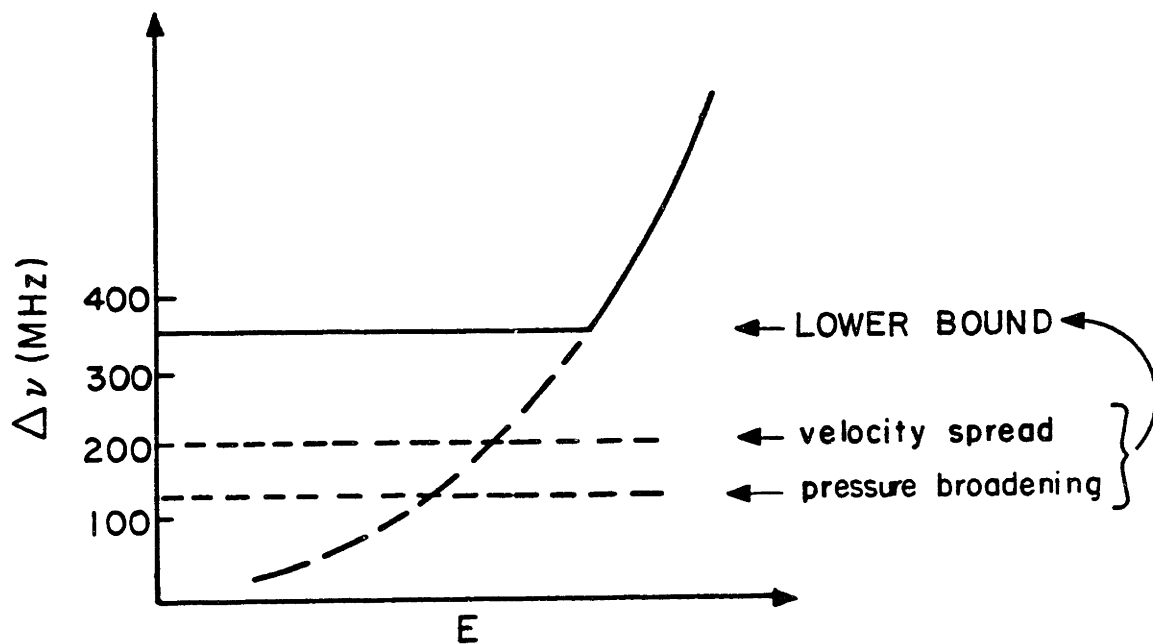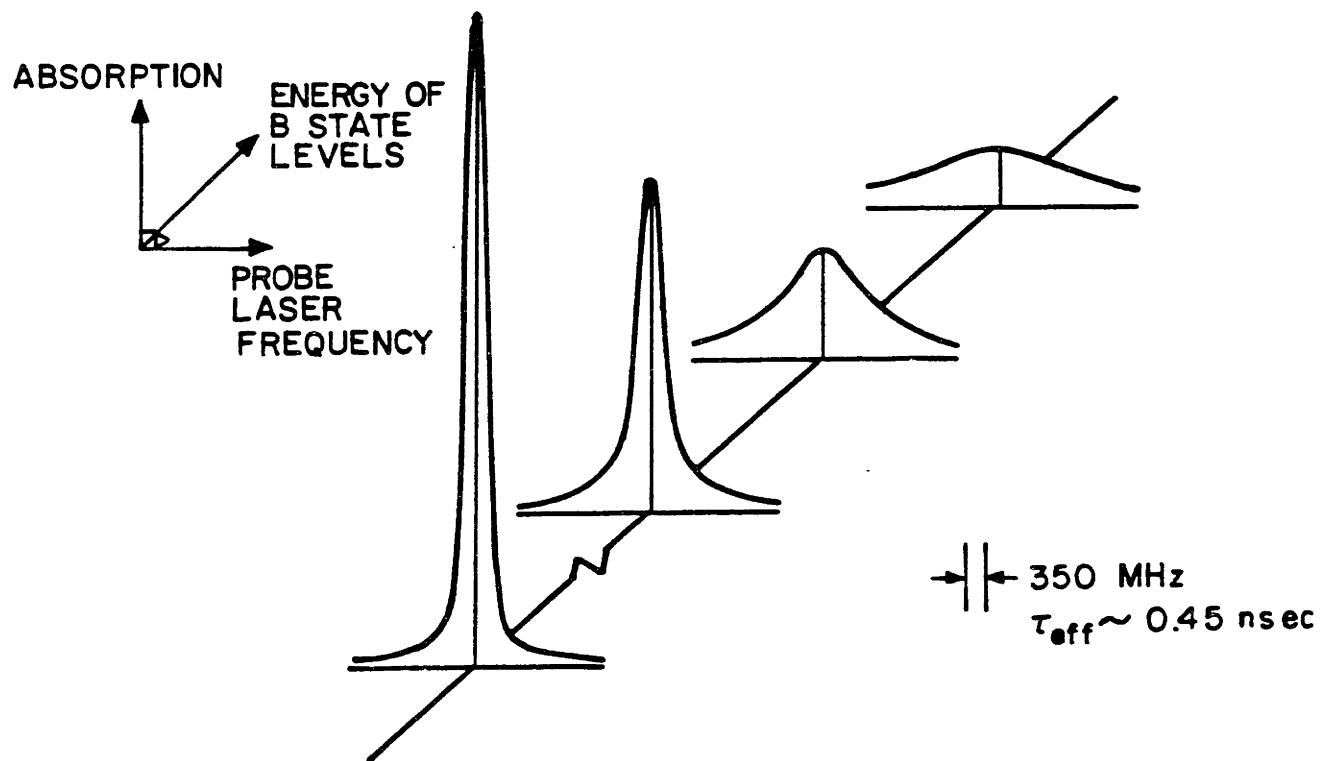
where $E^\dagger$ is the barrier maximum, and

$$[L/N] = \frac{p_0 + p_1(v_D-v) + \cdots + p_L(v_D-v)^L}{1 + q_1(v_D-v) + \cdots + q_N(v_D-v)^N}, \quad \text{and}$$

$$B(v) = (v_D-v)^{m-2} X_1 \exp\{\sum_{i=1}^{\ell_B} a_i(v_D-v)^i\} \qquad (4.4)$$

where $\qquad X_1 \equiv e^{a_0} \qquad\qquad$, and

$$D(v) = (v_D-v)^{m-4} X_2 \exp\{\sum_{i=1}^{\ell_D} b_i(v_D-v)^i\} \qquad (4.5)$$

where $X_2 \equiv e^{b_0}$.

In the above equations, $m = 2n/n-2$, where n is the asymptotically dominant power in the R^{-1} long-range expansion,

$$\lim_{v \to v_D} V(R) = C_n/R^n \qquad (4.6)$$

Notice that as v approaches v_D, Equations (4.3)-(4.5) reduce to the familiar Leroy-Bernstein, near-dissociation expressions[47],

$$G(v) = E^\dagger - (v_D-v)^m X_0(n)$$

$$B(v) = (v_D-v)^{m-2} X_1(n) \qquad (4.7)$$

$$D(v) = (v_D-v)^{m-4} X_2(n)$$

where

$$X_m(n) = \frac{\overline{X}_m(n)}{\{\mu^n (C_n)^2\}^{1/n-2}}$$

and the $\overline{X}_m(n)$ are known constants. Therefore, Equations (4.3)-(4.5)

are expansions about the limiting, near-dissociation behavior. They have been successfully used as compact representations for the energies of the ground states of H_2 and H_2^+, and for the B $^3\Pi_{0u}^+$ states of Br_2 and I_2. (The leading term in the first case is C_6/R^6, in the second case C_4/R^4, and in the third and fourth cases C_5/R^5).

It has been implicitly assumed in the derivation of Equations (4.7) (and therefore Equations (4.3)-(4.5)) that the long-range potential near dissociation can be approximated by a single term, which closely resembles the leading term in the R^{-1} expansion, i.e., Equation (4.6). If various terms in the R^{-1} expansion are not of the same sign, then this approximation is not necessarily valid. This is the case for the B state, where the leading term is a repulsive C_3/R^3 term. Under such circumstances, the usual correspondences between the fitting parameters $(X_0(3),m)$ and the potential energy parameters $(C_3,6)$ are invalid. The only physically relevant parameters in Equations (4.7) (and in Equations (4.3)-(4.5)) are E^t, v_D and a local value of n (or m). This last parameter should approach ∞ (or 2) as one approaches the barrier, as illustrated by the following argument. When $V(R) \sim C_n/R^n$, then n is a "local" value as defined by

$$-\frac{d^2V/dR^2}{dV/dR} \sim \frac{n+1}{R} \qquad (4.8)$$

Since $dV/dR=0$ at the barrier maximum and both d^2V/dR^2 and $R=R_{barrier}$ are finite, the apparent value of n near the barrier is ∞; therefore, since $m=2n/n-2$, $m=2$. Furthermore, the implications of an $m=2$ are that the $B(v)$ values are almost independent of v for levels near v_D and the $D(v)$ values approach their limiting value of ∞ at a rate of $(v_D-v)^{-2}$ (see Equation (4.4)-(4.5)).

With these expectations, we proceeded with a nonlinear least-squares fit to the energy levels. Our algorithm consisted of the following trial-and-error procedure. Since Equations (4.3)-(4.5) are not linear functions of the parameters v_D, m, $\{q_i\}$, $\{a_i\}$ and $\{b_i\}$, it is very important to make judicious first guesses for these parameters. The critical first step consisted of choosing realistic starting values of v_D and m, holding these fixed parameters at these values, and adjusting the (i+1) linear parameters, $E^\dagger$ and $\{p_i\}$. In this step the Padé expression takes the [L/0] form. The second step involved varying (i+3) parameters, where now v_D and m were also adjustable. Third and further steps incorporated additional nonlinear parameters, such as q_1 or a_1, one at a time and involved adjusting all parameters in each step. In this manner, we converged on a suitable Padé expression of the [2/2] form, with two rotational parameters X_1 and a_1, and one centrifugal distortion parameter X_2, which fitted our observed levels v=24-33 with a standard deviation of 0.005 cm^{-1}. These parameters are given in Table 4.2.

The fitted value m~2.2 is in satisfactory agreement with the expected value of m=2. The fitted value of $E^\dagger$ provides an estimate of the barrier height. Relative to the degeneracy-weighted average of the two asymptotes $\{Na\ 3s(^2S_{1/2}) + Na\ 3p(^2P_{1/2})\}$ and $\{Na\ 3s(^2S_{1/2}) + Na\ 3p(^2P_{3/2})\}$,[48] we get a value of the barrier height of

$$\Delta = 379.3 \pm 2.3\ cm^{-1}\ . \tag{4.10}$$

The 3σ error is based upon the statistical uncertainty of the fitted $E^\dagger$ as well as the 1.0 cm^{-1} uncertainty of the ground state dissociation energy.[49] The fitted v_D=34.01 ±0.03 does not uniquely determine the total number of quasibound rotationless vibrational levels. We note however

TABLE 4.2 Parameters in the term value fit to the observed

B state energy levels of Table 4.1. The quoted uncertainties

are 1σ. The number of digits in the constants is sufficient to

reproduce the calculated energy values to within 0.0005 cm^{-1}.

$E^{\dagger}$ = 23369.5223 ± 0.4

v_D = 34.013874 ± 0.03

m = 2.1738232 ± 0.004

p_0 = 56.857302 ± 3.5

p_1 = 6.1442025 ± 0.8

p_2 = 0.021936280 ± 0.007

q_1 = 2.1053627 ± 0.1

q_2 = 0.11633774 ± 0.02

X_1 = 0.058112743 ± 0.0002

a_1 = 7.0425655 ± 0.6 · 10^{-3}

X_2 = 5.7922974 ± 0.4 · 10^{-6}

TABLE 4.3 Parameters in the term value fit to calculated energies for

v=0-21 from Kusch and Hessel and to our observed energies for

v=24-33. Quoted uncertainties are 1σ.

$E^{\dagger}$ = 0.2336927943D+05 ± 0.5

v_D = 0.3399701070D+02 ± 0.3

m = 0.2165174468D+01 ± 0.003

p_0 = 0.5795065166D+02 ± 3.3287157695D+01

p_1 = 0.7422516977D+01 ± 0.6523982456D+00

p_2 = 0.5364829078D-01 ± 0.7880601831D-02

p_3 = -0.5161324922D-03 ± 0.8853285483D-04

p_4 = 0.3509271551D-05 ± 0.6242688591D-06

q_1 = 0.2154578560D+01 ± 0.1200349356D+00

q_2 = 0.1494929355D+00 ± 0.1348419923D-01

X_1 = 0.5807725618D-01 ± 0.2053662808D-03

a_1 = 0.1144683358D-01 ± 0.6761979322D-03

a_2 = -0.2724772942D-03 ± 0.2213395632D-04

a_3 = 0.2864429175D-05 ± 0.2916290316D-06

X_2 = 0.5624021035D-05 ± 0.7015077522D-06

TABLE 4.4 RKR turning points for the B $^1\Pi_u$ potential, based on the term value parameters of Table 4.3.

V	E(V)	B(V)	RMIN(V)	RMAX(v)
0.00	62.0033	0.1253377136	3.2679970001	3.5757829453
1.00	184.9102	0.1243680217	3.1697668137	3.7056736613
2.00	306.2061	0.1233898368	3.1060402929	3.8015199356
3.00	426.1666	0.1224001947	3.0564439494	3.8837525524
4.00	544.4651	0.1213761238	3.0150866125	3.9583191662
5.00	661.1728	0.1203745379	2.9792901424	4.0279599334
6.00	776.2584	0.1193327272	2.9475725654	4.0942217819
7.00	889.6890	0.1182673489	2.9190150865	4.1580924699
8.00	1001.4278	0.1171754155	2.8930025576	4.2202596756
9.00	1111.4363	0.1160537812	2.8691048835	4.2812352539
10.00	1219.6727	0.1148992252	2.8470011417	4.3414218891
11.00	1326.0920	0.1137084319	2.8264919967	4.4011520567
12.00	1430.6461	0.1124779654	2.8072693375	4.4607124998
13.00	1533.2828	0.1112042391	2.7893062521	4.5203606633
14.00	1633.9462	0.1098834763	2.7724429317	4.5803365029
15.00	1732.5755	0.1085116507	2.7565816635	4.6408716170
16.00	1829.1055	0.1070844730	2.7416414222	4.7021969221
17.00	1923.4649	0.1055972082	2.7275542001	4.7645496989
18.00	2015.5762	0.1040446682	2.7142622523	4.8281806756
19.00	2105.3549	0.1024210175	2.7017159929	4.8923617578
20.00	2192.7021	0.1007195902	2.6898723613	4.9603950821
21.00	2277.5334	0.0989326243	2.6726935470	5.0296242445
22.00	2359.7170	0.0970508904	2.6681460043	5.1014488929
23.00	2439.1317	0.0950631604	2.6581997362	5.1763444620
24.00	2515.6342	0.0929554259	2.6488276770	5.2548898640
25.00	2589.0613	0.0907097138	2.6400565728	5.3378073135
26.00	2659.2249	0.0883022171	2.6317161496	5.4260260080
27.00	2725.9049	0.0857002091	2.6239418365	5.5207745244
28.00	2788.8385	0.0828566328	2.6165787979	5.6237504625
29.00	2847.7028	0.0796999328	2.6099396892	5.7374190275
30.00	2902.0838	0.0761127284	2.6037710695	5.8656273655
31.00	2951.4124	0.0718808114	2.5922927719	6.0150735003
32.00	2994.7975	0.0665406908	2.5936728811	6.1998576465
33.00	3030.3959	0.0586490905	2.5897897022	6.4645775010

that if the value of m had been fixed at its predicted value of 2, then the least-squares adjusted value of v_D would have fallen below 34. We will see in Section Six that the potential barrier predicted by the J-dependent tunneling lifetimes of v=33 does not bound a v=34 level.

B. RKR Potential

We can also extend knowledge of the bound portion of the B state potential from our observed data by using the RKR inversion procedure. This requires representing our G(v)'s and B(v)'s and those of Kusch and Hessel (for v=0-29) in a composite fashion. Since we did not have access to their B←X frequencies, we calculated the energies for the v=0-21, J=1 and J=14 levels, based on the molecular constants of their analysis II. These energies were then combined with ours (for v=24-33) and fit, using Equations (4.2)-(4.5). The resulting [4/2] Padé, with four rotational constants X_1, a_1-a_3, and one distortion constant, X_2, is given in Table 4.3.

Using these constants, the RKR potential of Table 4.4 was generated. The outer turning points for the last few vibrational levels determine the shape of the inner wall of the barrier. We will find the outer turning point for v=33 especially important when determining the potential barrier from the tunneling lifetimes (Section 4.6).

4.4 Analysis of MGS Lineshapes

From the line frequencies in the MGS spectrum, we were able to determine several features of the barrier, such as the shape of its inner wall, an approximate height of the barrier maximum, and an estimate of the total number of quasibound vibrational levels supported by it. Additional information about the barrier is contained in the linewidths

of the MGS spectrum. The linewidths can reflect the rate at which the quasibound levels are tunneling.

To determine the lifetimes from the full-widths, it was necessary to fit the spectral lines to their appropriate lineshape profiles. The observed lineshapes contained contributions from two effects:

1) First, there are some out-of-phase (decreases in the OPL output caused by other probe resonance schemes mentioned in Chapter Two) which are superimposed on the in-phase B state signals and thus distort the true line-shapes. This problem becomes more severe as the quasibound level widths increase since the number of overlapping out-of-phase signals increases (about 5 out-of-phase signals per 20 GHz); therfore, a simple graphical determination of the widths is impossible, and

2) Secondly, we must account for those homogeneous and inhomogeneous contributions to the MGS signal that are present in the absence of tunneling (mentioned above); these must be deconvoluted out to give the contribution made to the full-width by the tunneling rate alone.

Figure 4.3a) shows the observed intensity profile for a level that does not exhibit any detectable tunneling. Superimposed on this signal are the lineshape fits using pure Gaussian $G(\Delta,\omega_0-\omega)$ and Lorentzian $L(\Gamma,\omega_0-\omega)$ functions,

$$L(\omega_0-\omega,\Gamma) = I_0 \frac{\Gamma/2\pi}{(\omega_0-\omega)^2 + \Gamma^2/4} + I_b$$

$$(4.11)$$

$$G(\omega_0-\omega,\Delta) = I_0 \exp\{\frac{-4(\omega_0-\omega)^2}{\Delta^2}\} + I_b \quad .$$

I_0 is the peak intensity; Γ and $\Delta[\ell n2]^{1/2}$ are the full-width-at-half-intensity for respectively the Lorentzian and Gaussian functions; ω_0 is

line-center frequency; I_b is the baseline. While both of these lineshape fits were adequate around the peak of a line , they severely over- or underestimated the decay of the wings. These inadequacies suggested the use of a Voigt profile. The Voigt profile is a convolution of the Lorentzian and Gaussian lineshapes, i.e.,

$$V(\omega_0-\omega,\Gamma/\Delta) = \int_0^\infty G(\omega_0-\omega,\Delta) \; L(\omega_0-\omega,\Gamma) \; d\omega \quad , \qquad (4.12)$$

and is uniquely determined by the ratio, Γ/Δ.

Figure 4.3 b) shows a satisfactory Voigt fit to the same signal shown in Figure 4.3 a). The Lorentzian and Gaussian full-widths for this signal are determined to be 137±28 MHz and 286±22 MHz, respectively.

The radiative lifetimes of the B-state levels are typically 6-7 nsec corresponding to natural linewidths of ~20 MHz. Homogeneous effects such as pressure broadening (and power broadening) dominate the Lorentzian linewidth, and arise primarily from collisions between Na_2 and Na at 1 Torr. The Gaussian linewidth of 286 MHz arises because the PROBE excites a non-δ-function axial velocity distribution in the lower OPL level. This velocity spread is created primarily by a two-photon, Raman contribution to the gain of the OPL[23].

Line broadening above the ~350 MHz lower bound was observed for the rotational levels of v=33 only. Let us now anticipate the two major lineshape considerations for the broadened lines. Firstly, when the lifetime of the quasibound levels is dominated by tunneling through the barrier, the MGS lines are expected to have a Lorentzian lineshape. This can be seen from the following argument. For a given energy, E, the

Figure 4.3 (a) Lorentzian (—) and Gaussian (---) lineshape fits to a

signal which does not exhibit tunneling broadening. This MGS

signal corresponds to excitation to the v=31, J=10 level of

the B state.

(b) Voigt lineshape fit to the same signal.

A

B → X (31, 44) P(11)

OPL INTENSITY

... OBS
— LORENTZIAN
FIT
--- GAUSSIAN
FIT

PROBE FREQUENCY

B

B → X (31, 44) P(11)

OPL INTENSITY

... OBS
— VOIGT FIT

0. 31
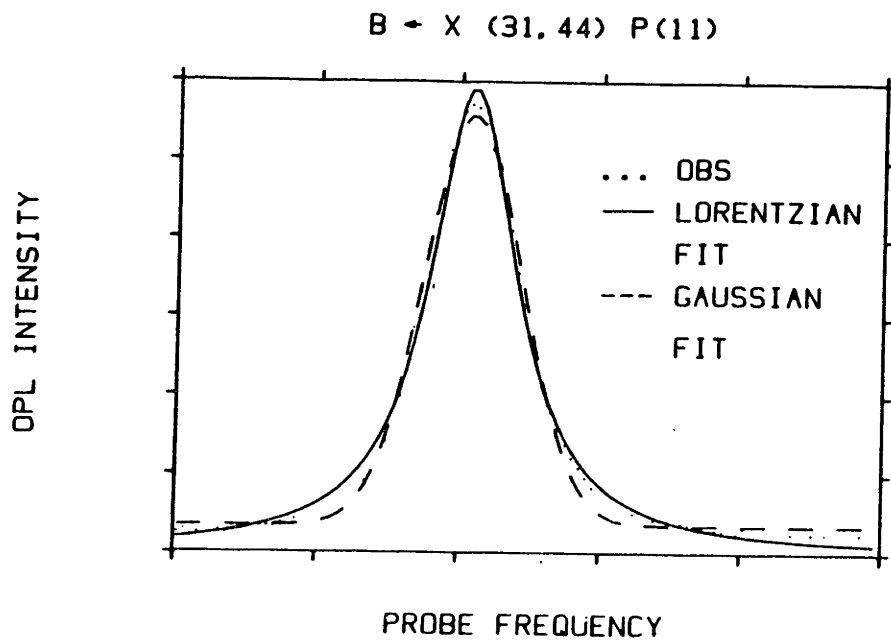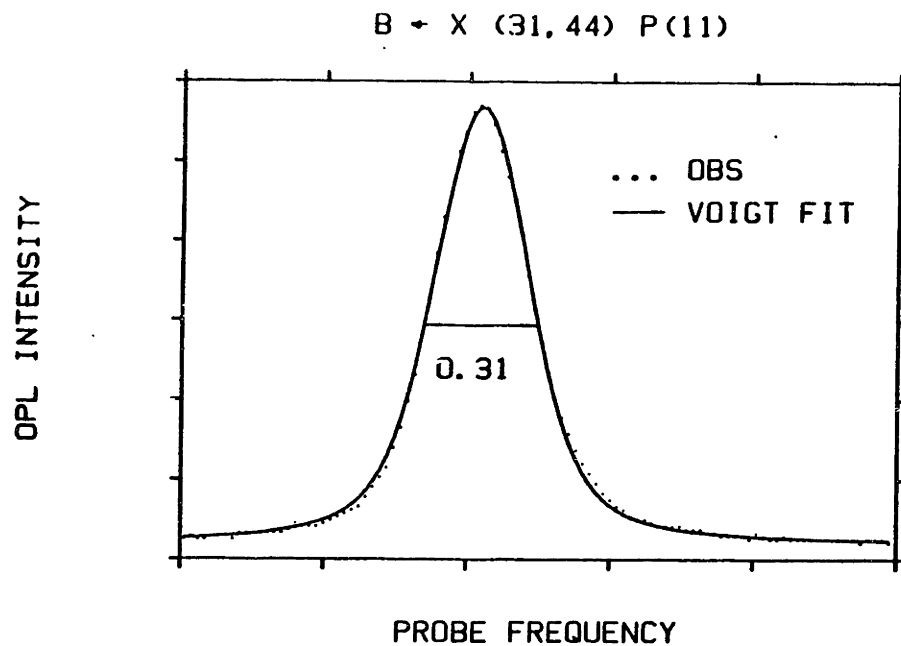
PROBE FREQUENCY

tunneling probability, P, is independent of time. (Its functionality

is discussed in the next section). In terms of the vibrational

frequency, ω, and the tunneling probability, the rate of decay of excited

molecules is given by

$$dN/dt = -(\omega P)N$$

$$\therefore N = N_0 \exp(-\omega Pt)$$

(4.13)

Thus the population decays exponentially with time and the Fourier

transform of N (i.e. the lineshape) is a Lorentzian.

The second lineshape consideration for the broadened lines concerns

the out-of-phase signals which invariably overlap with this main

Lorentzian MGS signal. Since most of the out-of-phase signals arise from

the probe interacting with a thermal distribution of velocities in the

lower pump level (see Chapter Two), they should be described by

predominantly Gaussian profiles. Therefore, the least-squares fitting

procedure for the tunneling-broadened lines consisted of assuming pure

Lorentzian lineshapes for the main signal and pure Gaussian lineshapes for

the superimposed out-of-phase resonances. The parameters typically varied

were the full-width, peak intensity, and line-center frequency for the

in-phase signal and for each out-of-phase signal, and the baseline (which

often could not be determined unambiguously by eye). The resultant

Lorentzian full-widths for the main, in-phase signal were then corrected

for the residual homogeneous contribution that is present in the absence

of tunneling, by subtracting ~150 MHz. Typical three-standard-deviation

uncertainties in the fitted linewidths were 1-2% of the linewidths.

Examples of the lineshape fits to the tunneling-broadened lines are shown

Figure 4.4 Lineshape fits (——) to tunneling-broadened signals. The

extracted Lorentzian lineshapes (---) give the tunneling

contribution to the full-widths. These are (a) J=4 with 1.88

GHz (b) J=10 with 2.96 GHz and (c) J=13 with 5.8 GHz.

B ← X (33,44) Q(4)

PROBE FREQUENCY

OPL INTENSITY

134

B → X (33,44) P(11)

····· Observed

—— Lineshape Fit

– – – Lorentzian Contour

2.96

PROBE FREQUENCY

OPL INTENSITY

B←X (33,50) Q(13)

· · · · Observed
———— Lineshape Fit
– – – Lorentzian Contour
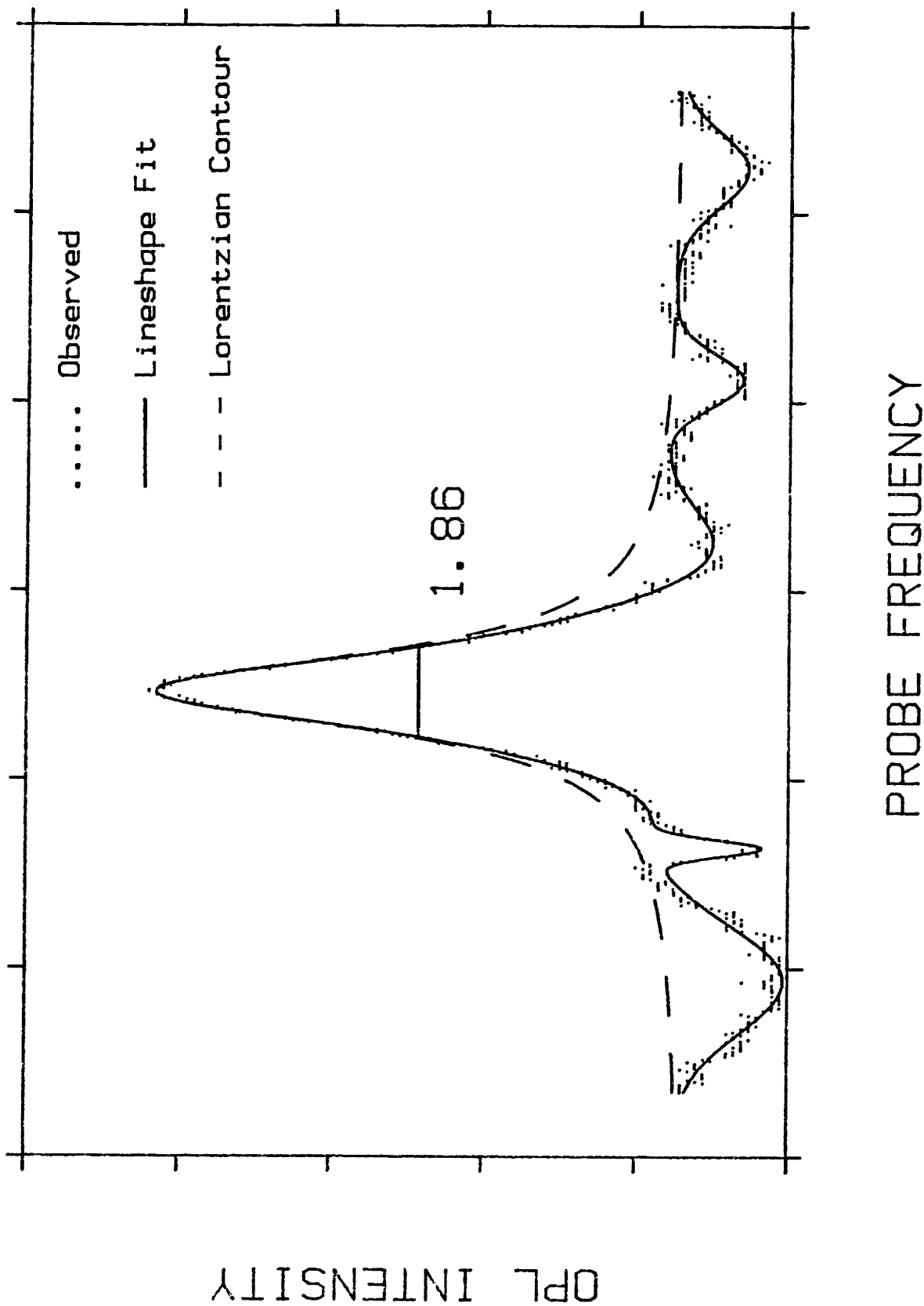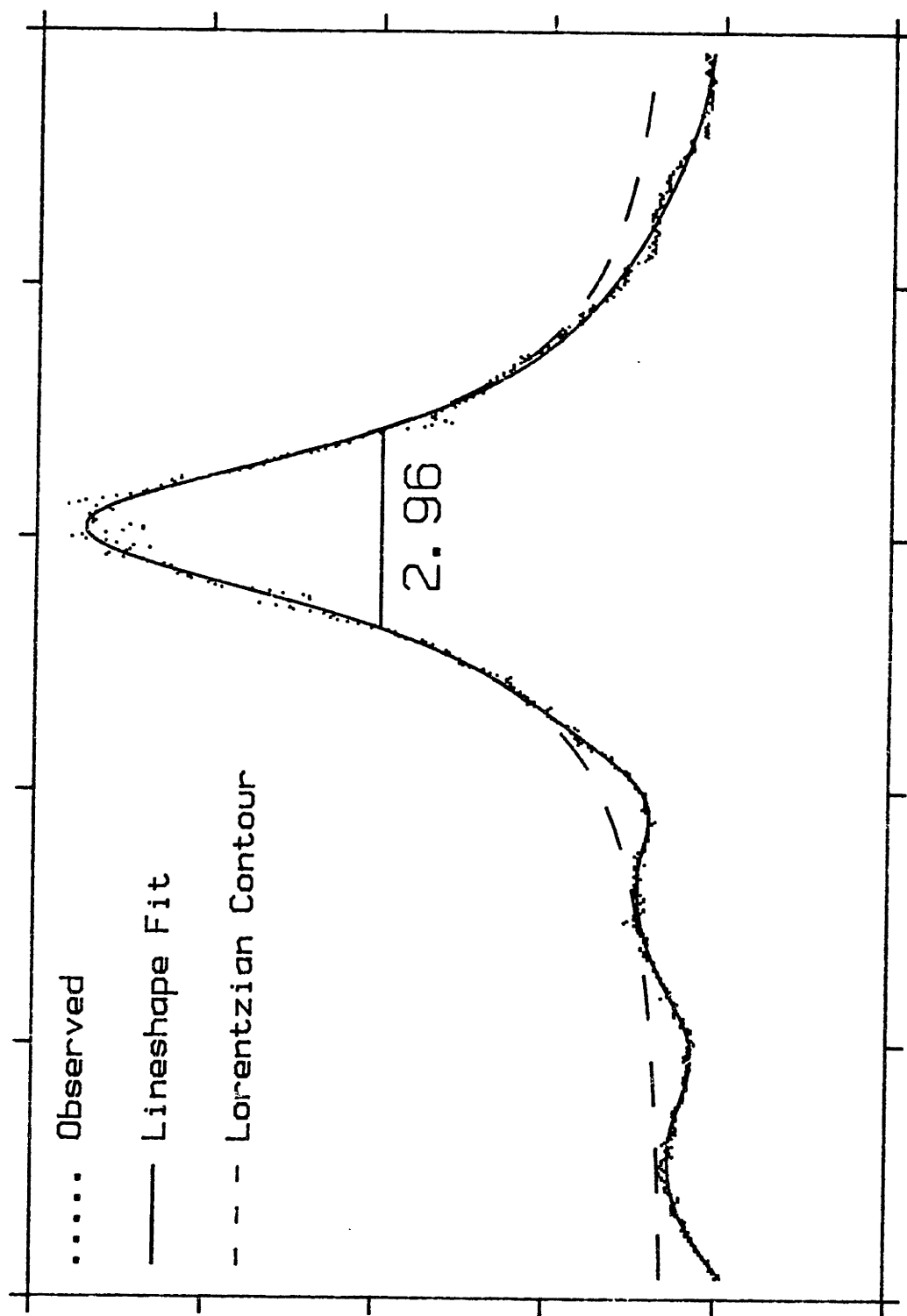
OPL INTENSITY
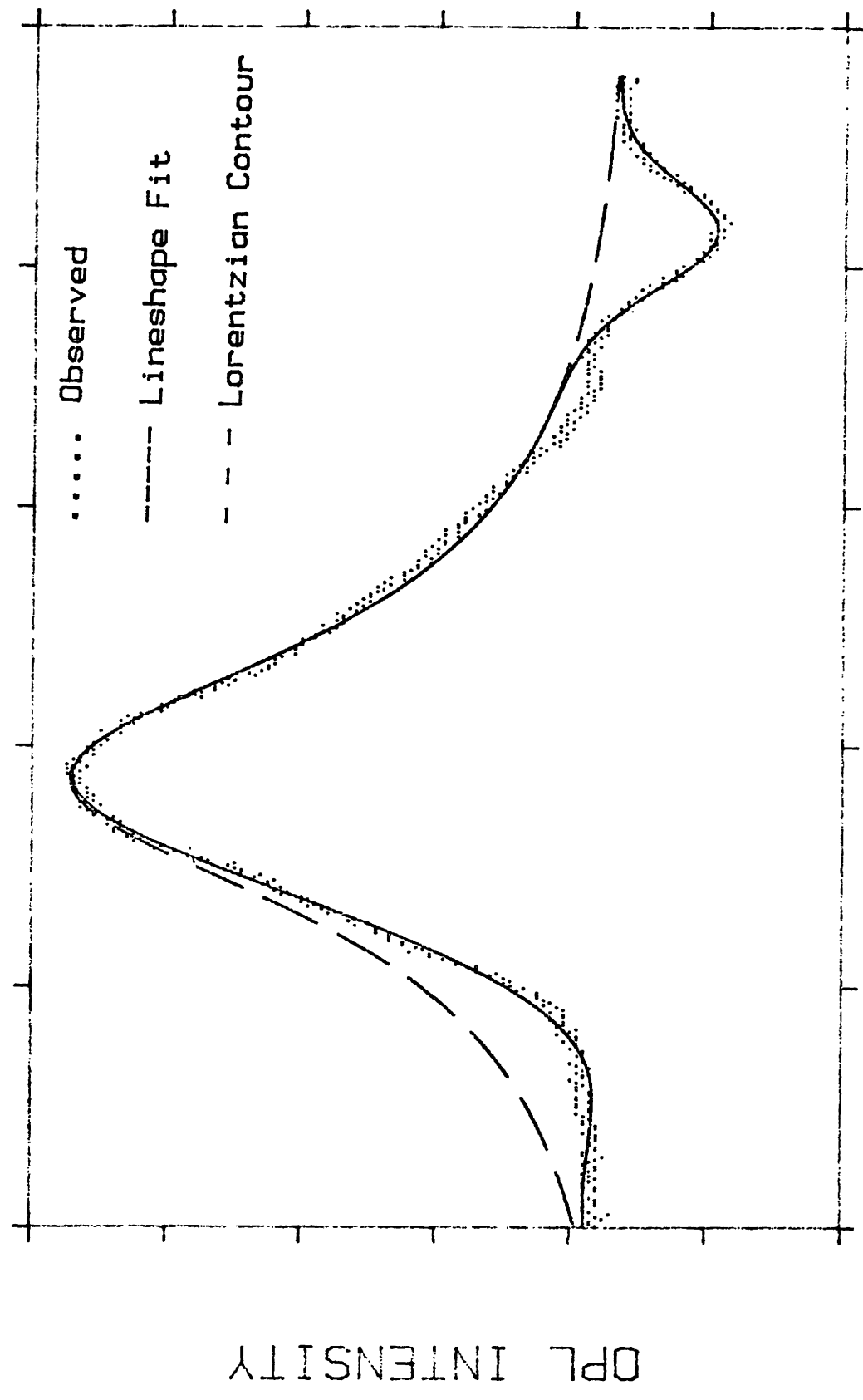
PROBE FREQUENCY

in Figures 4.4. The limiting accuracy of the fitted linewidths was not determined by the statistical errors of the fit, but rather by two kinds of errors introduced by the out-of-phase signals. The first error had its origin in the fitted widths of the out-of-phase resonances, which tended to be larger than the 1.5 GHz Doppler width (at T~460°C). The excess linewidth was often due to an obvious overlap of two out-of-phase signals which were not resolvable by the fit. In order to estimate what effect an incomplete model for the out-of-phase signals might have on the main signal widths, all fits were repeated with the out-of-phase widths held fixed at 1.5 GHz. The resulting main signal widths differed from those obtained in the first procedure (where each out-of-phase width was free to vary) by ~3% for small J and 0-1% for higher J.

The second and more severe error in the linewidth determination arose because different main signal widths were obtained when different excitation schemes, leading to the same upper J, were used (i.e., either a different lower laser level, v", or P- vs. R-excitation from the same v"). These differences ranged from 1% to 19% for the high J (J' = 11-17) lines. Some of these deviations might be explained by the fact that in many of the high J fits (J' > 13), where there were a large number of out-of-phase signals, the number of least-squares adjustable parameters had to be limited in the fitting procedure. Therefore the least critical parameter, the baseline, was held fixed at a value which may not have been determined accurately enough by eye.

Therefore, we quote a 3σ uncertainty for the full-widths of 3% for $3 < J' < 10$ lines and 6% for the $J' > 10$ lines. The 6% standard deviation is an average of the standard deviations obtained for each excitation line leading to the same upper J. For example,

138

$$\sigma(J{=}14) = \frac{\sigma(R_{13}) + \sigma(P_{15})}{2} \qquad (4.14)$$

The resulting lifetimes are reported in Table 4.5

4.5 WKB Transmission Probability

The tunneling lifetimes of various rotational levels in v=33, obtained from the lineshape fits, were used to determine the shape of the potential barrier near the maximum. The model used assumed that the tunneling rate is given by the product of the frequency with which the molecule hits the barrier, ω, times the probability of transmission per collision, P. Thus,

$$\tau = 1/\omega P \qquad \bullet \qquad (4.15)$$

The collisional frequency, ω, is simply the J-dependent, vibrational frequency and can be determined from Equations (4.2)-(4.5) by using the definition,

$$\omega(v,J) \equiv \frac{\partial E(v,J)}{\partial v} \qquad \bullet \qquad (4.16)$$

The probability, P, expressed in terms of the WKB phase integral, Φ, is

$$P(v,J) = [1 + \exp(2\Phi)]^{-1} \qquad (4.17)$$

where

$$\Phi(v,J) = \frac{1}{\hbar} \int_{r_<}^{r_>} \{2\mu[U(r,J) - E(v,J)]\}^{1/2} dr \qquad (4.18)$$

and $r_<,r_>$ (which are also v and J dependent) are the inner and outer classical turning points of the barrier (i.e where $E(v,J) = U(r,J)$). Since the tunneling lifetimes, τ, the energies, $E(v,J)$, and the vibrational frequencies, $\omega(v,J)$, are known, the potential barrier, $U(r,J)$ can be determined.

TABLE 4.5 J dependence of the tunneling lifetimes for the quasibound

level, v = 33. Also shown is the e/f parity of the particular

rotational level excited. The lifetimes are calculated from the

fitted full widths at half maximum, Δ_{FWHM}, using $\tau = 1/2\pi\Delta_{FWHM}$.

J'		τ (ps)
1		*
2		*
3	e	93.5 ± 2.8
4	f	91.9 ± 2.8
5	e	77.2 ± 2.3
6		*
7	e	74.4 ± 2.2
8	f	70.5 ± 2.1
9	e	68.7 ± 2.1
10	e	55.7 ± 1.7
11	f	42.8 ± 2.6
12	e	38.6 ± 2.3
13	e	28.0 ± 1.7
14	f	25.1 ± 1.5
15	e	22.6 ± 1.4
16	e	18.7 ± 1.1
17	f	18.3 ± 1.1

*J' = 1, 2, and 6 were not observed because we did not populate, via

any of the PUMP-OPL schemes, J" = 1-3 or 5-7 in the lower OPL level.

It is not possible to invert Equation (4.18) and obtain a closed form expression for the potential barrier in terms of the J-dependent lifetimes. Therefore, it is necessary to adopt a functional form for the barrier with some adjustable parameters. A least-squares optimization of these parameters by a fit to the tunneling lifetimes then yields the shape of the potential barrier, assuming that a reasonable representation for the barrier has been chosen.

Before discussing the functional form used and the subsequent fits, let us first explain why the tunneling probability of Equation (4.17) is used instead of the more standard form, $P = \exp(-2\phi)$. Equation (4.17) has an extended range of validity near the top of a barrier where the standard form, $P = \exp(-2\phi)$ tends to break down. The reason for the breakdown can be understood from the following line of reasoning. It is well-known that the WKB approximation fails at a turning point. The usual procedure taken to overcome this difficulty is to expand the potential in a Taylor series about the turning point, r_0, and retain only terms linear in $(r-r_0)$, i.e.

$$V(r) = V(r_0) + \frac{\partial V}{\partial r}\bigg|_{r=r_0}(r-r_0) + \frac{1}{2}\frac{\partial^2 V}{\partial r^2}\bigg|_{r=r_0}(r-r_0)^2 \qquad . \qquad (4.19)$$

This approximation becomes increasingly inaccurate as one approaches the top of the barrier, at which the slope becomes zero. Thus, near the top of the barrier, the quadratic term in the above Taylor series must be retained (and a parabolic barrier maximum is assumed). The exact solutions of the Schrödinger equation, for this quadratic potential, can be expressed in terms of parabolic cylinder functions[50] (just as the exact solutions for a linear potential are Airy functions). The

·asymptotic forms of these parabolic cylinder functions are then matched with the WKB solutions, which are valid away from the turning point. (This is known as the Weber boundary condition.)[50] The resulting WKB solutions in the regions $r < r_<$ and $r > r_>$ yield the barrier transmission probability given by Equation (4.17). For levels far below the top of the barrier, $\exp(2\phi) \gg 1$, and the transmission approaches the more familiar result, $P = \exp(-2\phi)$. For levels very near the top, however, this simpler result grossly overestimates the transmission. Figure 4.5 compares the result of the modified WKB formula with that of $P = e^{-2\phi}$.

From Equations (4.15) -(4.18), what might we anticipate for the variation of tunneling lifetimes vs. J? Note that there is a different potential barrier for each J because of a different amount of centrifugal energy associated with each J. Therefore, as J increases, the total energy E(J) as well as the effective potential U(J) increase. This is illustrated in Figure 4.6. At first thought, it is not obvious whether one would expect the tunneling lifetimes (which are related to the area enclosed by the potential and the energy level) to decrease steadily with increasing J. However a closer study shows that, for a given vibrational level, the tunneling lifetimes will decrease as J increases. The J dependence of the lifetimes, from Equation (4.15), is given by

$$\partial\tau/\partial J = \frac{-1}{(\omega \cdot P)^2} \, [(\partial P/\partial J)\omega + (\partial\omega/\partial J)P] \quad . \tag{4.20}$$

We know that $\partial\omega/\partial J$ is negative and ω and P are both positive; hence, we need only determine the sign of $\partial P/\partial J$. From Equations (4.17-4.18),

142

Figure 4.5 Comparison of transmission through a barrier with maximum V_0,

as predicted by Equation (4.17) (which is exact for a

parabolic barrier) and the usual WKB result. (From Ref. 50b).
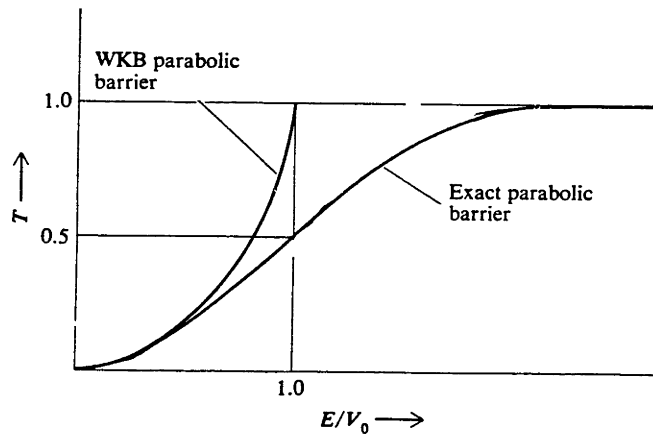
Figure 4.6 Variation of the effective potential, U(J), and the rotational energy, E(J), with J.
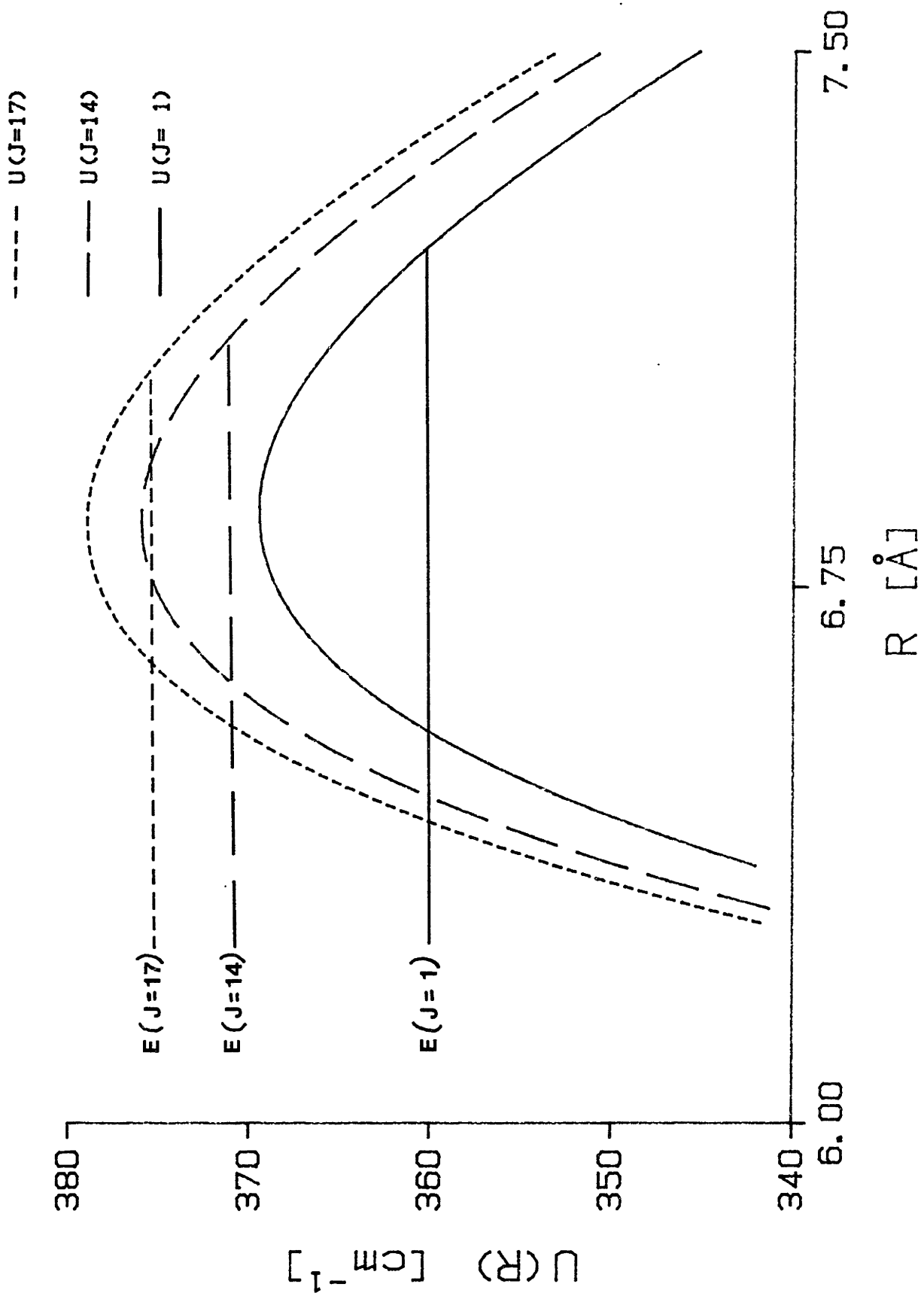
Figure 4.7 Observed tunneling lifetimes for the J=3-17 levels of v=33.
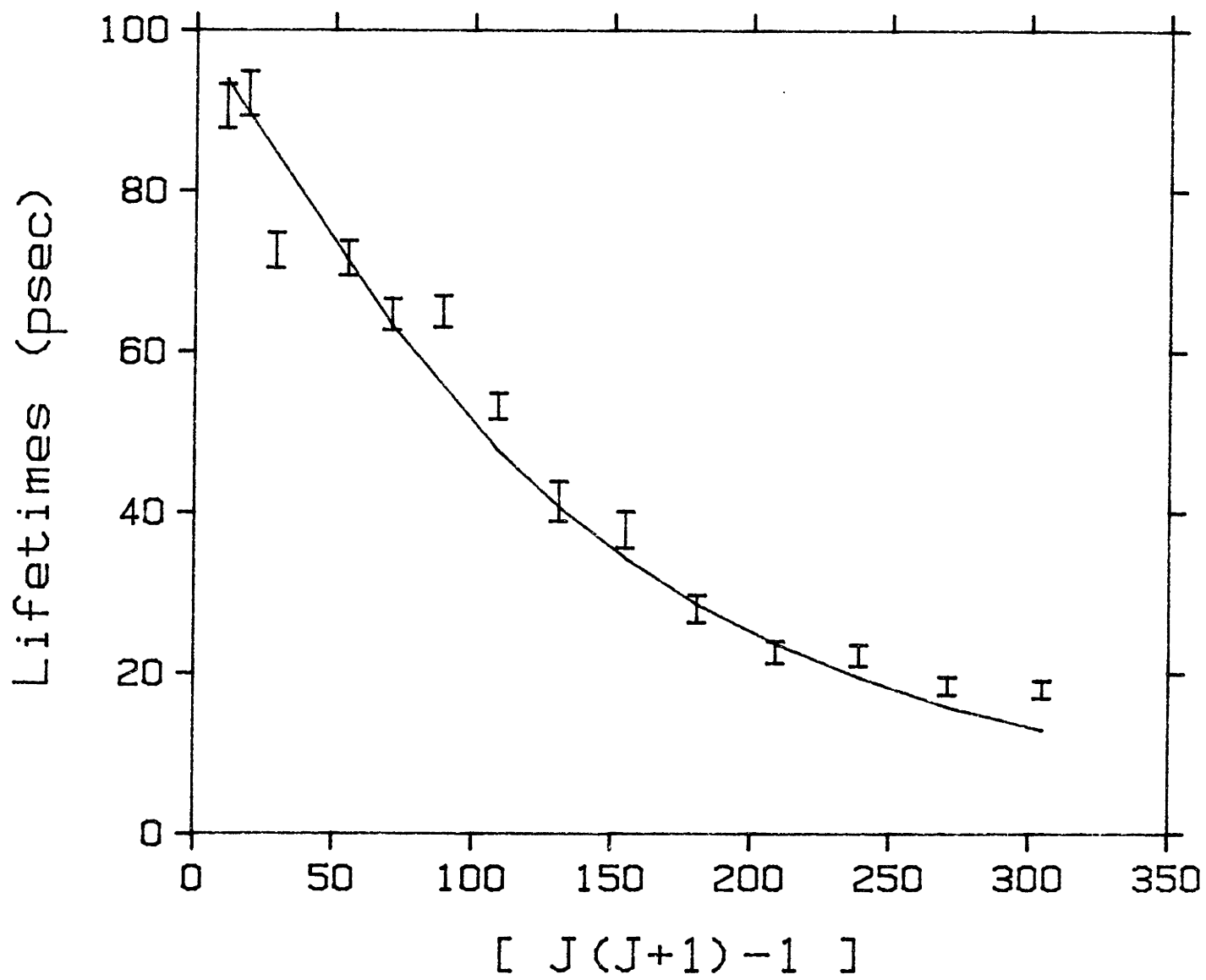
$$\partial P/\partial J = -2 \exp(2\Phi) \cdot [1+ \exp(2\Phi)]^{-2} \cdot \partial\Phi/\partial J$$

where

$$\partial\Phi/\partial J = \frac{\mu}{\hbar} \int_{r_<}^{r_>} \frac{(\partial U/\partial J - \partial E/\partial J)}{[2\mu(U - E)]^{1/2}} \, dr \qquad . \qquad (4.21)$$

It is evident that the sign of $\partial P/\partial J$ is determined by the factor, $(\partial U/\partial J-\partial E/\partial J)$, since ϕ is a positive quantity. Now, $E(J)$ is given approximately by $E(J) \simeq B[J(J+1)-1]$; therefore

$$\partial E/\partial J \simeq \frac{(2J+1)\hbar^2}{2\mu\langle r^2\rangle} \qquad (4.22)$$

where $\langle r^2\rangle$ is evaluated over the inner and outer turning points of the potential well. The effective potential is given by

$$U(J) = U_{J=0} + \frac{\hbar^2}{2\mu r^2} [J(J+1)-1] \quad ;$$

therefore,

$$\partial U/\partial J = \frac{(2J+1)\hbar^2}{2\mu r^2} \qquad (4.23)$$

where r^2 is considered in the interval between the inner and outer turning points of the potential barrier (i.e. betwen $r_<$ and $r_>$). If we combine Equations (4.22)-(4.23),

$$(\partial U/\partial J - \partial E/\partial J) = \frac{\hbar^2}{2\mu} (2J+1)[\frac{1}{r^2} - \frac{1}{\langle r^2\rangle}] \qquad (4.24)$$

we see that $(\partial U/\partial J-\partial E/\partial J)$ is a negative quantity since r^2, for the potential barrier, is greater than $\langle r^2\rangle$ for the potential well. That this factor is negative implies $\partial P/\partial J$ is positive and in turn $\partial\tau/\partial J$ is negative; i.e., the tunneling lifetimes decrease with increasing J. These

expectations are consistent with our observations; Figure 4.7 shows an essentially monotonic decrease in lifetimes as J increases.

4.6 From Tunneling Lifetimes to Potential Barrier

The tunneling lifetimes can be inverted to yield the shape of the potential barrier in the following manner. The least squares fits of the lifetimes are performed using Equations (4.15)-(4.18) with the following representation for the potential barrier:

$$U(r,J) = D_e + \frac{C_3}{r^3} + \frac{C_6}{r^6} + \frac{C_8}{r^8} + A\exp(-Br) + \frac{\hbar^2}{2\mu r^2}[J(J+1)-1] \qquad (4.25)$$

| ZERO OF ENERGY | LONG-RANGE | EXCHANGE | CENTRIFUGAL |

The potential is described by a sum of long-range (r^{-n} terms) and electron-exchange (Ae^{-Br}) contributions for the following reason. Overlap of the separated atom wave functions for the Na(3p)+Na(3s) atoms, is considered negligible for interatomic separations greater than 9.2Å; therefore, in these regions only long-range contributions to the potential need to be considered. We are interested in regions of the potential near the barrier maximum, located at ~7Å, where there is nonnegligible overlap. The electron-exchange interactions between the two atoms that arise by virtue of the overlap must therefore be accounted for. We represent the exchange contribution by the phenomenological, exponential function of r, with two parametrs A and B. For the $^1\Pi_u$ state, the exchange energy is attractive and A is therefore negative.

Equation (4.25) should adequately represent the total potential energy, which consists of the zero-order energy, D_e ($E^{(0)}$ of Chapter Three) for the Na(3p) + Na(3s) atoms, and corrections to this energy from

long-range and electron-exchange interactions. The centrifugal

contribution is important since we measure the J dependence of the

tunneling lifetimes.

In principle, $\{C_3,C_6,C_8,A,B\}$ can all be treated as parameters to be

least-squares determined from the tunneling lifetime fits. However, we

quickly found very high correlations between both (C_6,C_8) and the C_3 term.

Therefore, the C_6 and C_8 coefficients were held fixed at the ab-initio

values of Bussery.[12] Initially, it was also not apparent whether the one

order-of-magnitude variation in the observed tunneling lifetimes was

sufficient to determine independently the C_3 coefficient from the A and B

exchange parameters. As a result, two types of fits were performed: Fit

I, with three adjustable parameters $\{C_3,A,B\}$ and Fit II, with two adjust-

able parameters $\{A,B\}$ where C_3 was fixed at a value given by the experi-

mentally-determined Na D-lines oscillator strengths of Gaupp, et al.[51]

In the course of these fits, we discovered that although the

tunneling lifetimes were sensitive to the height and shape of the barrier,

they were insensitive to the internuclear distance of the barrier maximum.

In order to determine a physically meaningful barrier, whose inner wall

joins smoothly onto the RKR-determined potential well, fits I and II were

performed to Equations (4.15)-(4.18) and (4.25), subject to the heavily

weighted datum,

$$U(r_0) = E_0$$

where (E_0,r_0) are the energy and RKR outer turning point for the $v=33$, $J=1$

level (obtained from the RKR curve of Table 4.5). Figure 4.7 shows the

results of fits (I) and (II); both satisfactorily reproduce the

J-dependent lifetimes. The values of the barrier parameters from these

two fits are shown in Table 4.5.

We can summarize the three major findings:

(1) Errors in the assumed values of C_6 and C_8 (±1% for C_6 and ±10% for C_8) had inconsequential effects on the values of the least-squares-adjusted parameters.

2) The C_3 coefficient of fit I underestimates the fixed value of C_3 used in fit II by ~9%. (We note that Gaupp, et al. oscillator strength measurements are reported to 0.2% accuracy.) This outcome is not clearly understood. Since the C_3 coefficient is positive and the exchange parameter A is negative, the underestimated C_3 coefficient of fit I leads to an overestimated exchange energy, relative to that given by fit II.

3) While the two fits appropriated the C_3/r^3 and Aexp(-Br) contributions to the potential energy differently, the height and shape of the potential barrier (over the internuclear distances sampled by the tunneling levels) predicted by both fits are virtually the same.

Since fit II employs an accurate C_3 coefficient, which properly predicts the outer tail of the potential barrier, and this same fit satisfactorily accounts for the observed variation of tunneling lifetimes, which reflect the height and shape of the barrier near the maximum, we feel the results of this fit II provide the better description of the overall B state potential barrier (see Figure 4.8). Thus, the barrier height and position are

$$U_{max} = 369.5 \pm 3.9 \text{ cm}^{-1}$$

$$R_{max} = 6.85 \pm 0.02\text{Å}$$

This result is substantially lower than previous works have suggested, as shown in Table 4.6.

Figure 4.8 Potential barrier of the B $^1\Pi_u$ state obtained from the tunneling lifetimes: (a) shows the internuclear separations sampled by the v=33, J=3-17 tunneling levels and (b) shows extended regions of the inner and outer walls of the potential barrier. The inner wall is determined by the v=29-33, J=1 RKR turning points.

x RKR turning point
for v = 33, J = 1

Figure legend:

— Fit II of this work

— — C_9/R^9 contribution

× RKR turning points for v= 28-39, J=1 levels

Axes:

R [Å]

U(R) [cm^{-1}]
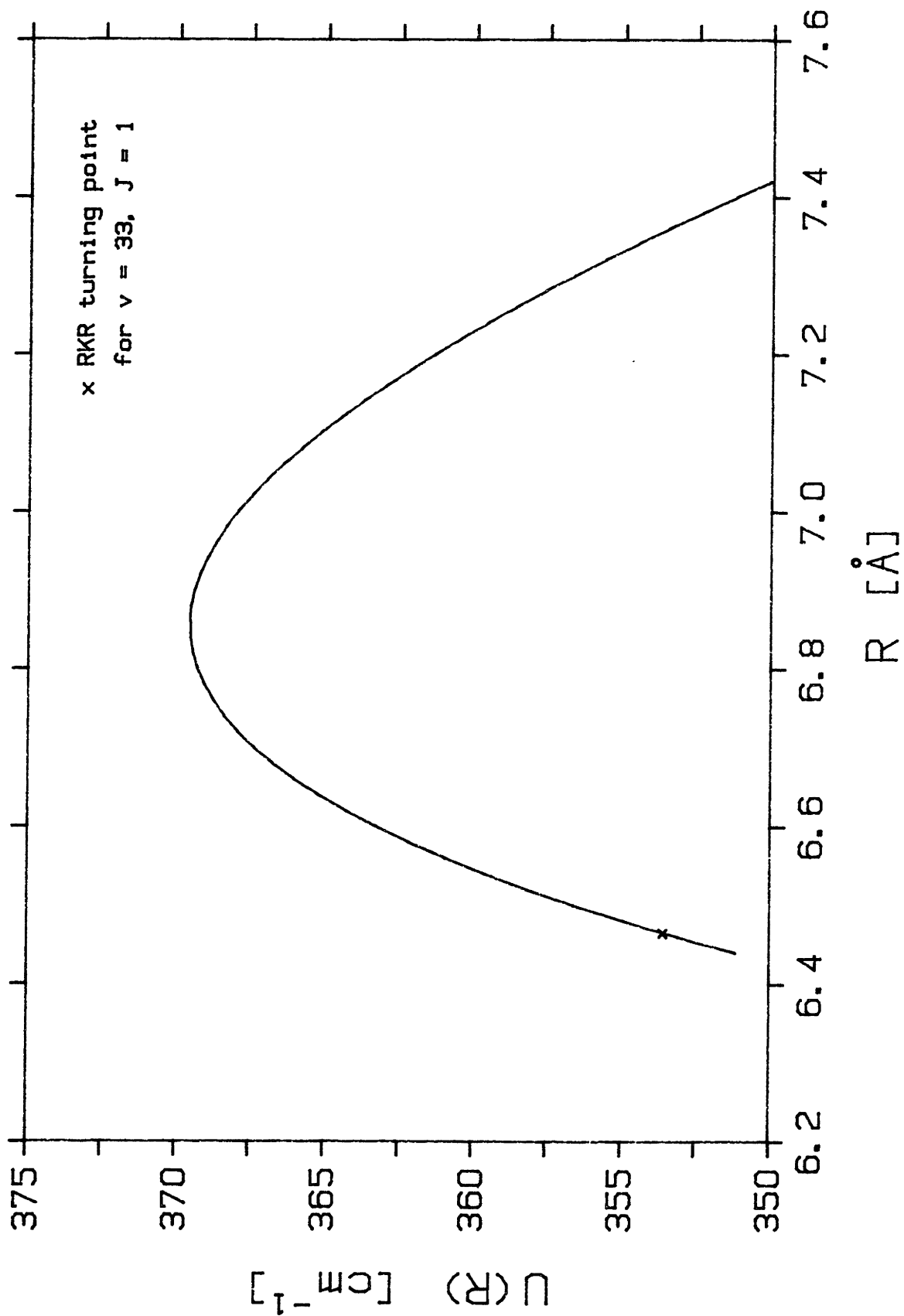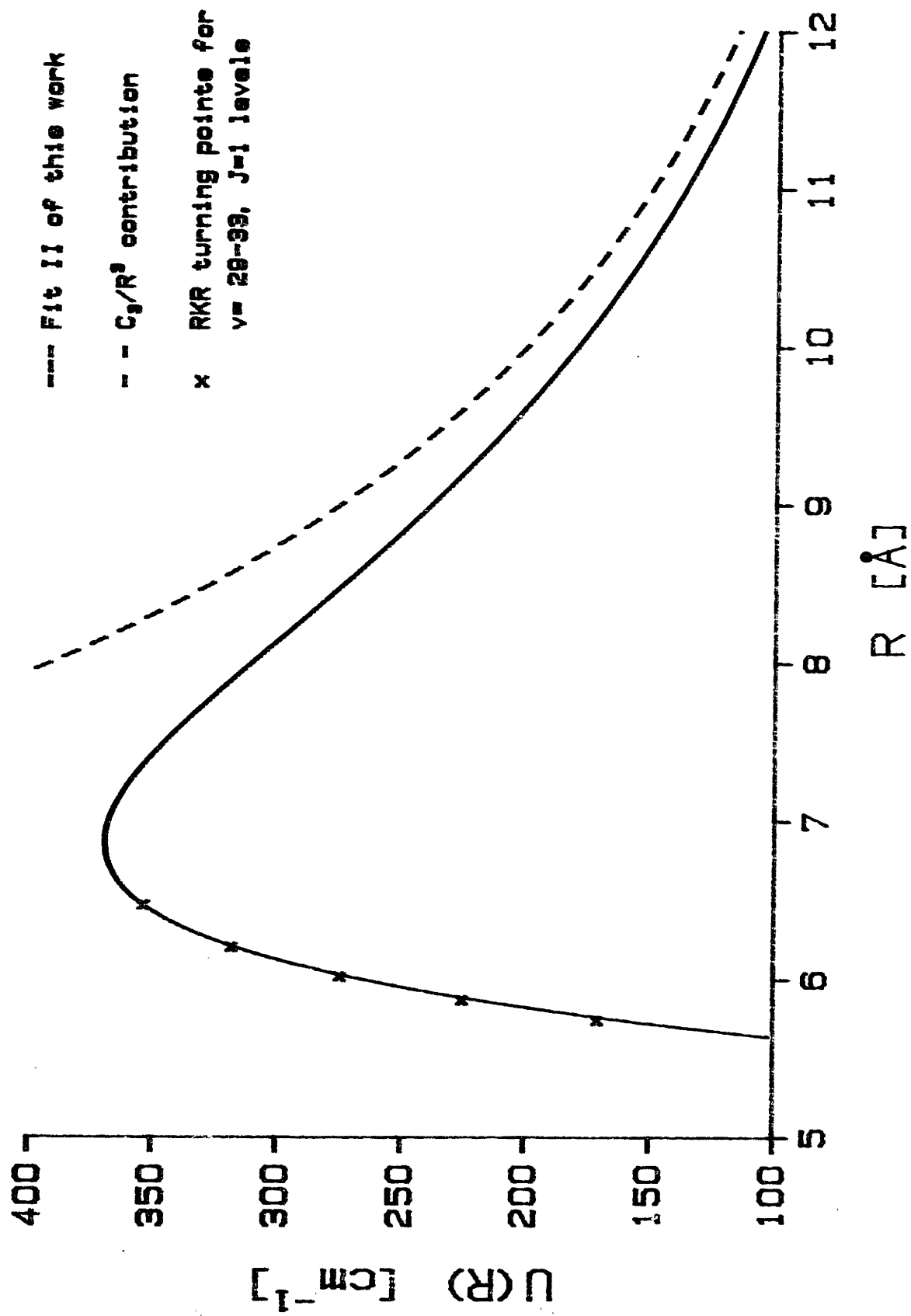
TABLE 4.6 B state potential barrier parameters (C_3, A, B) obtained by using
Equation 4.25, and comparison of the resulting barrier height
and position with previous works. In Fits I and II of this
work, D_e=22990.247 cm^{-1}, C_6=-1.286x10^7 cm^{-1} Å^6 and C_8=5.988x10^7
cm^{-1} Å^8.

	$C_3 \times 10^5$ (cm^{-1})	$A \times 10^5$ (cm^{-1})	B(Å^{-1})	U_m(cm^{-1})	r_m(Å)
Fit I	1.825(72)	-269(57)	1.861(35)	372(19)	
Fit II	2.0057	-11.01(19)	1.313(27)	369.5(3.9)	6.85
Stwalley[44]				410	6.98
Konowalow and Rosenkrantz[43]	2.23	-8.87	1.37	518	6.40
Kusch and Hessel[14]				480	-
Demtroder and Stock[13b]				554(120)	-

4.7 Alternate Method for Determining the Barrier Maximum

The determination of the barrier height in the previous section is very much dependent on the assumed functional form of the barrier in Equation (4.25). Fortunately, there is an alternate method for obtaining the barrier height which does not require us to assume a functional form for the barrier and thus allows for a self-consistency check on our earlier results.

Starting from Equation (4.18), we see that when $U(r,J) = E(v,J)$ (i.e., the barrier maximum), the phase integral is zero. If we rearrange Equation (4.17) such that the phase integral is a function of the observed lifetimes,

$$\Phi = \frac{1}{2} \ln(-1+1/P) = \frac{1}{2} \ln(-1+\omega\tau)$$

then we can plot Φ vs. E (since ω and τ are known from the experiment). The intercept of this curve with the energy axis gives us the barrier maximum.

Near the top of the barrier, the phase integral should vary linearly with E; therefore, a linear extrapolation to the intercept can be used. The linear dependence of Φ on E can easily be shown. In the region near the maximum (of height E_0 and location r_0), the potential can be expanded in a Taylor series, as in Equation (4.19), and approximated by the first three terms to give an inverted parabolic barrier,

$$U(r) = E_0 - a(r-r_0)^2 \tag{4.27}$$

where

$$E_0 = U(r_0); \quad a = -\frac{1}{2} \frac{\partial^2 U}{\partial r^2} \bigg|_{r=r_0}$$

Let us evaluate the phase integral of an energy level E through this barrier:

$$\phi \propto \int_{r_1}^{r_2} [E_0 - a(r-r_0)^2 - E]^{1/2} \, dr \qquad (4.28)$$

where

$$r_1 = r_0 - \left[\frac{E_0-E}{a}\right]^{1/2} \; ; \; r_2 = r_0 + \left[\frac{E_0-E}{a}\right]^{1/2}$$

If we make the following change of variables,

$$x = r-r_0; \quad B^2 = \frac{E_0-E}{a}$$

then Equation (4.28) becomes

$$\phi \propto \sqrt{a} \int_{-B}^{+B} [B^2-x^2]^{1/2} \, dx$$

$$\phi \propto (a)^{1/2}\left\{- \frac{x}{2}(B^2-x^2)^{1/2} + \frac{B^2}{2} \sin^{-1}\left(\frac{x}{B}\right)\right\} \Bigg|_{-B}^{+B}$$

$$\phi \propto (a)^{1/2} \frac{B^2}{2} \pi = \frac{(E_0-E)\pi}{2(a)^{1/2}} \qquad , \qquad (4.29)$$

or the phase integral varies linearly with E.

This is not a surprising result since in the analogous problem of a parabolic potential well, the same phase integral appears (except for a factor of i), and it also varies linearly with E, as shown below. If we combine

$$E \simeq E_0 + \hbar\omega(v+1/2) \qquad \text{(for low v)}$$

with the Bohr-Sommerfeld quantization condition,

$$2\phi \propto \int_{r_1}^{r_2} [(E-U)]^{1/2} \, dr \propto h(v+1/2)$$

we have

$$\Phi \propto (\frac{h}{2})(\frac{E-E_0}{h\omega}) \propto \frac{(E-E_0)\pi}{\omega} \qquad . \qquad (4.30)$$

Note the very similar forms of Equations (4.29) and (4.30). (Recall that $a \propto \omega^2$ from Equation (4.27)).

Let us now return to the problem of finding the barrier maximum. A linear least-square fit of the phase integrals for the v=33, J=3-17 data as a function of energy is shown in Figure 4.9; an extrapolation to the intercept of the energy axis determines the barrier maximum to be 397.09 cm^{-1}.

What this maximum actually corresponds to is the height of the effective potential barrier for that value of J* where E(J*)=U(J*). In order to extract a rotationless barrier maximum, one must know J* and the value of r at the maximum, since

$$E(J^*) = U_{max}(J^*) \cong U_{max}(J=1) + \frac{\hbar^2}{2\mu r^2_{max}} [J^*(J^*+1)-1] \quad .$$

We know E(J*) = 397.09 cm^{-1} from Figure 4.9; thus J* can be determined from the parameters of Table 4.2; it is equal to 25.8. Unfortunately, we must assume a location for the barrier maximum, r_{max} (which we can do from the analysis of Section 4.6). We then get the height of the J=1 barrier maximum to be 375.5 cm^{-1}. This result is within 6 cm^{-1} of the previous result and thus provides us with an almost independent and satisfactory verification of the earlier results.

Figure 4.9 Phase integrals for the J=3-17 levels as a function of the
rotational energy. Extrapolation to the energy intercept
gives an <u>effective</u> barrier maximum U(J*)=37.74 cm^{-1} (or
379.09 cm^{-1} relative to the 3s + 3p atomic limit).

$$\phi(J) = 2.267 - 0.6006\ E(J)$$
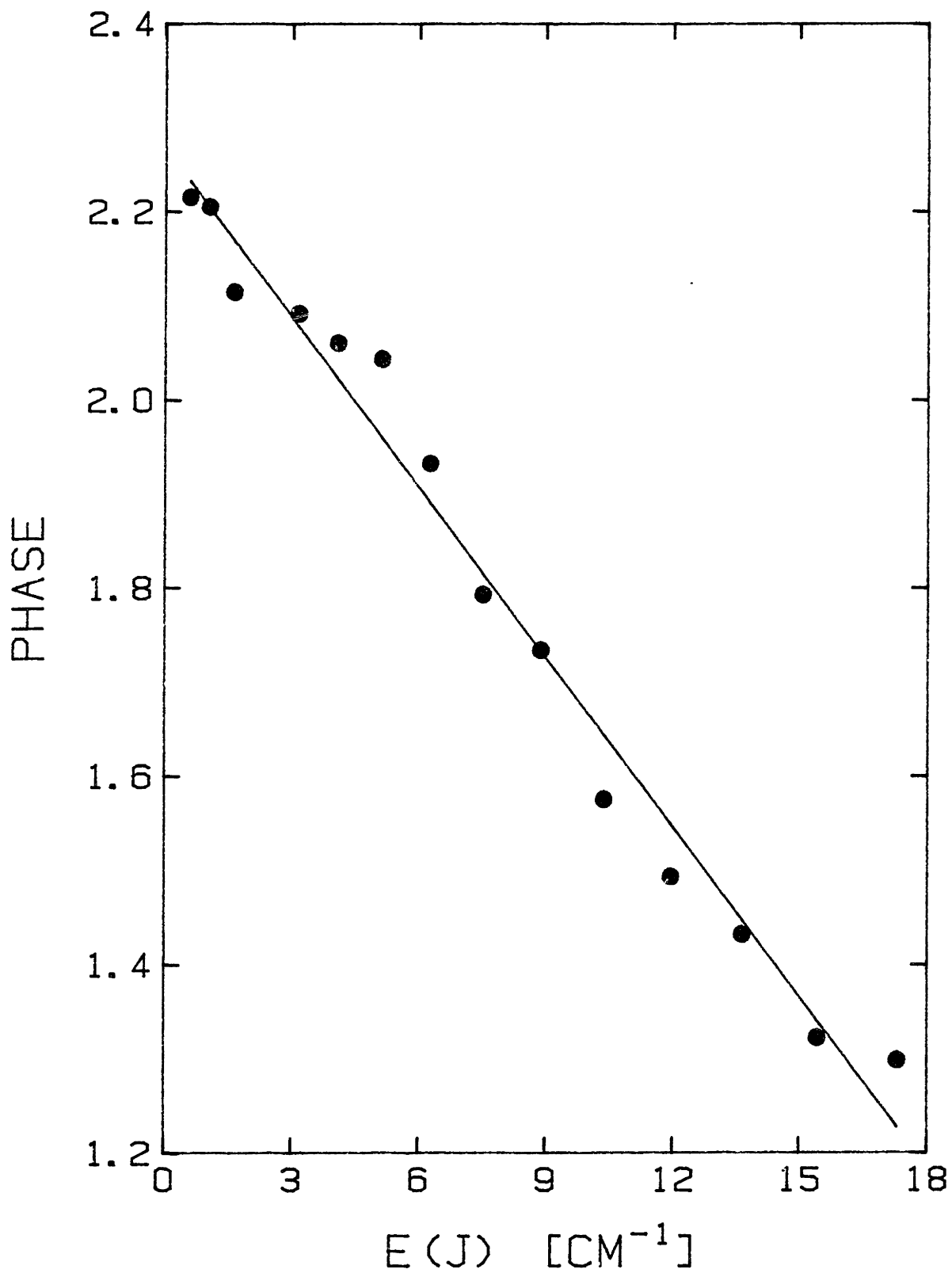
CHAPTER FIVE

THE Na$_2$ A $^1\Sigma_u^+$ STATE

5.1 Introduction

The Na_2 A $^1\Sigma_u^+$ electronic state is characterized by a very

attractive, $-2C_3/R^3$, long range potential. As depicted in Table 3.2,

this behavior arises because the transition dipole moments in the

separated sodium atoms must lie parallel to each other and along the axis

of approach when the atoms combine to form this molecular state. By

virtue of the slow R variation of the long range potential, the A state

is expected to support over 200 vibrational levels, with half of these

located ~300 cm^{-1} below the dissociation limit. Previous spectroscopic

investigations[15,16] of the A state extend up to v=44, or 54% of the

potential well depth. We began our study with the highest of these

observed levels.

5.2 Presentation of Data

PUMP-OPL-PROBE excitation schemes similar to those shown for the

B $^1\Pi_u$ state [Equation (4.1)] were used to study different sets of

vibrational levels in the A state. The MGS spectrum consisted of a simple

vibrational progression with approximately equally intense P(11), R(11)

doublets per vibrational band, as is characteristic of a parallel band

system involving singlet states. The energies of the observed levels in

the range , v = 43-105, are listed in Table 5.1.

Rapidly decreasing Franck-Condon factors for the A←X transitions,

with increasing v', limited the accessibility of the highest observed

vibrational level to v' = 105. This cutoff in v' is to be expected since

the largest contribution to the highest v' A-X Franck-Condon factors

comes from vibrational overlap at the inner turning points. The

dominance of the contribution from the inner turning point can be easily

TABLE 5.1 Observed energies (in cm^{-1}) for the J=10,12 levels of v=43-105 in the A $^1\Sigma_u^+$ state.

v = 43	J = 10	E(v,J) = 19 126.6750	v = 76	J = 10	E(v,J) = 21 529.8608
v = 44	J = 10	E(v,J) = 19 212.8600		J = 12	E(v,J) = 21 532.7956
	J = 12	E(v,J) = 19 216.8420	v = 77	J = 10	E(v,J) = 21 586.1511
v = 45	J = 10	E(v,J) = 19 298.1780		J = 12	E(v,J) = 21 589.0415
	J = 12	E(v,J) = 19 302.1530	v = 78	J = 10	E(v,J) = 21 641.2848
v = 49	J = 10	E(v,J) = 19 632.4660		J = 12	E(v,J) = 21 644.1336
	J = 12	E(v,J) = 19 636.3310	v = 79	J = 10	E(v,J) = 21 695.2224
v = 50	J = 10	E(v,J) = 19 713.9400		J = 12	E(v,J) = 21 698.0184
	J = 12	E(v,J) = 19 717.7590	v = 80	J = 10	E(v,J) = 21 747.9282
v = 52	J = 10	E(v,J) = 19 874.8060		J = 12	E(v,J) = 21 750.7045
	J = 12	E(v,J) = 19 878.5644	v = 81	J = 10	E(v,J) = 21 799.4150
v = 53	J = 10	E(v,J) = 19 954.0863		J = 12	E(v,J) = 21 802.1456
	J = 12	E(v,J) = 19 957.7895	v = 83	J = 10	E(v,J) = 21 898.6177
v = 54	J = 10	E(v,J) = 20 032.3914		J = 12	E(v,J) = 21 901.2475
	J = 12	E(v,J) = 20 036.1039	v = 84	J = 10	E(v,J) = 21 946.2739
v = 55	J = 10	E(v,J) = 20 110.0668		J = 12	E(v,J) = 21 948.8590
	J = 12	E(v,J) = 20 113.7305	v = 85	J = 10	E(v,J) = 21 992.6401
v = 56	J = 10	E(v,J) = 20 186.8546		J = 12	E(v,J) = 21 995.1722
	J = 12	E(v,J) = 20 190.5671	v = 86	J = 12	E(v,J) = 22 040.1632
v = 61	J = 10	E(v,J) = 20 558.0470	v = 87	J = 10	E(v,J) = 22 081.3725
	J = 12	E(v,J) = 20 561.5330		J = 12	E(v,J) = 22 083.7837
v = 62	J = 10	E(v,J) = 20 629.6504	v = 88	J = 10	E(v,J) = 22 123.7127
	J = 12	E(v,J) = 20 633.1058		J = 12	E(v,J) = 22 126.0699
v = 63	J = 10	E(v,J) = 20 700.5077	v = 89	J = 10	E(v,J) = 22 164.6899
	J = 12	E(v,J) = 20 703.7076		J = 12	E(v,J) = 22 166.9977
v = 64	J = 10	E(v,J) = 20 770.0797	v = 90	J = 12	E(v,J) = 22 206.5535
	J = 12	E(v,J) = 20 773.4714	v = 94	J = 10	E(v,J) = 22 349.0046
v = 65	J = 10	E(v,J) = 20 838.9372		J = 12	E(v,J) = 22 351.0315
	J = 12	E(v,J) = 20 842.2991	v = 95	J = 10	E(v,J) = 22 381.7584
v = 66	J = 10	E(v,J) = 20 906.8250		J = 12	E(v,J) = 22 383.7294
	J = 12	E(v,J) = 20 910.1551	v = 96	J = 10	E(v,J) = 22 413.1715
v = 67	J = 10	E(v,J) = 20 973.7761		J = 12	E(v,J) = 22 415.0874
	J = 12	E(v,J) = 20 977.0810	v = 97	J = 10	E(v,J) = 22 443.2524
v = 68	J = 10	E(v,J) = 21 039.7020		J = 12	E(v,J) = 22 445.1170
	J = 12	E(v,J) = 21 042.9503	v = 98	J = 10	E(v,J) = 22 472.0243
v = 69	J = 10	E(v,J) = 21 104.6575		J = 12	E(v,J) = 22 473.8340
	J = 12	E(v,J) = 21 107.8669	v = 99	J = 10	E(v,J) = 22 499.5112
v = 70	J = 10	E(v,J) = 21 168.5972		J = 12	E(v,J) = 22 501.2664
	J = 12	E(v,J) = 21 171.7839	v = 100	J = 10	E(v,J) = 22 525.7603
v = 71	J = 10	E(v,J) = 21 231.5020		J = 12	E(v,J) = 22 527.4555
	J = 12	E(v,J) = 21 234.6433	v = 101	J = 10	E(v,J) = 22 550.7795
v = 72	J = 10	E(v,J) = 21 293.3552		J = 12	E(v,J) = 22 552.4088
	J = 12	E(v,J) = 21 296.4590	v = 102	J = 10	E(v,J) = 22 574.6130
v = 73	J = 10	E(v,J) = 21 354.1362		J = 12	E(v,J) = 22 576.1948
	J = 12	E(v,J) = 21 357.1912	v = 103	J = 10	E(v,J) = 22 597.3037
v = 74	J = 10	E(v,J) = 21 413.8223		J = 12	E(v,J) = 22 598.8516
	J = 12	E(v,J) = 21 416.8503	v = 104	J = 10	E(v,J) = 22 618.8827
v = 75	J = 10	E(v,J) = 21 472.4027		J = 12	E(v,J) = 22 620.3722
	J = 12	E(v,J) = 21 475.3891	v = 105	J = 10	E(v,J) = 22 639.4021

understood when one realizes that the equilibrium internuclear distance for the A and X states are comparable (R_e' ~ 3.6Å vs. R_e'' ~ 3.1Å) whereas the outer potential walls for the two states are markedly different, with the ground state's long range potential rising more steeply towards the dissociation limit in comparison to the A state. It is a general restriction that for an R^{-6} lower state (correlating with the Na 3s + Na 3s limit) and an attractive R^{-3} upper state (correlating with the Na 3s + Na 3p limit), the high-v access will always be via the inner turning points. A complete study of the A state long range potential would require accessing the state via its outer turning point, where the probability density of the vibrational wave function is a maximum. Transitions via the outer turning point are possible only in emission from higher lying excited states, which can also have slowly varying long range potentials. This approach has been utilized by Barrow, et al.[52] in studying the long range potential of the (1) $^1\Pi_g$ state (which correlates with the Na 3s + Na 3p limit and, therefore, also possesses an R^{-3} outer limb like the A state). Their experiment involved exciting the (2) $^1\Sigma_u^+$ ← X $^1\Sigma_g^+$ transition, via the inner turning point, as illustrated in Figure 5.1. The upper state (2) $^1\Sigma_u^+$ possesses a double minimum arising from an avoided curve crossing between the (Na$^+$ + Na$^-$) and (Na 3s + Na 4s) $^1\Sigma_u^+$ states. The long range potential of the outer well varies in a Coulombic R^{-1} manner because it correlates with the ionic limit. Therefore, emission from the outer well of the upper state on the (2) $^1\Sigma_u^+$ → (1) $^1\Pi_g$ transition, has large Franck-Condon factors to high vibrational levels of the $^1\Pi_g$ state and thus has allowed Barrow, et al. to characterize the long range potential of the $^1\Pi_g$ state up to ~15.8Å.

Figure 5.1 Excitation scheme used by Barrow, et al.[52] to access

the long range potential of the Na$_2$ (1)$^1\Pi_g$ state.

$^1\Sigma_u^+$

$^1\Pi_g$

$^1\Sigma_g^+$

Na (3s) + Na (4s)

Na (3s) + Na (3p)

Na (3s) + Na (3s)

R (AU)
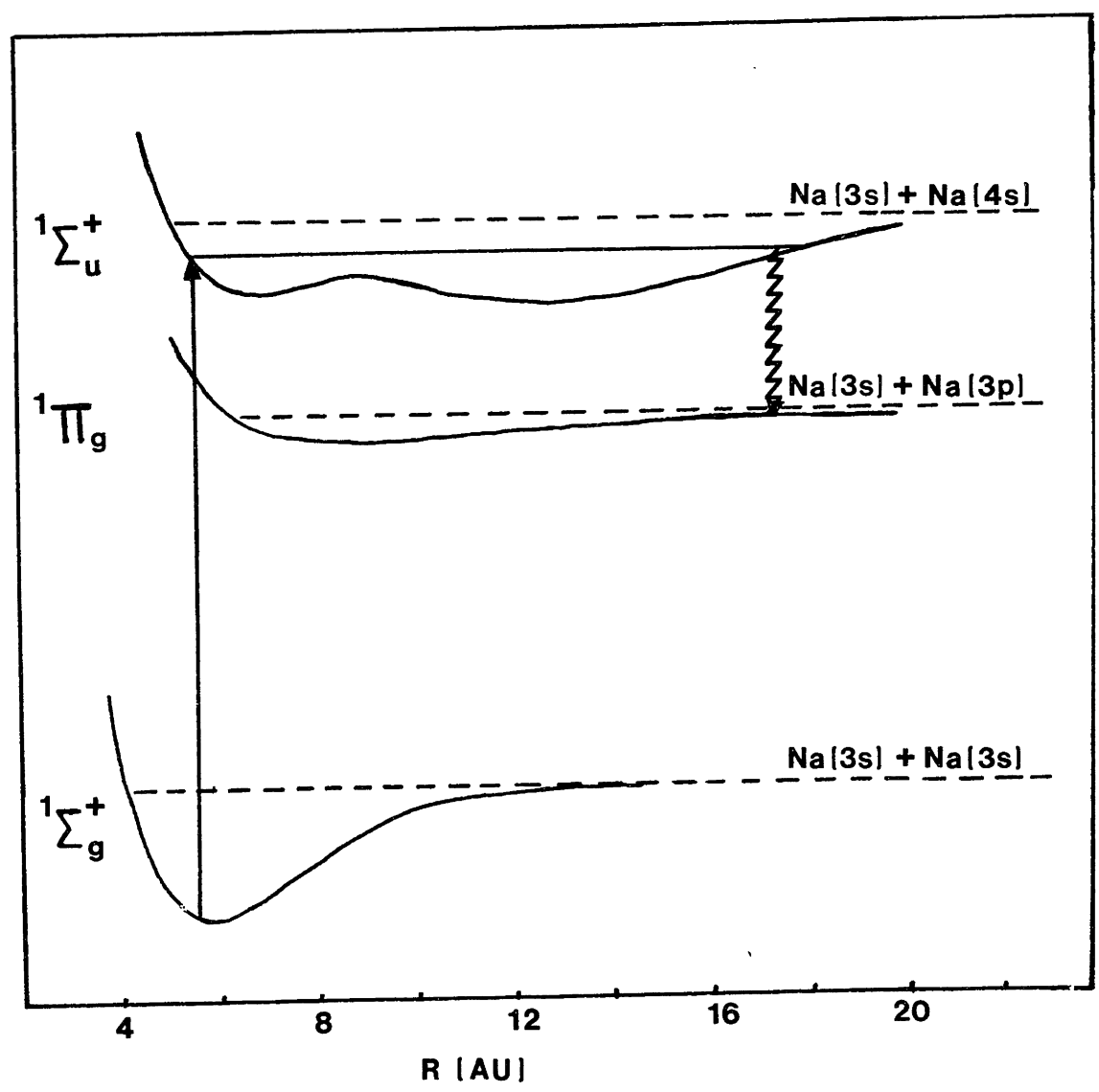
5.3 $A^1\Sigma_u^+$ State RKR Potential

A primary objective in studying the Na_2 $A^1\Sigma_u^+$ state was to obtain its complete intramolecular potential. The standard spectroscopic procedure for determining intramolecular potentials is the semi-classical, inversion method of Rydberg-Klein-Rees (RKR).[53] It relies upon a knowledge of G_v and B_v for each vibrational level spanning from v=0 up to the highest observed level. With these two properties known at each vibrational level, the following f and g integrals can be evaluated to determine the two turning points, r_1 and r_2, for each level, v',

$$f\{E(v')\} \sim \int_0^{v'} [E-G(v)]^{-1/2} \, dv \sim r_2 - r_1$$

$$g\{E(v')\} \sim \int_0^{v'} B(v)[E-G(v)]^{-1/2} \, dv \sim r_1^{-1} - r_2^{-1}$$

where r_1 and r_2 correspond respectively to the inner and outer turning points. Thus, the RKR method generates a representation of the full potential energy curve, point-by-point.

Since a smooth representation of the full (G_v, B_v) data set is required for an RKR analysis, it was necessary to merge our v=43-105 data with the previous works of Kaminsky[16] for v=19-44, and Kusch and Hessel[15] for v=0-20. However, a comparison of our G_v's and B_v's for v=43 and 44 with Kaminsky's revealed some apparent inconsistencies: our G_v's were ~1.5 cm^{-1} too low while our B_v's were ~9.9x10^{-4} cm^{-1} too high.

The possibility of a misassignment on our part of either the vibrational or rotational quantum numbers seems highly unlikely. The

(v,J) identity of the lower state in the MGS probe transition was firmly established from the measured PUMP and OPL frequencies. Therefore, the frequency of the PROBE laser unambiguously determined the final state's v and J assignment.

The discrepancy between our data and Kaminsky's prompted us to redetermine the G_v's and B_v's for the v=19-44 range from Kaminsky's observed A-X frequencies[54]. This involved determining a new set of Dunham polynomial coefficients, obtained by a least squares fit to the following energies:

(a) v=0-20, J=0,3,5,7,10,...,80, (33 rotational levels per v) as calculated from Kusch and Hessel's molecular constants,[15]

(b) v=19-35, J=42 and 44
=40-44, J=42 and 44 } as measured by Kaminsky.
=22-30, J=12 and 14

With 10 coefficients $\{Y_{10}-Y_{40}, Y_{01}-Y_{31}, Y_{02}, Y_{03}\}$, we obtained a new set of Dunham coefficients from those of Kaminsky. The resulting RKR potential does not have the G_v and B_v inconsistencies at v'=43 and 44 mentioned above.

Our first attempt at combining the above data sets a) and b) with our observed data involved generating Dunham coefficients by a fit to data sets (a) and (b) and our v=43-68, J=10 and J=12 only. With 12 coefficients $\{Y_{10-50}, Y_{01-41}, Y_{02}, Y_{03}\}$ we were able to uniformly describe this data set with a reasonable standard deviation of ~0.027 cm^{-1}; these coefficients are shown in Table 5.2.

It was not possible to represent a larger range of vibrational-rotational data than v=0-68 by one set of Dunham coefficients. To achieve a smooth representation of the full range of data, we took the following series of steps.

First, for <u>our</u> <u>data</u>, the vibrational and rotational parts of $E(v,J)$ were separated by subtracting $\{B_v J(J+1) + D_v[J(J+1)]^2\}$ from $E(v,J)$. The B_v values were determined from PR combination differences, with $D_e = 3.8 \times 10^{-7}$ cm^{-1} and $Y_{12} = 4 \times 10^{-9}$ cm^{-1}; these were then fit to a sixth order polynomial. The fitted B_v values were used to determine the vibrational energies, G_v, in order to avoid transferring the "experimental noise" of B_v's to the vibrational energies. It became important to account for the v-dependence of the centrifugal distortion, Y_{12}, especially for the higher v' levels. Neglecting the Y_{12} results in too low $B_{v'}$ values for the higher vibrational levels which, in turn, causes the inner wall of the resulting RKR potential to bend towards larger R. The estimated value of Y_{12} is based upon the ratio Y_{02}/Y_{12} from the X and B states of Na$_2$. (It can be verified once the final potential is constructed.)

Second, the resulting $B_{v'}$ and $G_{v'}$ sets for our data are merged with the lower v' data to form a complete set running from v'=0-105. For vibrational levels lower than v'=43, the $G_{v'}$ and $B_{v'}$ values are obtained from the calculated Dunham coefficients described previously. To assure a smooth merge of these two parts (v'$\leq$43, v'$\geq$43), a spline program is used. Third, the spline coefficients for v'=0-105 are then used to generate the RKR potential curve of Table 5.3 and Figure 5.2. The convergence criterion for the f and g integrals was set at 10^{-6}.

The potential curve was tested by numerically solving the radial Schrödinger equation for the eigenvalues. The calculated energies agree satisfactorily with the observed energies, for the v'=43-105 J=10 and 12 levels, to ~0.03 cm^{-1}.

TABLE 5.2 The Y_{ik} Dunham coefficients of polynomials in $(v+1/2)^i$ and $[J(J+1)]^k$ obtained from the v=0-68 combined data set of the A state.

k \ i	0	1	2	3	4	5
0	0.14680581×10^5	0.11732744×10^3	-0.35980180	0.23706855×10^{-3}	0.13393322×10^{-5}	-0.68096715×10^{-7}
1	0.11077173	-0.54474535×10^{-3}	-0.33128531×10^{-6}	0.32935142×10^{-7}	0.60533290×10^{-9}	
2	-0.38680735×10^{-6}					
3	0.10055540×10^{-11}					

Figure 5.2 Intermolecular potential of the Na_2 $A^1\Sigma_u^+$ state, from the
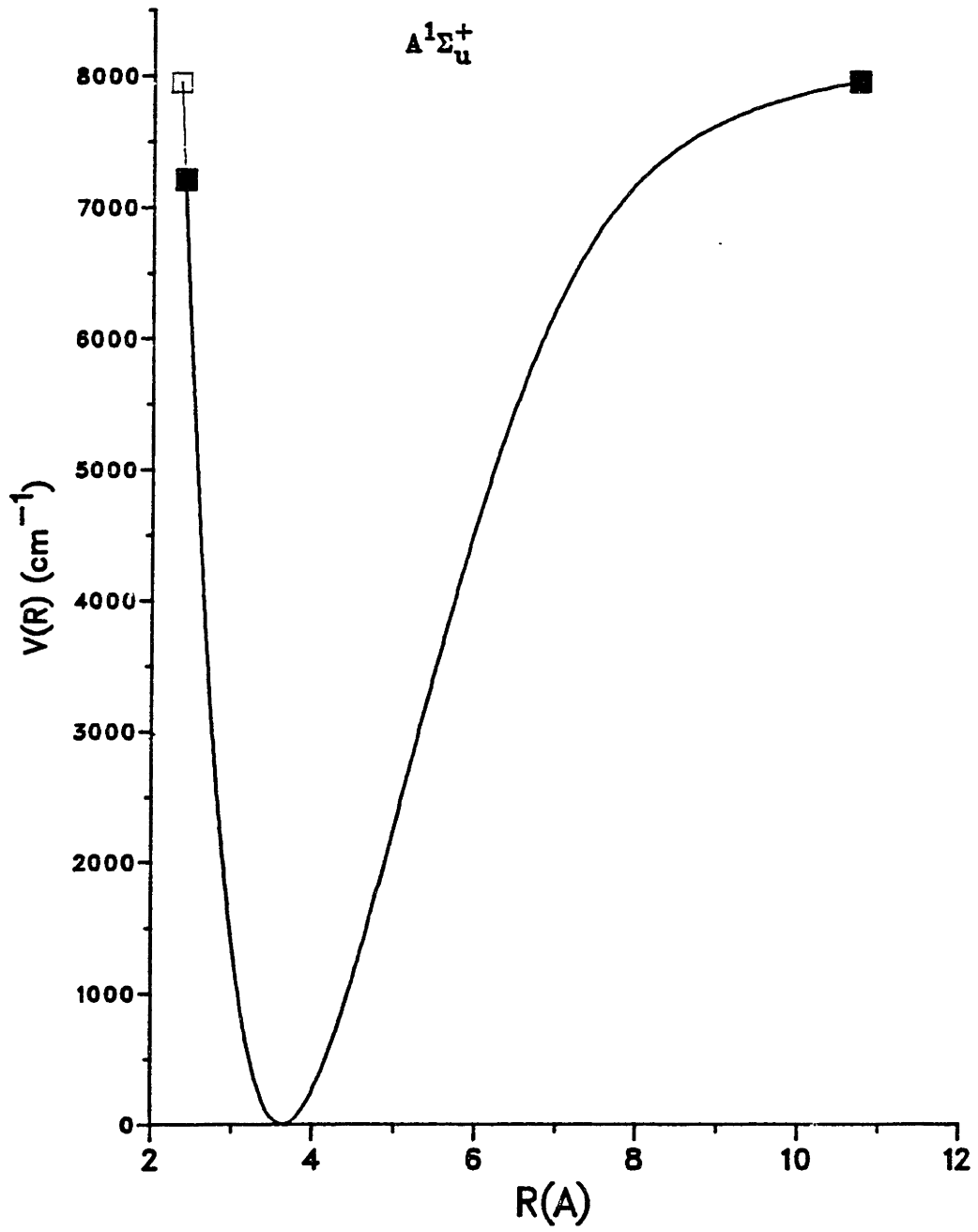
RKR-determined turning points of the v=0-105 levels.

TABLE 5.3 RKR potential for the Na$_2$ A$^1\Sigma_u^+$ state.

V	EV	GV + YOO	DELTA GV	RMIN	RMAX
0	0.1104993	58.5805	116.6086	3.4867726	3.8033094
1	0.1099540	175.1897	115.6912	3.3830201	3.9326831
2	0.1094065	291.0803	115.1752	3.3151061	4.0207498
3	0.1088624	406.2555	114.4607	3.2616661	4.1000674
4	0.1083164	520.7162	113.7477	3.2172267	4.1709648
5	0.1077705	634.4639	113.0362	3.1763892	4.2421627
6	0.1072249	747.5001	112.3262	3.1437999	4.3032890
7	0.1066795	859.8263	111.6175	3.1124923	4.3612523
8	0.1061345	971.4438	110.9104	3.0838150	4.4167238
9	0.1055901	1082.3542	110.2045	3.0573048	4.4701665
10	0.1050462	1192.5587	109.5001	3.0326164	4.5219241
11	0.1045029	1302.0588	108.7966	3.0094934	4.5722592
12	0.1039602	1410.8556	108.0949	2.9877236	4.6213790
13	0.1034182	1518.9505	107.3941	2.9671440	4.6694492
14	0.1028769	1626.3446	106.6943	2.9476196	4.7166061
15	0.1023363	1733.0369	105.9955	2.9290386	4.7629630
16	0.1017963	1839.0344	105.2976	2.9113075	4.8086150
17	0.1012570	1944.3320	104.6005	2.8943467	4.8536439
18	0.1007182	2048.9325	103.9042	2.8780681	4.8981198
19	0.1001795	2152.8367	103.2082	2.8624729	4.9421043
20	0.0996421	2256.0449	102.5128	2.8474496	4.9856519
21	0.0991046	2358.5577	101.8177	2.8329737	5.0288101
22	0.0985673	2460.3754	101.1227	2.8190054	5.0716223
23	0.0980301	2561.4981	100.4277	2.8055096	5.1141276
24	0.0974929	2661.9258	99.7325	2.7924555	5.1563615
25	0.0969555	2761.6583	99.0371	2.7798147	5.1983564
26	0.0964177	2860.6954	98.3411	2.7675626	5.2401422
27	0.0958795	2959.0365	97.6444	2.7556763	5.2817473
28	0.0953405	3056.6809	96.9469	2.7441356	5.3231977
29	0.0948005	3153.6278	96.2462	2.7329223	5.3645180
30	0.0942594	3249.8766	95.5483	2.7220194	5.4057320
31	0.0937170	3345.4243	94.8466	2.7114120	5.4468616
32	0.0931728	3440.2711	94.1437	2.7010661	5.4879289
33	0.0926266	3534.4146	93.4386	2.6910294	5.5289539
34	0.0920786	3627.8534	92.7312	2.6812302	5.5699575
35	0.0915278	3720.5846	92.0213	2.6716779	5.6109594
36	0.0909743	3812.6059	91.3089	2.6623636	5.6519794
37	0.0904211	3903.9148	90.5934	2.6532716	5.6930290
38	0.0898747	3994.5082	89.8746	2.6443756	5.7341108
39	0.0893452	4084.3828	89.1523	2.6356279	5.7751981
40	0.0888059	4173.5351	88.4108	2.6270445	5.8163516
41	0.0882560	4261.9459	87.6671	2.6186290	5.8576641
42	0.0877023	4349.6130	86.9373	2.6104017	5.8990968
43	0.0871396	4436.5503	86.2029	2.6023803	5.9406258
44	0.0865707	4522.7532	85.4631	2.5945427	5.9823107
45	0.0859960	4608.2163	84.7176	2.5868343	6.0241709

46	0.0854159	4692.9559	83.9661	2.5793961	6.0062278
47	0.0848308	4776.9000	83.2081	2.5720727	6.1085017
48	0.0842407	4860.1081	82.4432	2.5649005	6.1510126
49	0.0836457	4942.5513	81.6708	2.5578915	6.1937809
50	0.0830457	5024.2221	80.8907	2.5510212	6.2366279
51	0.0824406	5105.1126	80.1025	2.5442904	6.2801751
52	0.0818302	5185.2153	79.3056	2.5376939	6.3238447
53	0.0812142	5264.5209	78.4997	2.5312272	6.3678014
54	0.0805920	5343.0206	77.6843	2.5248858	6.4122496
55	0.0799634	5420.7049	76.8591	2.5186670	6.4570368
56	0.0793277	5497.5640	76.0236	2.5125667	6.5022493
57	0.0786844	5573.5876	75.1774	2.5065820	6.5479167
58	0.0780329	5648.7650	74.3199	2.5007142	6.5940723
59	0.0773724	5723.0849	73.4511	2.4949573	6.6407467
60	0.0767023	5796.5360	72.5702	2.4893129	6.6879746
61	0.0760219	5869.1062	71.6769	2.4837782	6.7357924
62	0.0753304	5940.7831	70.7708	2.4783539	6.7842391
63	0.0746271	6011.5539	69.8514	2.4730400	6.8333564
64	0.0739111	6081.4053	68.9185	2.4678368	6.8831858
65	0.0731817	6150.3236	67.9714	2.4627442	6.9337704
66	0.0724382	6218.2952	67.0161	2.4577057	6.9851630
67	0.0716798	6285.3113	66.0351	2.4529069	7.0373839
68	0.0709058	6351.3464	65.0391	2.4461481	7.0905703
69	0.0701154	6416.3655	64.0261	2.4435021	7.1447347
70	0.0693080	6480.4116	62.9954	2.4369671	7.1999509
71	0.0684629	6543.4070	61.9461	2.4345434	7.2562870
72	0.0676397	6605.3531	60.8775	2.4302297	7.3136197
73	0.0667776	6666.2306	59.7890	2.4260310	7.3720338
74	0.0658964	6726.0196	58.6795	2.4219391	7.4328087
75	0.0649955	6784.6991	57.5465	2.4179561	7.4944480
76	0.0640747	6842.2476	56.4002	2.4140810	7.5576416
77	0.0631336	6898.6476	55.2314	2.4103185	7.6224045
78	0.0621722	6953.8792	54.0416	2.4066648	7.6890415
79	0.0611903	7007.9210	52.8319	2.4031192	7.7574875
80	0.0601860	7060.7529	51.6017	2.3996769	7.8279211
81	0.0591654	7112.3540	50.3510	2.3963415	7.9004795
82	0.0581228	7162.7056	49.0796	2.3931048	7.9753030
83	0.0570606	7211.7654	47.7881	2.3899636	8.0525468
84	0.0559793	7259.5735	46.4761	2.3869115	8.1323920
85	0.0548794	7306.0496	45.1526	2.3839456	8.2149926
86	0.0537618	7351.2022	43.8130	2.3810729	8.3004658
87	0.0526274	7395.0152	42.4620	2.3782832	8.3890396
88	0.0514773	7437.4772	41.1020	2.3755774	8.4806665
89	0.0503127	7478.5792	39.7355	2.3729537	8.5761373
90	0.0491351	7518.3147	38.3651	2.3704106	8.6750427
91	0.0479460	7556.6798	36.9933	2.3679455	8.7777857
92	0.0467471	7593.6731	35.6225	2.3655550	8.8845800
93	0.0455405	7629.2956	34.2553	2.3632355	8.9956556
94	0.0443283	7663.5509	32.8942	2.3609664	9.1112492
95	0.0431128	7696.4451	31.5436	2.3587840	9.2316100
96	0.0418967	7727.9889	30.2113	2.3566438	9.3569527
97	0.0406826	7758.2002	28.9065	2.3545867	9.4873958
98	0.0394738	7787.1067	27.6272	2.3525711	9.6230130
99	0.0382729	7814.7339	26.3734	2.3506401	9.7640528
100	0.0370839	7841.1073	25.1452	2.3487637	9.9108283
101	0.0359103	7866.2525	23.9608	2.3469288	10.0034576
102	0.0347564	7890.2135	22.8112	2.3451459	10.2219569
103	0.0336200	7913.0245	21.7014	2.3434433	10.3859403
104	0.0325237	7934.7259	20.6306	2.3415640	10.5583768
105	0.0314542	7955.3565899999999999		2.3403440	10.7287517

5.4 Determination of C_n Coefficients using Le Roy's Method.

In addition to determining the intramolecular potential for the A $^1\Sigma_u^+$ state, we wished to determine the van der Waals coefficients characterizing the A state potential at long range. Our first attempt at extracting these coefficients from the v=95-105 subset of observed data, made use of the "deviations from the limiting near-dissociation behaviour" method developed by Le Roy.[55] This method allows a direct determination of the various C_n's from the observed vibrational and rotational constants, ω_v and B_v, without an intermediate representation of the data. Therefore, it appears to be a preferrable method of analysis when compared to the more traditional procedure for obtaining C_n coefficients from fits to RKR turning points. Furthermore, this method allows for a more reliable estimate of the C_n's with reduced correlations, as exemplified by Le Roy's application[56] to the B $^3\Pi_{0_u^+}$ state of I_2.

A. Principles

In the following section we outline some of the important points on which Le Roy's method is based. It is well known that the properties of vibrational levels lying near dissociation can be described by a potential obtained by retaining only the leading term in the long range power series expansion in $1/r$,

$$V(r) = D - C_n/r^n \tag{5.1}$$

The above single term description of the long range potential gives rise to the following, familiar Le Roy-Bernstein distributions for ω_v and B_v:[47]

$$\omega_v^\infty = K_n[D - E(v)]^{(n+2/2n)}$$

$$B_v^\infty = P_n[D - E(v)]^{2/n} \tag{5.2}$$

where K_n and P_n are functions of n, C_n, and the reduced mass, μ.

As the binding energy of vibrational levels increases, their outer turning points decrease; therefore, the higher order terms in the potential expansion begin to make substantial contributions to the overall potential energy . One important effect of the higher terms is that they modify the form of the v-dependence of ω_v and B_v from their near-dissociation limiting behavior of Equation (5.2). The parameter α is used to express the deviations from limiting behavior. α is the ratio of the contributions made by the higher terms relative to that of the leading term in the long range expansion,

$$V(r) = D - C_n/r^n - C_m/r^m, \qquad m>n$$

and
$$\tag{5.3}$$
$$\alpha \equiv \frac{C_m/r_2^m}{C_n/r_2^n}$$

where r_2 is the outer turning point. The deviations of observed ω_v and B_v from limiting behavior correspond to a unique variation of the α's (this is shown below). Once this variation of α is extracted, one obtains the desired magnitudes of the C coefficients.

Figure 5.3 demonstrates how the deviations of the ω_v's and B_v's from asymptotic behaviour can reveal the underlying C coefficients. The data points $v = 63$-80 are for the $B\ {}^3\Pi_{0_u^+}$ state of I_2, which correlates with the $I({}^2P_{3/2}) + I({}^2P_{1/2})$ limit. The dotted horizontal line at $y=1$ represents the limit where the potential is well

Figure 5.3 For I_2 $B^3\Pi_{0_u^+}$ state, a comparison of the experimental ω_v/ω_v^∞ and B_v/B_v^∞ values (large dots) with the predictions made by various representations of the long range potential:

....   (5)

---   (5,6)

— —   (5,6,8)

—.—.—.   (5,6,8,10)

From Le Roy.[55]

$$\frac{\omega_v}{\omega_v^\infty}$$

$$\frac{B_v}{B_v^\infty}$$

$$\{[D-G(v)]/cm^{-1}\}^{3/10}$$
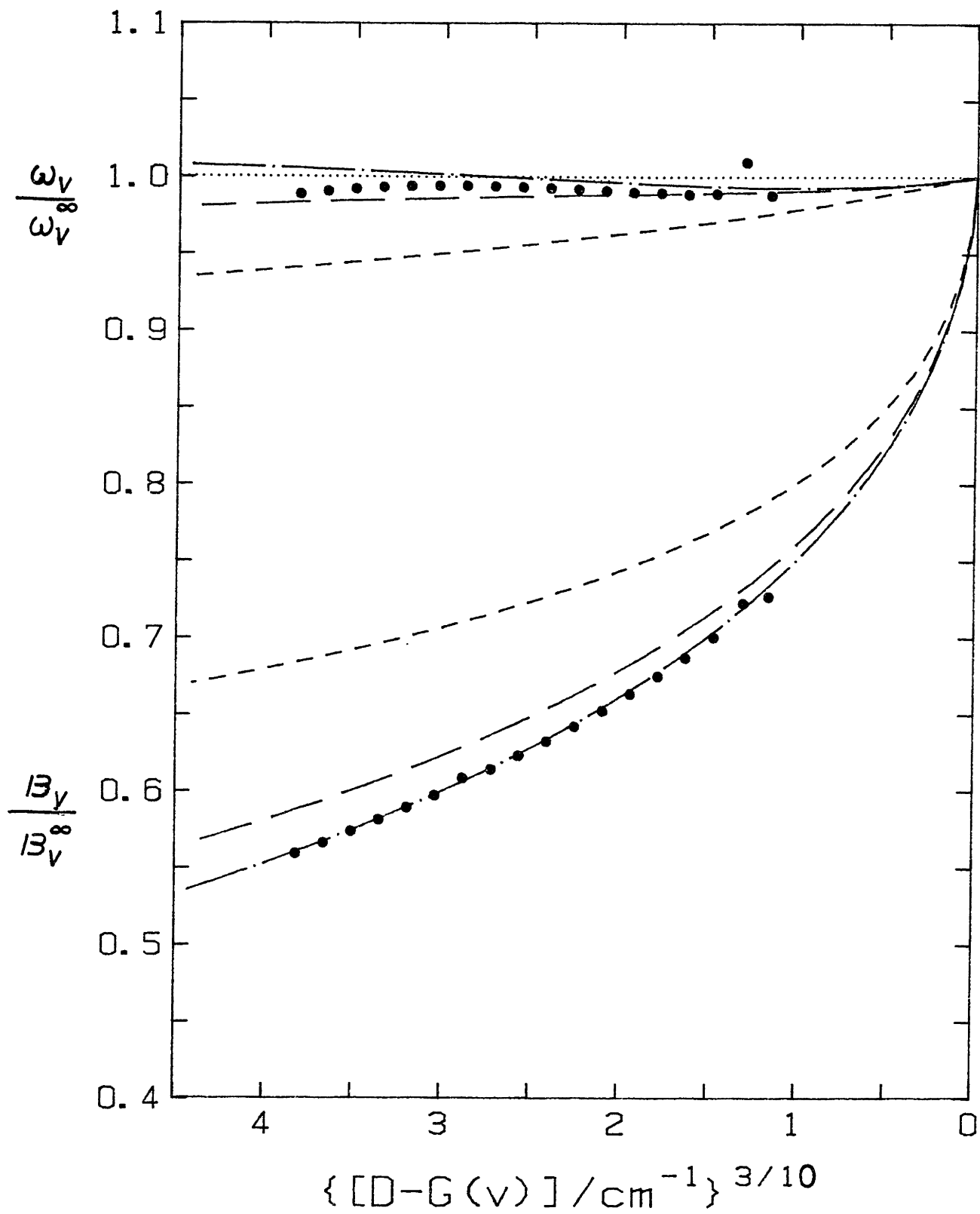
characterized by the leading C_5 r^{-5} term alone; the corresponding

limiting ω_V and B_V values are denoted ω_V^∞ and B_V^∞. Contributions by the

$C_6 r^{-6}$ term cause a negative deviation from limiting behavior for both the

ω_V and B_V data set, with a substantially larger effect on the B_V's.

Inclusion of $C_8 r^{-8}$ and $C_{10} r^{-10}$ terms influence the ω_V's and B_V's in

opposite directions and by varying amounts. Since the various C

coefficients affect ω_V and B_V in qualitatively very different ways, one

would expect a simultaneous fit of the (ω_V, B_V) data to be a sensitive

method by which to optimally separate the contributions of each term and

thereby determine accurate values of these coefficients.

In order to show the transparent and straightforward nature of the

technique, let us rederive the expressions relating the different

dependence of ω_V and B_V on the parameter α. ω_V and B_V are respectively

the inverse of the vibrational and rotational density of states.

$$\omega_V \equiv \partial E/\partial v$$

$$B_V \equiv \partial E/[\partial J(J+1)] \bigg|_{J=0} = \frac{\partial v/\partial [J(J+1)]}{\partial v/\partial E} \bigg|_{J=0} \tag{5.4}$$

Using the Bohr-Sommerfeld quantization condition,

$$h(v + 1/2) = 2 \int_{r_1}^{r_2} dr \, \{2\mu[E(v) - V(r)]\}^{1/2}$$

we see that ω_V and B_V can be expressed as partial derivatives of the

above action integral through quantities $\partial v/\partial E$ and $\partial v/\partial [J(J+1)]$,

$$\partial v/\partial E = (\sqrt{2\mu}/h) \int_{r_1}^{r_2} dr\ (E-V)^{-1/2}$$

$$\partial v/\partial[J(J+1)] = (\sqrt{2\mu}/h) \int_{r_1}^{r_2} dr\ (E-V)^{-1/2} B_v \qquad (5.5)$$

where $B_v = \dfrac{\hbar^2}{2\mu} \langle r^{-2}\rangle$.

A useful and compact representation of ω_v and B_v, in terms of the integral,

$$I_\ell(E) = \int_{r_1}^{r_2} dr\ r^{-\ell}(E-V)^{-1/2} \qquad (5.6)$$

now becomes

$$\omega_v = 2\pi\beta/I_0(E)$$

$$B_v = \beta^2 I_2(E)/I_0(E) \qquad (5.7)$$

where

$$\beta = [\hbar^2/2\mu]^{1/2} \quad .$$

Examination of the integrand of Equation (5.6) shows that the largest contribution to the integral, for high vibrational levels, comes from regions of r near the turning points r_1 and r_2, where the integrand becomes singular. Furthermore, since the potential becomes increasingly anharmonic as the energies increase, the contribution from r_2 dominates. These two considerations led Leroy to make the following approximations:

(i) Replace V(r) in Equation (5.6) by the long range form of the potential, and

(ii) Set $r_1 = 0$.

Implementing the first of these, V(r) is represented by the two term expression of Equation (5.3). Combining this with the following relation

$$E(v) = D - C_n/r_2^n - C_m/r_2^m$$

where r_2 is the outer turning point of the vth vibrational level, we get

$$E(v) - V(r) = \frac{C_n}{r_2^n} \left[\left(\frac{r_2}{r}\right)^n - 1\right] + \frac{C_m}{r_2^m} \left[\left(\frac{r_2}{r}\right)^m - 1\right] \qquad (5.8)$$

If we make the following substitutions into the above equation,

$$\alpha \equiv C_m/C_n (r_2)^{m-n} \quad \text{and} \quad x \equiv r/r_2$$

then Equation (5.8) transforms into

$$\left(\frac{r_2^n}{C_n}\right) [E(v)-V(r)] = (x^{-n}-1) + \alpha(x^{-m}-1)$$

Substituting this result into Equation (5.6), we get

$$I_\ell(E) = (C_n)^{-1/2} (r_2)^{1-\ell+n/2} \int_{(r_1/r_2)}^{1} dx/x^\ell \{(x^{-n}-1)+\alpha(x^{-m}-1)\}^{1/2}$$

$$(5.9)$$

Using the second approximation mentioned above and rearranging equation (5.9), we get the desired expression:

$$I_\ell(E) = \{(C_n)^{(1-\ell)/n} / [D-E]^{1/2+(1-\ell)/n}\} \, \overline{I}_\ell(\alpha)$$

where

$$\overline{I}_\ell(\alpha) = (1+\alpha)^{1/2+(1-\ell)/n} \int_0^1 dx/x^\ell \{(x^{-n}-1)+\alpha(x^{-m}-1)\}^{1/2} \qquad (5.10)$$

When $\alpha=0$, we recover the limiting, near-dissociation expressions of Equation (5.2). For example,

$$\omega_v = 2\pi\beta/I_0(E)$$

$$= \{[D-E]^{(n+2)/2n}\}\{2\pi\beta / \underbrace{(C_n)^{1/n} \, \overline{I}_{\ell=0}(\alpha=0)\}}_{K_n}$$

Figure 5.4 Courtesy of Le Roy[55].

(B)

$\ell = 2$

$\ell = 0$

(n,m)

$(3,4)$

$(4,5)$
$(3,5)$
$(5,6)$
$(4,6)$
$(3,6)$
$(6,8)$

$(3,4)$

$(3,5)$
$(3,6)$
$(4,5)$
$(4,6)$
$(5,6)$

$(6,8)$

$\bar{I}_\ell\,(a)$

1.4 1.2 1.0 0.8 0.6 0.4

0.8 0.6 0.4

0.0 0.5 1.0 1.5 2.0

$a(n,m) = c_m/c_n\,(r_2)^{m-n}$

(A)

$m = 5$
$m = 5,6$
$V(r)$

$[E(v) - V(r)]^{-1/2}$

E

r
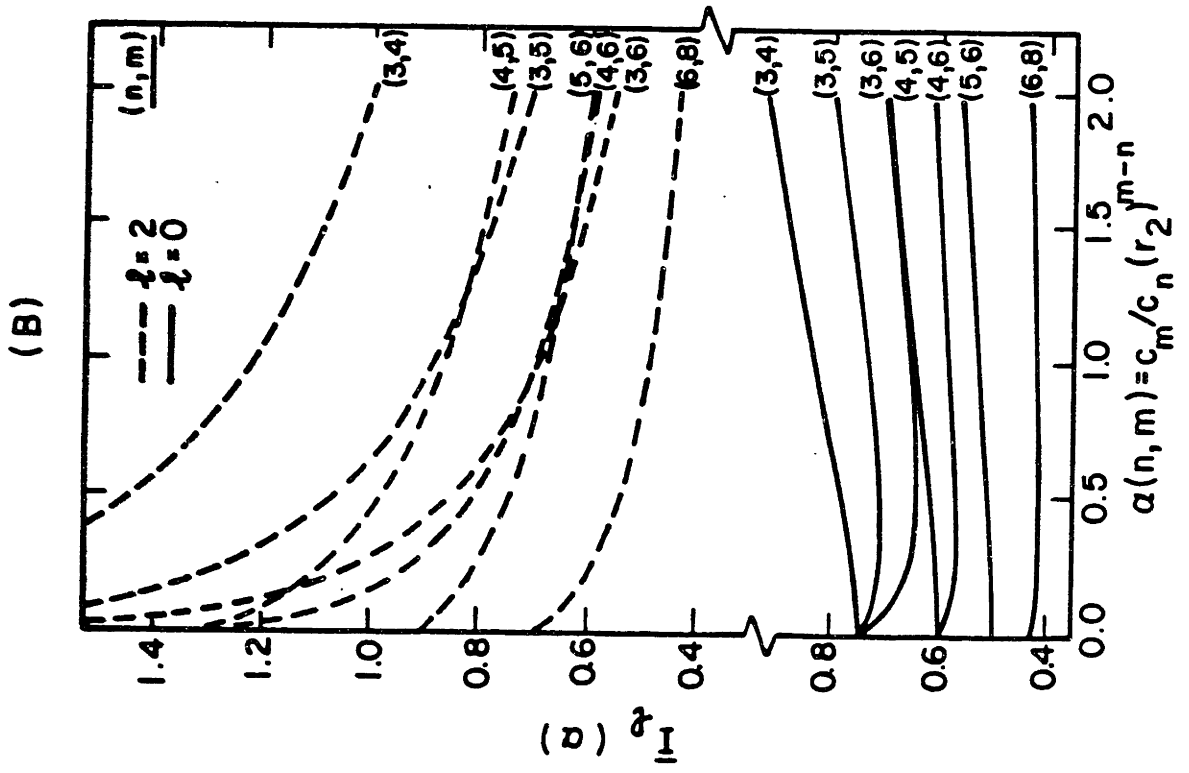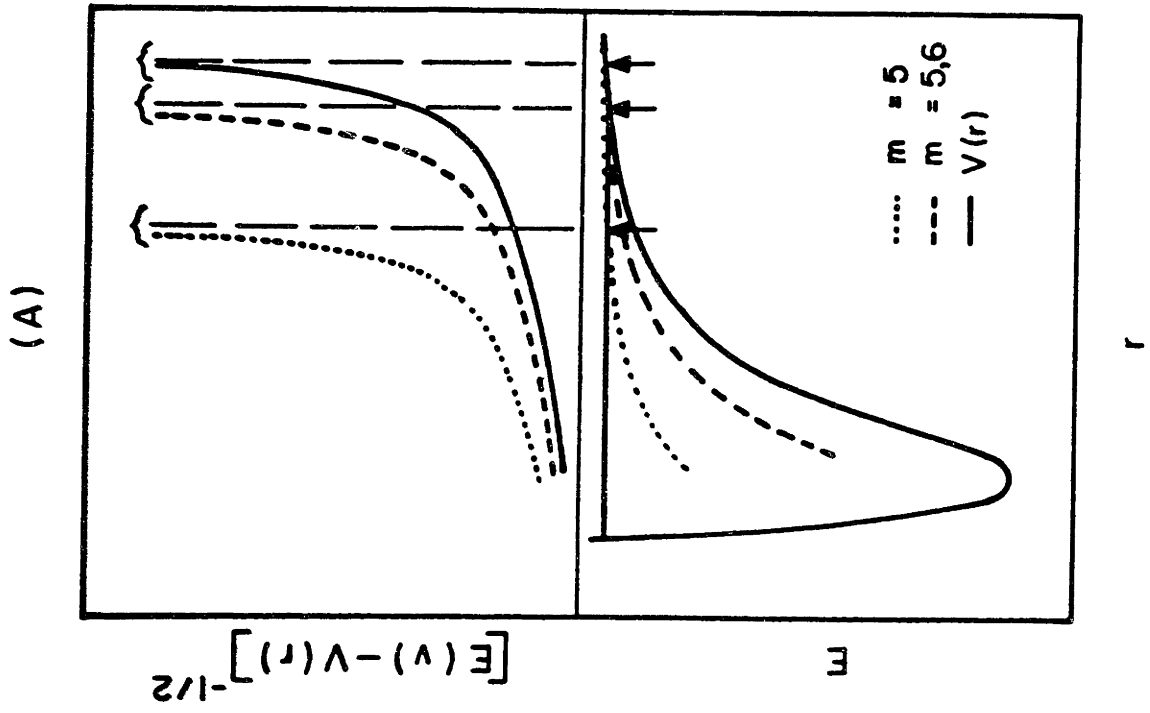
where $\overline{T}_\ell(\alpha=0)$ is a simple ratio of gamma functions in the variables ℓ and n.

Equation (5.10) reveals two different ways in which the parameter α (a measure of the relative contribution of higher order terms compared to the leading term) can affect the $\overline{T}_\ell(\alpha)$ integral (and in turn the ω_v's and B_v's). The qualitatively different dependence of ω_v and B_v on the $\overline{T}_\ell(\alpha)$ integrals is due to these two different dependences of $\overline{T}_\ell(\alpha)$ on the parameter α. Increasing the value of α causes the outer potential wall to become more steep, thereby influencing the $\overline{T}_\ell(\alpha)$ integral in the two ways shown in Figure 5.4a. First, it moves the outer turning points toward larger values of r. This has the effect of increasing the value of $\overline{T}_\ell(\alpha)$ by the multiplicative factor, $(1+\alpha)^{1/2+(1-\ell)/n}$. The second effect of the increased steepness of the outer wall is to produce a larger difference between an energy level and the potential thereby leading to a smaller integrand (or a reduced value of $\overline{T}_\ell(\alpha)$). The presence of the x^{-2} factor in the $\overline{T}_2(\alpha)$ integral "weights" these two opposing effects of $\alpha\neq0$ differently with respect to each other in the $\overline{T}_0(\alpha)$ and $\overline{T}_2(\alpha)$ cases. Figure 5.4b shows the essentially flat profiles of $\overline{T}_0(\alpha)$ vs. α, which result from an almost complete cancellation of the two effects, and the rapidly decreasing profiles of $\overline{T}_2(\alpha)$ vs. α, which result from a domination of the second effect over the first. We can now see how the ω_v's and B_v's (or the $\overline{T}_0(\alpha)$ and $\overline{T}_2(\alpha)$ integrals) provide mutually complementary information about α and, in turn, the C coefficients.

B. Application to the A $^1\Sigma_u^+$ State of Na$_2$

Le Roy has made available to us a computer program which performs nonlinear least squares fits of the observed (ω_v, B_v) data to the

dissociation energy, D, and the various C coefficients. We attempted to apply this method to the v=96-105 levels of the A state. The outer turning points for this data set ranges from 9.36Å to 10.7Å; therefore, the properties of these vibrational levels should be predictable by long range theory, which is appropriate for internuclear separations $R \gtrsim 9.2$Å.

When the long range potential is represented by the (3,6,8) three term expansion, the observed ω_V's and B_V's could not be least squares fitted, either as two independent data sets or as one combined data set. If one uses a (3,6) two term representation of the potential, one does obtain convergence. However, the resulting C_3 value is lower (by ~12%) than that value determined from the experimental oscillator strength of the Na D-lines[51], of 4.0114×10^5 cm^{-1}Å^3. The fitted C_6 value is also lower (by ~31%) than the ab initio value of Bussery[12], of 1.9969×10^7 cm^{-1} Å^6. The $\omega_V/\omega_V^{\infty}$ and B_V/B_V^{∞} values predicted by the ab initio C_6 and C_8 values are illustrated in Figure 5.5 for both the two (3,6) and three (3,6,8) term cases. The observed values of $\omega_V/\omega_V^{\infty}$ and B_V/B_V^{∞}, indicated by dots, are seen to be poorly described by either the (3,6) or (3,6,8) representation.

Our inability to extract the higher order C_m coefficients may be due to the very small relative contributions of the higher order terms to the total potential energy. Table 5.4 shows that for v = 96 the contribution made by the C_6R^{-6} term is only 6% of the C_3R^{-3} term. (Notice that this is even smaller than the 10% relative contribution of the $C_{10}R^{-10}$ term in the (5,6,8,10) potential of the B state of I_2.) Higher terms in the Na_2 potential like C_8R^{-8} or $C_{10}R^{-10}$ also make small relative contributions (like the C_6R^{-6} term); therefore, extracting these coefficients is equally difficult.

Figure 5.5 For the Na_2 A $^1\Sigma_u^+$ state, a comparison of the experimental

ω_v/ω_v^∞ and B_v/B_v^∞ values (large dots) with the predictions made

by various representations of the long range potential:

········   (3)

- - - -   (3,6)

— —   (3,6,8)

$$\frac{\omega_v}{\omega_v^\infty}$$

$$\frac{\beta_v}{\beta_v^\infty}$$
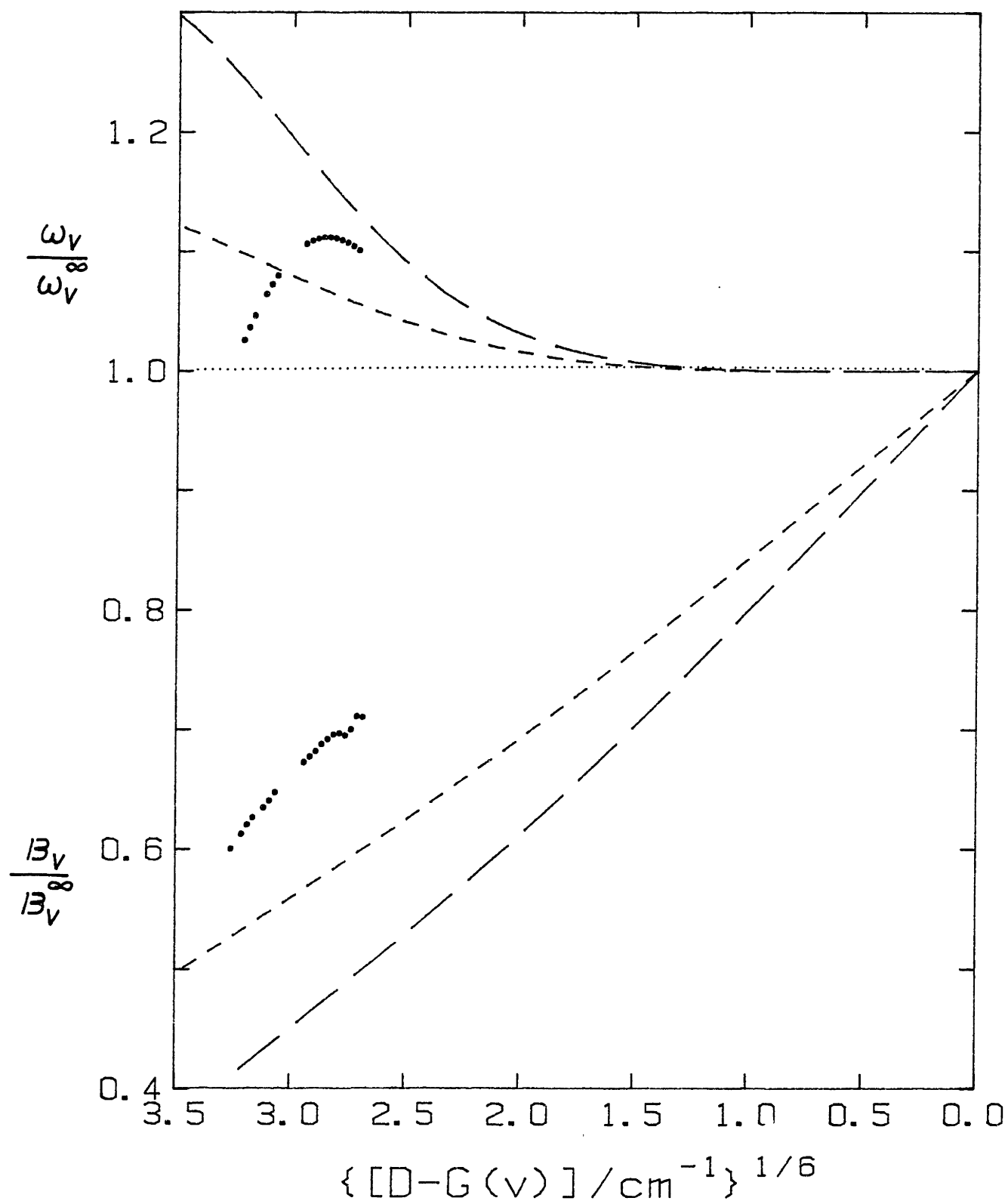
$$\{[D-G(v)]/cm^{-1}\}^{1/6}$$

TABLE 5.4 Comparison of the contributions made to the long range
potential energy by higher order R^{-n} terms relative to the
leading R^{-n} term. Relative contributions are given by the α's,
and are shown for two vibrational levels in each system.

System[a,b]	v	$r_2(v)$,Å	α_1	α_2	α_3
I_2 B $^3\Pi_{0_u^+}$	60	5.713	1.12	0.47	0.098
	80	12.29	0.52	0.047	0.0022
Na_2 A $^1\Sigma_u^+$	96	9.36	0.06	0.049	-
	103	10.4	0.044	0.029	-
H_2 B $^1\Sigma_u^+$	32	6.34	0.091	0.05	-
	38	19.9	0.003	0.0002	-

[a] For the I_2 state under consideration, long range theory is valid for $R \gtrsim$
5.5Å; for the Na_2 state shown, $R \gtrsim 9.2$Å; for the H_2 state shown, $R \gtrsim 6.6$Å.

[b] Also note that for the (5,6,8,10) potential of I_2, $\alpha_1 = C_6/C_5 r_2$,
$\alpha_2 = C_8/C_5 r_2^3$, and $\alpha_3 = C_{10}/C_5 r_2^5$; For the (3,6,8) potentials of Na_2 and
H_2, $\alpha_1 = C_6/C_3 r_2^3$ and $\alpha_2 = C_8/C_3 r^5$.

In order to test the above hypothesis, we applied Le Roy's method to the well-studied analogous state in H_2, the B $^1\Sigma_u^+$ state. Since this state correlates with the (H 1s + H 2p) limit, its long range potential is also characterized by the (3,6,8,...) expansion, like the A $^1\Sigma_u^+$ state of Na_2. Naimoka[57] has observed the high lying vibrational levels, v=32-38, of the H_2 B state which extend up to within ~1 cm^{-1} of the dissociation limit. Least squares fits of the ω_v's and B_v's for these levels showed the same symptomatic failures observed for the vibrational levels of the Na_2 A state. A (3,6,8) representation of the potential yielded converged results only for the v=35-38 subset; however, the fitted values of C_3, C_6, and C_8 were substantially smaller than the accurate ab initio values of Kolos[58] (smaller by 69%, 19%, and 97% respectively). Grossly underestimated values of C_3 and C_6 were also obtained when using a (3,6) potential representation.

For both the A state of Na_2 and the B state of H_2, the small contributions of the $C_6 R^{-6}$ and higher terms manifest themselves as small values of the parameter α. The (somewhat deceptively) large deviations of ω_v and B_v from limiting behavior appear only because the $I_\ell(\alpha)$ integrals have a very sensitive dependence on α, near $\alpha=0$, for the (3,6) case. However, the actual contributions of the higher terms are very small indeed. Therefore, we conclude that the deviations-from-limiting-behavior technique seems to be applicable primarily to those systems with (5,6,...) or (6,8,...) potentials, where the higher order terms make a substantial (perhaps 10% or more) contribution to the total potential energy of the system.

5.5   Estimation of C_n coefficients from RKR points

We attempted to obtain estimates of the C_n long range coefficients for the Na_2 $A^1\Sigma_u^+$ state from the RKR-determined potential curve of Section Three. Since the long-range potential, $U(R)$, has the asymptotic form

$$U(R) \simeq D_e + C_3/R^3 + C_6/R^6 + C_8/R^8 \qquad (5.11)$$

a plot of $R^6 \cdot [U(R)-D_e-C_3/R^3]$ versus R^{-2} should be linear with intercept C_6 and slope C_8. Figure 5.6a shows such a plot for the highest observed vibrational levels, $v=95-105$, whose outer turning points span the range $R \sim 9.2-10.7$Å. Although the plot shows reasonably linear behavior for the last six levels, it gives the physically unreasonable result of a positive C_6 coefficient, $C_6 \sim +5.36 \times 10^7$ cm^{-1}Å^6. A positive C_6 would arise from an overestimated slope (i.e. too large C_8 coefficient).

The contributions made by each R^{-n} term of Equation (5.11), based on <u>ab initio</u> C_6 and C_8 values of Bussery[12], are tabulated in Table 5.5. Also shown is the electron-exchange energy contribution to the potential, based on the <u>ab initio</u> A and B values of Konowalow and Rosenkrantz[43]. It is seen that the attractive exchange effects persist to surprisingly large values of R and makes contributions comparable to the attractive C_6/R^6 and C_8/R^8 terms. If the exchange contribution is subtracted from $U(R)$ and $R^6 \cdot [U(R)-D_e-C_3/R^3-A\exp(-BR)]$ is plotted versus R^{-2}, then we obtain more reasonable values of C_6 and C_8 are obtained, as shown by Figure 5.6b. The C_6 coefficient thus obtained is tenfold smaller and the C_8 coefficient threefold larger than Bussery's values. We note that these C_6 and C_8 results are essentially determined by the A and B exchange parameters and are based on the assumption that exchange contributions to the potential energy can be completely accounted for by the addition of an A exp(-BR)

term to Equation (5.11). If the exchange contributions are indeed as large as suggested by Table 5.5, then the initial assumption of separability of the C_6/R^6, C_8/R^8 and the exchange terms is of questionalbe validity.

A first attempt at extracting the C_3 coefficient from the v=95-104 data was also made by approxiamting the long range potential of Equation (5.11) by the leading C_3/R^3 term only. The resulting Le Roy-Bernstein expression

$$[\Delta E(v)]^{1.2} = (K_3)^{1.2} [D_e - E(v)]$$

where

$$K_3 = \frac{34.5429}{(\mu)^{1/2}(C_3)^{1/3}}$$

can be used to determine K_3 (and in turn the C_3 coefficient) from the observed values of $E(v)$ and $\Delta E(v)$. (Note that the C_3 coefficient in the above expression was implicitly assumed to be negative.) From the plot of Figure 5.7 we obtained a $C_3 = -2.80 \times 10^5$ cm^{-1} Å^3, which is 30% smaller than the accurate value of 4.0114×10^5 cm^{-1} Å^3. Evidently the long range potential of the A state cannot be reasonably approximated by the leading term in order to account for the observed data.

It appears that an extension of the A state vibrational data beyond the highest presently observed level, v=105, is needed before further manipulation of data to the end of determining C_n coefficients can be performed.

Figure 5.6   a) Plot of $R^6[U(R)-D-C_3/R^3]$ versus R^{-2} for Na_2 A state using

RKR outer turning points for $v=95-105$. The resulting

$C_6 \simeq + 5.36 \times 10^7$ cm^{-1} $Å^6$ and $C_8 \simeq -6.2 \times 10^9$ cm^{-1} $Å^8$.

b) Plot of $R^6[U(R)-D-C_3/R^3-A\exp(-BR)]$ versus R^{-2} for same

data set. The resulting $C_6 \simeq -1.50 \times 10^6$ and $C_8 \simeq -4.29 \times 10^9$

cm^{-1} $Å^8$.

B

$v = 105\ 104\ 103\ 102\ 101\ 100\ 99\ 98\ 97\ 96\ 95$

$R^6 [U(R) - D - C_3 R^{-3} - A \exp(-BR)] \times 10^{-7}$

-3.75 -4.00 -4.25 -4.50 -4.75 -5.00 -5.25

0.008 0.009 0.010 0.011 0.012

R^{-2}

A

$v = 105\ 104\ 103\ 102\ 101\ 100\ 99\ 98\ 97\ 96\ 95$

$R^6 [U(R) - D - C_3 R^{-3}] \times 10^{-7}$

-4.0 -4.5 -5.0 -5.5 -6.0 -6.5

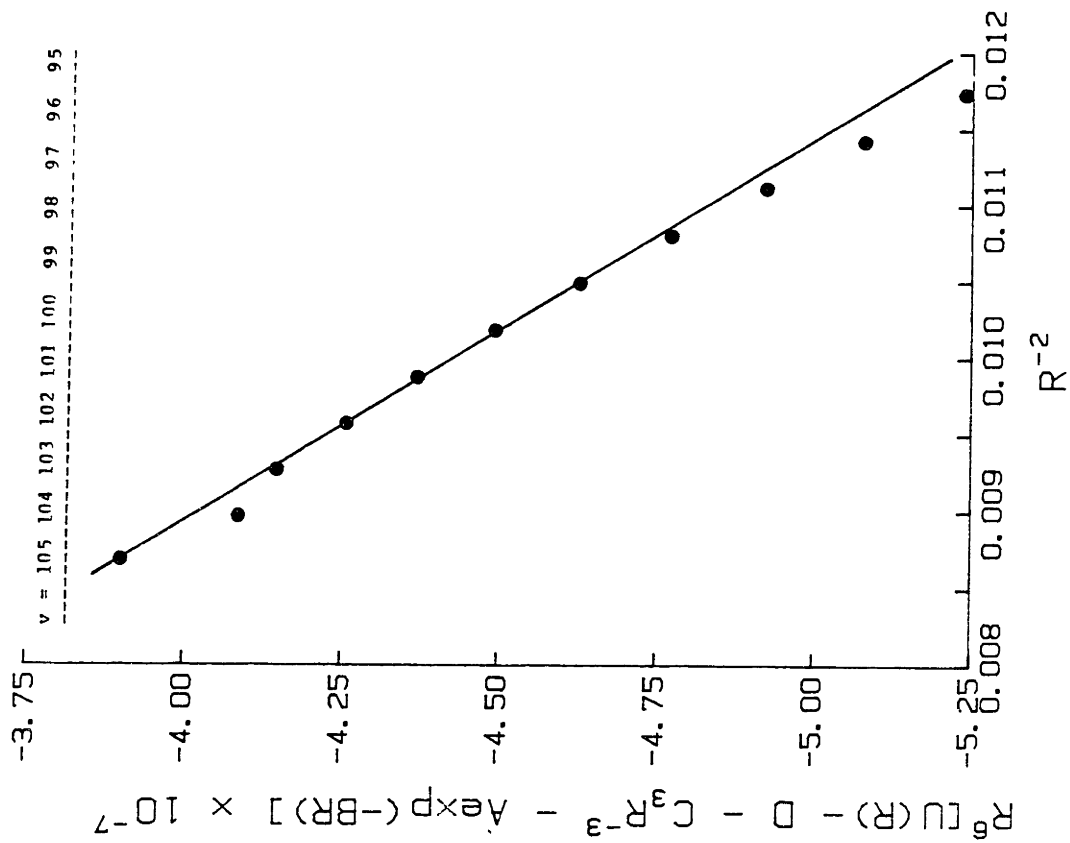0.008 0.009 0.010 0.011 0.012

R^{-2}
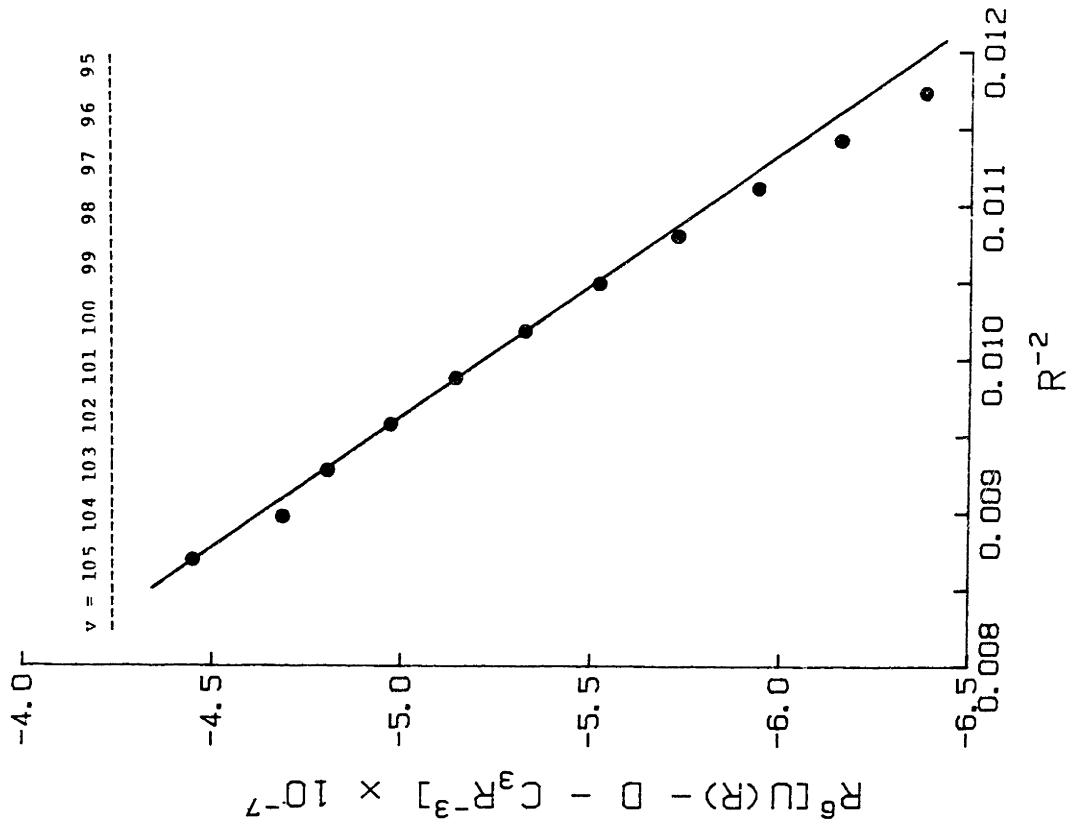
TABLE 5.5   Comparison of theoretically predicted long range and electron-
exchange contributions to the potential energy as a function of
internuclear separation, using D_e = 22990.247 cm^{-1}, C_3 =
-4.0114×10^5 cm^{-1} $Å^3$, C_6 = -1.9969×10^7 cm^{-1} $Å^6$, C_8 = -1.3984×10^9
cm^{-1} $Å^8$, A = -4.389×10^5 cm^{-1}, B=1.092 $Å^{-1}$.

v	R(v)	E(v) - D_e	C_3/R^3	C_6/R^6	C_8/R^8	Aexp(-BR)
95	9.232	-613.221	-509.875	-32.262	-26.510	-18.377
96	9.357	-581.677	-489.658	-29.754	-23.799	-16.026
97	9.487	-551.466	-469.737	-27.383	-21.304	-13.899
98	9.623	-522.559	-450.156	-25.147	-19.017	-11.985
99	9.764	-494.932	-430.929	-23.045	-16.927	-10.275
100	9.911	-468.559	-412.065	-21.072	-15.023	-8.753
101	10.063	-443.413	-393.599	-19.225	-13.294	-7.490
102	10.222	-419.453	-375.573	-17.505	-11.732	-6.232
103	10.386	-396.641	-358.062	-15.910	-10.329	-5.210
104	10.558	-374.940	-340.804	-14.414	-9.054	-4.316
105	10.729	-354.309	-324.824	-13.094	-7.966	-3.583

Figure 5.7 Graphical determination of the C_3 coefficient for the Na$_2$ A$^1\Sigma_u^+$ state.
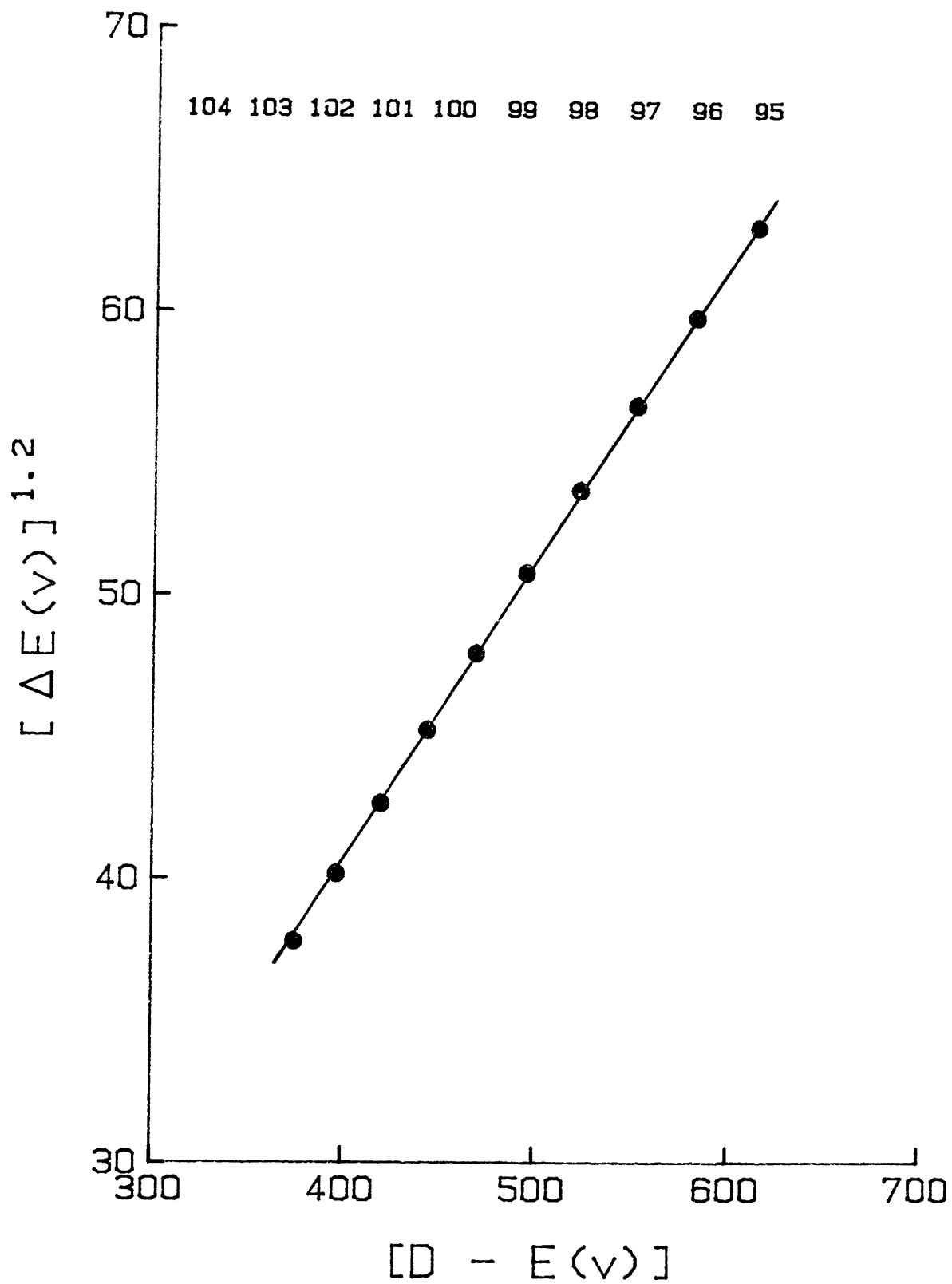
CHAPTER SIX

CONCLUSION

The primary factor which enabled us to study the high lying vibrational levels in the excited electronic states of Na_2, the A $^1\Sigma_u^+$ and B $^1\Pi_u$ states, was the sample-preparation capabilities of the MGS excitation scheme. Using the MGS technique, we have observed the energies of all quasibound levels in the $B^1\Pi_u$ state. Combining these energies with the rotation-dependent tunneling rates observed for the last quasibound level has allowed a determination of the B state potential barrier near its maximum. In the A $^1\Sigma_u^+$ state, many vibrational levels in the range v=43-105 have been observed and have led to a characterization of the A state intramolecular potential up to 96% of its dissociation limit. Thus the initial objective set forth in the introduction of characterizing the A and B state long range potentials has been achieved.

In addition to this primary goal, we had hoped to be able to reduce the A and B state long range potentials into two sets of C_n coefficients (describing the long range behavior for each molecular state) and thereby obtain the long range behavior of all molecular states correlating with the Na(3s) + Na(3p) atomic limit. Such a reduction would also have allowed us to make a reasonable estimate of two fundamental atomic properties: the Na D-lines oscillator strength from the C_3 coefficient and the static dipole polarizabilities of the Na(^{2}P) state from the C_6 coefficients. There already exist high accuracy measurements of these two atomic properties[51,59]; therefore, if the C_n coefficients could be extracted from the long range potentials of Na_2, we would have a check of the resulting atomic properties.

However, the hope of breaking down the A and B molecular potentials into their constituent C_n coefficients was not completely successful.

The compound effect of a) the leading C_3/R^3 term dominating the potential over a broad range of R and b) the large electron-exchange terms, relative to higher order C_n/R^n terms, led to an inadequate determination of the C_n coefficients.

We hope the present results on the A and B state long range potentials are useful to current theories of the photodissociation process[62], $Na_2(X\ ^1\Sigma_g^+) + h\nu \rightarrow Na(^2S_{1/2}) + Na(^2P_{3/2}, ^2P_{1/2})$, which proceeds primarily via the $A\ ^1\Sigma_u^+$ and $B^1\Pi_u$ molecular states. Resonances in the $^2P_{3/2}$ fine structure cross section (due to quasibound levels of the B state) should depend very sensitively on the shape of the barrier; the ratio of photodissociation cross sections for $^2P_{3/2}:^2P_{1/2}$ atoms may reflect the nonadiabatic interactions of the A and B states with other molecular states at large R.

REFERENCES

1. R.J. Le Roy, in Molecular Spectroscopy, vol. 1, R.F. Barrow, D.A. Long and D.J. Miller, eds. (London, 1973) Chapter 3.

2. J.B. Koffend, Thesis, M.I.T., Cambridge (1978).

3. F. Martin, S. Churassy, R. Bacis, R. W. Field, and J. Verges, J. Chem. Phys. 79, 3725 (1983).

4. R.B. Bernstein and J.T. Muckerman, in Intermolecular Forces (Advances in Chemical Physics, vol. 12), J. Hirschfelder, ed. (Interscience, New York, 1967) p. 389.

5. H. Pauly and J.P. Toennies, in Advances in Atomic and Molecular Physics, vol. 1, D.R. Bates and I. Estermann, eds. (Academic Press, New York, 1965).

6. E.L. Lewis, Physics Reports 58, 1 (1980).

7. (a) J. Huennekens and A. Gallagher, in Spectral Line Shapes, vol. 2, K. Burnett, ed. (Walter de Gruyter, Berlin, 1983), p. 665; (b) D. Veza, J. Rukavina, M. Movre, V. Vujnović and G. Pichler, Opt. Comm. 34, 77 (1980).

8. J.O. Hirschfelder, C.F. Curtiss, and R.B. Bird, Molecular Theory of Gases and Liquids (Wiley, New York, 1964).

9. R.R. Freeman, D.E. Pritchard, and D. Kleppner, Phys. Rev. A, 13, 907 (1976).

10. T.Y. Chang, Rev. Mod. Phys. 39, 911 (1967).

11. F.E. Cummings, Thesis, Harvard University, Cambridge (1972).

12. B. Bussery, Thesis, L'universite Claude-Bernard Lyon-1 (1984).

13. (a) W. Demtröder, M. McClintock, and R.N. Zare, J. Chem. Phys. 51, 5495 (1969); (b) W. Demtröder and M. Stock, J. Mol. Spec. 55, 476 (1975).

14. P. Kusch and M.M. Hessel, J. Chem. Phys. 68, 2591 (1978).

15. P. Kusch and M.M. Hessel, J. Chem. Phys. 63, 4087 (1975).

16. M.E. Kaminsky, J. Chem. Phys 66, 4951 (1977); ibid. 73, 3520(E) (1980).

17. G. Gerber and R. Moller, Chem. Phys Letters 113, 546 (1985).

18. C. N. Man-Pichot and A. Brillet, IEEE J. of Quantum Electronics QE16, 1103 (1980).

19. T.W. Hänsch, A.L. Schawlow, P.E. Toschek, IEEE J. Quantum Electronics QE-8, 802 (1972).

20. W. Brunner and H. Paul, Opt. Comm. 12, 252 (1974).

21. A.N. Nesmeyanov, Vapor Pressure of the Elements (Academic Press, New York, 1963).

22. S. Gerstenkorn and P. Luc, Atlas du Spectre d'Absorption de la Molecule d'Iode (CNRS, Paris, 1978).

23. B. Wellegehausen, IEEE J. Quantum Electronics QE-15, 1108 (1979).

24. C. N. Man and A. Brillet, Opt. Comm. 45, 95 (1983).

25. N. Skribanowitz, M. S. Feld, R. E. Francke, M. J. Kelly and A. Javan, App. Phys. Letters 19, 161 (1971).

26. S. Churassy, Thesis, L'universite Claude Bernard Lyon-1 (1979).

27. I.C. Finlay and D.B. Green, J. Phys. E.: Sci. Inst. 9, 1026 (1976).

28. P.D. Dunn and D.A. Reay, Heat Pipes (Pergamon, Oxford, 1978).

29. L.A. Melton, National Bureau of Standards Special Publication 561, Proceedings of the 10th Materials Research Symposium on Characterization of High Temperature Vapors and Gases held at NBS, Gaithersburg, Maryland, September 18-22, 1978. (1979).

30. a) H. Kogelnik and T. Li, Appl. Opt. 5, 1550 (1966); b) H.A. Haus, Waves and Fields in Optoelectronics (Prentice-Hall, New Jersey, 1984); c) J.T. Verdeyen, Laser Electronics (Prentice-Hall, New Jersey, 1981).

31. Coherent Radiation, Inc.; private communication.

32. J.B. Marion, Classical Electromagnetic Radiation (Academic Press, New York 1980).

33. J.D. Jackson, Classical Electrodynamics (Wiley, New York, 1962).

34. G.W. King and J.H. VanVleck, Phys. Rev. 55, 1165 (1939).

35. B. Linder and J. O. Hirschfelder, J. Chem. Phys. 28, 197 (1957).

36. P.R. Fontana, Phys. Rev. 123, 1865 (1961); ibid. 123, 1871 (1961); ibid. 125, 1597 (1962).

37. H. Margenau and N.R. Kestner, Theory of Intermolecular Forces (Pergamon, Oxford, 1969) Chapter 8.

38. F. London, Trans. Faraday Soc. 33, 8 (1937).

39. A. Unsöld, Z. Physik 43, 563 (1927).

40. H. L. Kramer, J. Chem. Phys. 53, 2783 (1970).

41. J.F. Bukta and W. J. Meath, Mol. Phys. 25, 1203 (1973).

42. F. Vigné-Maeder, Chem. Phys. 85, 139 (1984).

43. D. D. Konowalow and M. E. Rosenkrantz, J. Phys. Chem. 86, 1099 (1982).

44. W. C. Stwalley and W. T. Zemke, unpublished results.

45. J. Keller and J. Weiner, Phys. Rev. A 29, 2943 (1984).

46. a) A. Hashemi-Attar, C. B. Beckel, W. N. Keepin, and S. S. Sonnleitner, J. Chem. Phys. 70, 3881 (1979); b) J. W. Tromp and R. J. Le Roy, sub. to J. Mol. Spec. (1984).

47. R. J. Le Roy and Bernstein, J. Chem. Phys. 52, 3869 (1970); R. J. Le Roy and R. B. Bernstein, J. Mol. Spectros. 37, 109 (1971).

48. C. E. Moore, National Standard Reference Data Series (National Bureau of Standards (U.S.), 35/V.I 1971).

49. R. F. Barrow, J. Vergés, C. Effantin, K. Hussein and J. D'Incan, Chem. Phys. Lett. 79, 6060 (1983).

50. (a) R. J. LeRoy and W. K. Liu, J. Chem. Phys. 69, 3622 (1978); (b) D. Rapp, Quantum Mechanics (Holt, Rinehart and Wilson, New York, 1971) Chapter 9.

51. A. Gaupp, P. Kuske and H. J. Andrä, Phys. Rev. A 26, 3351 (1982).

52. R. F. Barrow, J. Vergés, C. Effantin, K. Hussein and J. D'Incan, Chem. Phys. Letts. 104, 179 (1984).

53. (a) R. Rydberg, Z. Physik 73, 376 (1931); 80, 514 (1933); b) O. Klein, Z. Physik 76, 226 (1932); c) A. L. G. Rees, Proc. Phys. Soc. (London) A59, 998 (1947); d) J. T. Vanderslice, E. A. Mason, W. G. Maisch, E. R. Lippincott, J. Mol. Spectros. 3, 17 (1959).

54. M. E. Kaminsky, Thesis, Stanford University (1976).

55. R. J. Le Roy, J. Chem. Phys. 73, 6003 (1980).

56. R. J. Le Roy, unpublished results.

57. T. Namioka, J. Chem. Phys. $\underline{40}$, 3154 (1964); also see W. C. Stwalley, Chem. Phys. Lett. $\underline{6}$, 241 (1970).

58. W. Kolos, Intr. J. Quantum Chem. $\underline{1}$, 169 (1967).

59. H. T. Duong and J.-L. Picqué, J. de Physique $\underline{33}$, 513 (1972).

60. H. Kreck and W. J. Meath, J. Chem. Phys. $\underline{50}$, 2289 (1969).

61. M. Krauss and D. B. Neumann, J. Chem. Phys. 71, 107 (1979).

62. W. S. Struve, S. J. Singer and K. F. Freed, submitted to J. Chem. Phys. (1984).